TAMPEREEN TEKNILLINEN YLIOPISTO
TAMPERE UNIVERSITY OF TECHNOLOGY

Mariusz Zdanowicz

Nonlinear Optical Response of Metal Nanoparticles and Nanocomposites

Julkaisu 1241 • Publication 1241

Tampere 2014

Tampereen teknillinen yliopisto. Julkaisu 1241
Tampere University of Technology. Publication 1241

Mariusz Zdanowicz

Nonlinear Optical Response of Metal Nanoparticles and Nanocomposites

Thesis for the degree of Doctor of Science in Technology to be presented with due permission for public examination and criticism in Sähkötalo Building, Auditorium S1, at Tampere University of Technology, on the 12th of September 2014, at 12 noon.

Tampereen teknillinen yliopisto - Tampere University of Technology
Tampere 2014

ISBN 978-952-15-3351-8 (printed)
ISBN 978-952-15-3358-7 (PDF)
ISSN 1459-2045

Abstract

In this work, we study the second-order nonlinear optical properties of two kinds of nanoplasmonic structures. The first part of the study concerns regular arrays of L-shaped gold nanoparticles. The samples are investigated by linear characterization, i.e., extinction spectroscopy, and by second-harmonic generation. By incorporating the effective medium theory into the earlier developed nonlinear response tensor formalism, we determine the effects connected to higher-multipolar interactions in the second-order nonlinear response of the samples. We verify the effect of the sample quality on the presence of such multipolar contributions, as well as the effect of the local field enhancement, which is driven by the plasmon resonance.

In the second part of the thesis, we investigate bulk-like materials with symmetry breaking along the direction of the normal to the sample surface. These samples are fabricated with aerosol techniques, which are relatively cheap and time efficient. The symmetry breaking is induced by the structure, i.e. by separating consecutive layers of silver-glass nanocomposite with silica glass. It is shown that after optimization such a structure might be interesting as a second-order nonlinear material. We also develop an analytical model that allows us to estimate the surface nonlinear tensor of such structures. Preliminary estimates show that decreasing the effective thickness of such structures could improve their nonlinear properties.

Preface

The research presented in this thesis has been done in the Optics Laboratory of the Department of Physics at Tampere University of Technology. It is a wonderful and friendly working environment, and I will always remember the pleasant atmosphere. In a first place I would like to acknowledge the financial support from Jenny and Antti Wihuri foundation, and also Academy of Finland for funding the projects related to my research.

I would like to express my deepest gratitude for my supervisor, Prof. Goëry Genty for the guidance and the trust he put in me to finish this work. I would also like to thank Prof. Martti Kauranen for the discussions and great help in gaining knowledge and understanding in the field of nanoplasmonics - a novelty for me, at my early years in TUT. I also thank Prof. Marian Marciniak from National Institute of Telecommunications for inspiring me to start my PhD studies.

I would like to express my gratitude for the collaborators in the University of Eastern Finland, for fabricating the L-shaped nanoparticle samples, and my colleagues from TUT: Robert Czaplicki, and Kalle Koskinen for the valuable cooperation in this project. I want to thank the collaborators from Aerosol Physics Department at TUT, especially Juha Harra, for the preparation of the silver nanoparticles, and Prof. Jyrkki Mäkelä, for supervising the fabrication. I also thank Antti Rantamäki from Optoelectronics Research Center in Tampere for the help in fabrication of the silver nanocomposite samples.

In this place I would also like to thank Sami Kujala for the introduction to the multipolar effects, Mikael Siltanen and Francísco Rodríguez Martinez for their great help in organizing life in Tampere. Thank you "Polish Mafia" - Robert and Piortr, for the valuable discussions in my favorite language. Thanks to you I did not forget how to pronounce "Konstantynopolitańczykowianeczka". Dear Juha, I still feel like I owe you an apologies for ruining your glasses, I hope you do understand it happened under the conditions I could not fully control. I remember the weather was rough and the wave was high on a Baltic. Antti, Aku, Johan, Kalle and Mikko N., thank you for sharing the good times, at work and after it, I keep these moments dear. Godofredo, I consider you one of the kindest man I have met in life, and I truly wish you success and happiness in life. Actually I wish that to all the people mentioned here.

The moment comes when you realize it is really hard to mention all the people you would

like to thank. I really appreciate the time spent in Tampere. All the other people I have met an TUT, thank you so much, Abdel, Caroline, Elisa, Jouni, Laura, Léo, Mari, Matti, Mikko H., Miro, Puskal, Roope, Samu, Tapsa, Victor, Wendy, and all the others which names are not mentioned - it was great to work and spend free time with you all. Special thanks go to the staff of our Department: Ari, Hanna, Inkeri and Jaana. Thank you all, my friends from Tampere. For those who actually read that far, if you happen to be around, do not hesitate to contact me, feel invited to my home, wherever it will be at the moment.

The last part of this few words goes to my family, Mother, Father, and my Sister, thank you for your support. You did shape me as I am now, for which I am grateful. To you I am saying simple: Dziękuję. The last but certainly not least. Terribly important in fact. Thank you Weronika for finding me out there, and joining me in this journey, which became more interesting and beautiful since you joined in. Let's go to the end of it together, what do you say?

Tampere, September 2014

Mariusz Zdanowicz

Contents

List of Publications

Publication 1

M. Zdanowicz, S. Kujala, H. Husu, and M. Kauranen, "Effective medium multipolar tensor analysis of second-harmonic generation from metal nanoparticles," New Journal of Physics **13**, 023025 (2011).

Publication 2

R. Czaplicki, M. Zdanowicz, K. Koskinen, J. Laukkanen, M. Kuittinen, and M. Kauranen, "Dipole limit in second-harmonic generation from arrays of gold nanoparticles, Opt. Express **19**, 26866–26871 (2011).

Publication 3

M. Zdanowicz, J. Harra, J. M. Mäkelä, E. Heinonen, T. Ning, M. Kauranen, and G. Genty, "Ordered multilayer silica-metal nanocomposites for second-order nonlinear optics," Applied Physics Letters **103**, 251907 (2013).

Publication 4

M. Zdanowicz, J. Harra, J. M. Mäkelä, E. Heinonen, T. Ning, M. Kauranen, and G. Genty, "Second-harmonic response of multilayer nanocomposites of silver-decorated nanoparticles and silica," Scientific Reports **6**, 5745 (2014).

Author's Contribution

This Thesis consists of a number publications. All the publications deal with recent advances made in the field of the linear and nonlinear properties of different types of metal nanostructures. Short descriptions about the subjects and key results of the publications as well as the contribution of the author to each publication are listed below.

Paper 1

This paper presents detailed multipolar tensor analysis of second-harmonic generation (SHG) from arrays of L-shaped gold nanoparticles. Three effective nonlinear tensors, which include electric dipoles only (A^{eee}) and lowest-order magnetic (and quadrupole) effects at the fundamental (A^{eem}) and SHG (A^{mee}) frequency are defined. The model introduced allows for the determination of the contributions of different multipolar orders to the SHG signal generated by arrays of L-shaped nanoparticles. The author contributed to all parts of the study as first author.

Paper 2

This paper presents a multipolar tensor analysis of second-harmonic generation from arrays of noncentrosymmetric gold nanoparticles. In contrast to earlier results, where higher multipoles and symmetry-forbidden signals arising from sample defects did play a significant role, the results presented in this publication are dominated by symmetry-allowed electric-dipole tensor components. The results determine the role of sample quality to the multipolar nature of the SH signals. The author contributed to the experiments and reporting of the study as second author.

Paper 3

We utilize aerosol synthesis to fabricate ordered metal-silica nanocomposites consisting of alternating layers of pure silica and silica nanoparticles decorated with silver nanodots. These multilayer structures preserve the narrow plasmon resonance of the nanodots even for high optical densities and allow second-harmonic generation due to spontaneous symmetry breaking arising from the interfaces between the silica and nanoparticle layers. The concept presented in the publication opens up new

perspectives for complex structures for advanced optical applications. The author contributed to all parts of the study as a first author.

Paper 4

In this work, we perform a detailed characterisation of the second-order nonlinear response of nanocomposites consisting of alternating layers of silver-decorated silica nanoparticles and pure silica. The samples were fabricated using methods described in publication 3. The second-order nonlinear response increases with the number of layers. Using a combination of polarization and Maker-fringe measurements, we determine the effective susceptibility tensor components of a single active layer of silver-decorated silica nanoparticles and pure silica. The author contributed to all parts of the study as a first author.

The results obtained and reported in the publications have contributions from a group of people. The contribution from the Author of this Thesis is estimated in the table below. The table is divided into four parts. Preparation includes designing the samples and all required work before that. Experiments include deciding the type of the experiment used for characterization, building the setup and actual measurements. Calculations include developing the theoretical model and numerical calculations. Reporting includes analysis of the measured data and reporting obtained results in a publications.

Table 1.

	Preparation	**Experiments**	**Calculations**	**Reporting**
Paper 1	50 %	90 %	90 %	90 %
Paper 2	50 %	80 %	90 %	50 %
Paper 3	80 %	100 %	90 %	90 %
Paper 4	80 %	100 %	90 %	90 %

List of Figures

List of Tables

List of Abbreviations and Symbols

EBL	Electron-beam lithography
EM	Electromagnetic
HWP	Half-wave plate
LSP	Localized surface plasmon
NL	Nonlinear
NRT	Nonlinear response tensor
QWP	Quarter-wave plate
SERS	Surface-enhanced Raman scattering
SH	Second-harmonic
SHG	Second-harmonic generation
TE	Transverse electric
THG	Third-harmonic generation
TM	Transverse magnetic
ϵ	Relative permittivity, dielectric function
ϵ_0	Free space permittivity
$\mathbf{M}$	Magnetization
$\mathbf{P}$	Electric polarization
$\mathbf{Q}$	Quadrupolarization
$\mathbf{B}$	Magnetic flux density

$\mathbf{D}$	Electric displacement field
$\mathbf{E}$	Electric field
$\mathbf{H}$	Magnetic field
$\mathbf{J}$	Free current density
μ	Relative permeability
μ_0	Free space permeability
ρ	Free charge density
$\widetilde{}$	Quantity that varies rapidly in time, e.g. $\widetilde{\mathbf{E}}$

Chapter 1

Introduction

The demonstration of second-harmonic generation (SHG) in crystalline quartz using a ruby laser[5], only three years after the development of the first laser[6], marks the beginning of the field of nonlinear optics. Subsequent progress in the development of laser systems and measurement techniques led to experiments revealing new mechanisms of nonlinear processes as well as new nonlinear materials. A particularly interesting class of materials in optics nowadays are so called metamaterials. Meatamaterials are artificial materials that do not appear in nature and whose optical characteristics can be engineered to guide light in unconventional fashions. Their remarkable linear and nonlinear characteristics are the result of the utilization of metals in nanoscale.

1.1 Metals in Optics

Recent advances in the fabrication of nanoscale structures allows for better understanding and control of the characteristics of metamaterials. Metal particles with sizes of the order of a few to a few hundred nanometers interact strongly with the electromagnetic field at optical frequencies. The resulting collective oscillations of the free electrons inside the particles induce a range of interesting effects like plasmon resonances or the lightning rod effect. The first theoretical models describing the optical characteristics of metallic nanoparticles were formulated by Maxwell Garnett in 1904[7], and Gustav Mie in 1908[8]. Because of their

unique properties, metals can change the optical characteristics of dielectric materials in remarkable ways. In fact, the characteristics of the metal-dielectric composite material can be significantly different from those of its constituent components[9]. Nowadays, research on optical properties of metal nanoparticles and nanostructures is very popular. It is a major part of the expanding field of nanoplasmonics, which studies the interactions of such structures with the electromagnetic field. The main cause of such interest in the field of nanoplasmonics is its extremely broad spectrum of applications, starting from biosensors and photovoltaics, to spectroscopy, microscopy and ultrafast dynamics.

The optical responses of metal nanoparticles arise from the plasmonic oscillations of their conduction electrons. The resulting localized surface plasmon (LSP) resonances give rise to strong electromagnetic fields near the metal-dielectric interface. The theoretical models used to calculate the responses of metal nanostructures are well suited for spheroids and ellipsoids[10]. However, analytic theories generally fail to fully explain the responses of samples with more complex geometries. Intense experimental studies to determine responses of different geometries of nanoparticles have been conducted for over 20 years now. These studies cover various geometries of metal particles, from the simplest spheres, ellipsoids and nanorods[10,11], to more advanced shapes, including nanorings[12], nanoshells[13,14], and split-ring resonators[15,16]. These experimental studies bring rise to understanding of the phenomena, and help to form new empiric models which consecutively can be used for further optimization of plasmonic structures. It is possible thanks to the fact that plasmonic resonances depend sensitively on the particle size[17,18] and shape[19–22] as well as their dielectric environment. The possibilities of modifying these resonances are indeed extremely broad, and they allow for tailoring the plasmon resonance to fit specific applications. Determining the correlation between the plasmon resonance and aforementioned structure parameters now bring benefit to the fields of biosensing[23,24], imaging[25,26], and solar cells[27,28].

The local-field enhancement is particularly important for nonlinear optical effects, which scale with a high power of the electromagnetic field. The effective medium theories have been successful in describing the enhancement of third-order effects in bulk-type metal-dielectric nanocomposites[9,29], with no particular constraints on symmetry. However, due to the symmetry properties of the electric susceptibility tensor, second-order effects, such as second harmonic generation (SHG), require non-centrosymmetric samples and their observation has so far been limited to surface geometries. Enhancement of SHG by rough metal surfaces was demonstrated early on[30]. More recently, lithographic arrays of non-

centrosymmetric particles have been introduced as second-order metamaterials[2,31–33] but such samples are difficult to fabricate. The nonlinear responses (both second- and third-order) of a macroscopic sample can be enhanced by tuning the incident laser close to the plasmon resonance of the particles[34,35] or by increasing their density. Unfortunately, the latter approach generally degrades the quality (shape and linewidth) of the resonances either due to clustering of particles causing inhomogeneous broadening[36,37], or because of the near-field interactions between individual elements[38].

In the Optics Laboratory of Tampere University of Technology, the research in the field of metal nanostructures began already in 2001. Our laboratory was one of the first to address systematically the nonlinear optical properties of such structures. The performed studies helped us to understand the underlying physical phenomena in the nonlinear processes of metal nanostructures. The structures investigated in our lab were non-centrosymmetric; thus, the best tool for determining their properties was second-harmonic generation. Previously, the linear properties, like plasmon resonance central wavelength dependence on particle size were investigated[39]. However, the most interest of our research goes to the nonlinear properties of metal nanostructures. The effects like chiral symmetry breaking reflect defects of the nanostructures, which can be explained by higher-multipolar interactions in the nonlinear processes[32,40,41].

1.2 This Work

The main objective of the research was to create a valuable input in the field of nonlinear nanoplasmonics. To gain the understanding in the fundamental processes governing the interaction of light with various types of metal nanostructures. Even though we barely scratch a surface of extremely broad field of nanoplasmonics, we were able to achieve very interesting results, which are compiled in this thesis. In this work, we develop further the concept of the Nonlinear Response Tensor already used in the analysis of nonlinear effects in metal nanostructures[42], to account for the higher multipolar effects at the second-harmonic and fundamental frequencies. The nonlinear experiments performed in the framework of this thesis reveal novel interesting aspects about the metal nanostructures, and give the answer to the hypothesis formed in previous works that relates the quality of the sample with the multipolar contributions to the total second-harmonic signal. We first investigate the presence of the higher multipolar effects in second-harmonic signals generated by an

array of L-shaped nanoparticles, with particular interest in magnetic-dipole and electric-quadrupole contributions. We determine the conditions for the optimization of the array of metal particles for the suppression of these effects. In the second part of the thesis, we develop a new concept for the fabrication of nanocomposite structures, based on aerosol techniques. The main advantages of this new method are relatively low fabrication costs and relatively high speed of the fabrication process. For both kinds of samples we determine the linear and nonlinear properties arising from the presence of metals in the nanoscale. We show that the optical properties of the structures are determined by their smallest details, and by controlling those, we are able to fabricate structures with better and better properties.

1.3 Structure of the Thesis

This thesis summarizes the research results contained in four original publications. Chapter 2 contains the theoretical background of the field of nonlinear optics. Starting from Maxwell's equations, we derive the wave equation that accounts for the higher-order effects (e.g., magnetic dipole, electric quadrupole) that act as sources for the second-harmonic field. We also present the symmetry rules governing the second-order nonlinear phenomena, and introduce the concept of the nonlinear response tensor, which is later used for the analysis of the measurements made in the thesis.

Chapter 3 introduces the electromagnetic properties of metals. We briefly explain the phenomenon of plasmon resonance, and present the theory of the effective medium, which accounts for the effective parameters of the compound material containing a mixture of metal nanoparticles and glass.

Chapter 4 covers the techniques used to fabricate the different samples as well as the experimental setups used for their characterization. Chapter 4 also describes the theoretical models used for the data analysis. The main experimental results and findings are discussed in Chapter 5.

The thesis is concluded with Chapter 6, where the main results are summarized and perspectives for future research are opened.

Chapter 2

Nonlinear Optics

A complete description of interaction between light and matter is provided by quantum electrodynamics[43]. Although it produces excellent agreement between special relativity and quantum mechanics, allowing for accurate predictions of certain quantities (e.g., anomalous magnetic moment of the electron), it is rather tedious to apply for the description of nonlinear phenomena. Nonlinear light-matter interactions may be described more simply within the framework of classical electrodynamics. In this chapter, starting from the Maxwell's equations of classical electrodynamics, we derive the wave equation that governs the light propagation in a medium, including effects arising from the nonlinear interaction between light and the medium. The presented approach also accounts for higher-order effects (magnetic dipole and electric quadrupole sources), and it explains the role of symmetry in second-order nonlinear effects.

2.1 Maxwell's Equations and Wave Equation

The interaction of electromagnetic (EM) waves and matter is well described by Maxwell's equations[44]. Maxwell's equations connect together the magnetic and electric field and are the foundation of classical electrodynamics. In the SI system of units the set of four

equations is written in differential form as[45]:

$$\begin{aligned} \nabla \times \widetilde{\mathbf{E}} &= -\tfrac{\partial \widetilde{\mathbf{B}}}{\partial t}, & \nabla \cdot \widetilde{\mathbf{D}} &= \rho, \\ \nabla \times \widetilde{\mathbf{H}} &= \widetilde{\mathbf{J}} + \tfrac{\partial \widetilde{\mathbf{D}}}{\partial t}, \text{and} & \nabla \cdot \widetilde{\mathbf{B}} &= 0, \end{aligned} \tag{2.1}$$

where $\widetilde{\mathbf{E}}$ is the electric field, $\widetilde{\mathbf{D}}$ is the electric displacement field, $\widetilde{\mathbf{H}}$ is the magnetic field, and $\widetilde{\mathbf{B}}$ is the magnetic flux density. The last two quantities, the free current density $\widetilde{\mathbf{J}}$, and free charge density ρ, describe the interaction of the EM field with free electric charges within the medium. The complete description of light-matter interaction is given by the above expressions together with the constitutive relations, which describe the medium:

$$\widetilde{\mathbf{D}} = \epsilon_0 \widetilde{\mathbf{E}} + \widetilde{\mathbf{P}}, \tag{2.2a}$$

$$\widetilde{\mathbf{H}} = \frac{1}{\mu_0} \widetilde{\mathbf{B}} - \widetilde{\mathbf{M}}. \tag{2.2b}$$

In the above expressions $\widetilde{\mathbf{P}}$ and $\widetilde{\mathbf{M}}$ are the electric polarization and magnetization, respectively; ϵ_0 and μ_0 represent the electric permittivity and magnetic permeability of the free space, respectively. Equations 2.2 describe the material response to the external EM field.

For a dielectric, non-magnetic material, the free charge density ρ, free current density $\widetilde{\mathbf{J}}$, and magnetization $\widetilde{\mathbf{M}}$ can be neglected. The work we present in this thesis describes the interaction between the EM field and materials consisting of metal nanoparticles, which are both conductive and magnetic, and thus these quantities cannot be neglected. Combining Eqs. (2.1), and (2.2), we obtain[46]:

$$\nabla \times \left(\nabla \times \widetilde{\mathbf{E}} \right) = -\nabla \times \frac{\partial \widetilde{\mathbf{B}}}{\partial t}. \tag{2.3}$$

Using the relation $\nabla \times \left(\nabla \times \widetilde{\mathbf{E}} \right) = \nabla \left(\nabla \cdot \widetilde{\mathbf{E}} \right) - \nabla^2 \widetilde{\mathbf{E}}$, and making use of the plane wave approximation where $\nabla \cdot \widetilde{\mathbf{E}} \equiv 0$, we get the final form of the wave equation:

$$\nabla^2 \widetilde{\mathbf{E}} - \frac{1}{c^2} \frac{\partial^2 \widetilde{\mathbf{E}}}{\partial t^2} = \mu_0 \frac{\partial}{\partial t} \left(\widetilde{\mathbf{J}} + \nabla \times \widetilde{\mathbf{M}} \right) + \mu_0 \frac{\partial^2 \widetilde{\mathbf{P}}}{\partial t^2}. \tag{2.4}$$

The above expression is an inhomogeneous wave equation, where the polarization $\widetilde{\mathbf{P}}$, magnetization $\widetilde{\mathbf{M}}$, and the current density $\widetilde{\mathbf{J}}$ are the source terms for the radiation of EM field.

Provided all the sources are accounted for, Eqs. (2.2), and (2.4) fully describe the interaction of a plane EM wave with the medium. In the general macroscopic case, the problem is extremely difficult to solve. Nevertheless, it can be shown, that averaged macroscopic contributions from collective material sources can be expressed with[47]:

$$\widetilde{\mathbf{D}} = \epsilon_0 \widetilde{\mathbf{E}} + \left(\widetilde{\mathbf{P}} - \nabla \cdot \widetilde{\mathbf{Q}} + \dots \right), \tag{2.5a}$$

$$\widetilde{\mathbf{H}} = \frac{1}{\mu_0} \widetilde{\mathbf{B}} - \left(\widetilde{\mathbf{M}} + \dots \right), \tag{2.5b}$$

where the quantities $\widetilde{\mathbf{P}}$, $\widetilde{\mathbf{Q}}$, and $\widetilde{\mathbf{M}}$ now stand for the macroscopically averaged electric dipole density, electric quadrupole density (quadrupolarization), and magnetic dipole density (magnetization) of the considered medium in the presence of the applied field. Neglecting the higher-order elements of the sums in Eq. (2.5), we can now rewrite Eq. (2.4) as:

$$\nabla^2 \widetilde{\mathbf{E}} - \frac{1}{c^2} \frac{\partial^2 \widetilde{\mathbf{E}}}{\partial t^2} = \mu_0 \frac{\partial}{\partial t} \left(\nabla \times \widetilde{\mathbf{M}} \right) + \mu_0 \frac{\partial^2}{\partial t^2} \left(\widetilde{\mathbf{P}} - \nabla \cdot \widetilde{\mathbf{Q}} \right). \tag{2.6}$$

Assuming a monochromatic field oscillating at frequency ω, and separating the temporal and spatial parts by introducing the form:

$$\widetilde{\mathbf{E}}(\mathbf{r}, t) = \mathbf{E}(\mathbf{r}) e^{-i\omega t} + \mathbf{E}^*(\mathbf{r}) e^{i\omega t}, \tag{2.7}$$

we rewrite Eq. (2.6) as:

$$\nabla^2 \mathbf{E} + \frac{\omega^2}{c^2} \mathbf{E} = -\mu_0 \omega^2 \left[\frac{i}{\omega} \left(\nabla \times \mathbf{M} \right) + \mathbf{P} - \nabla \cdot \mathbf{Q} \right]. \tag{2.8}$$

It is convenient to separate the total contributions of the source terms into linear and nonlinear parts. In order to do that, the polarization $\mathbf{P}$, quadrupolarization $\mathbf{Q}$, and magnetization $\mathbf{M}$ are expanded into power series in terms of the applied field, where the higher-order components of the series account for the nonlinear effects. With this expansion, the source terms are given by: $\mathbf{P} = \mathbf{P}^{(1)} + \mathbf{P}^{NL}$, $\mathbf{Q} = \mathbf{Q}^{(1)} + \mathbf{Q}^{NL}$, and $\mathbf{M} = \mathbf{M}^{(1)} + \mathbf{M}^{NL}$. The electric displacement field, and magnetic field then take the form:

$$\mathbf{D} = \mathbf{D}^{(1)} + \left(\mathbf{P}^{NL} - \nabla \cdot \mathbf{Q}^{NL} \right), \tag{2.9a}$$

$$\mathbf{H} = \mathbf{H}^{(1)} - \mathbf{M}^{NL}. \tag{2.9b}$$

We assume that the linear response is nearly isotropic, and in case of an isotropic materials, the linear part of the quadrupolarization $\mathbf{Q}^{(1)}$ vanishes due to symmetry properties[47]. The

linear parts of $\mathbf{D}^{(1)}$, and $\mathbf{H}^{(1)}$ are expressed with:

$$\mathbf{D}^{(1)} = \epsilon_0 \mathbf{E} + \mathbf{P}^{(1)} \equiv \epsilon_0 \epsilon(\omega) \mathbf{E}, \tag{2.10a}$$

$$\mathbf{H}^{(1)} = \frac{1}{\mu_0} \mathbf{B} - \mathbf{M}^{(1)} \equiv \frac{1}{\mu_0 \mu(\omega)} \mathbf{B}, \tag{2.10b}$$

where $\epsilon(\omega)$, and $\mu(\omega)$ are complex and frequency-dependent dielectric constant and magnetic permeability. The above definitions yield the final form of the wave equation:

$$\nabla^2 \mathbf{E} + \epsilon(\omega)\mu(\omega)\frac{\omega^2}{c^2}\mathbf{E} = -\frac{\omega^2}{c^2}\left[\frac{i}{\omega\epsilon_0}\left(\nabla \times \mathbf{M}^{NL}\right) + \mathbf{P}^{NL} - \nabla \cdot \mathbf{Q}^{NL}\right]. \tag{2.11}$$

We can now define the effective nonlinear polarization of the material, which takes into account the nonlinear part of both the magnetization and quadrupolarization:

$$\mathbf{P}^{NL}_{eff} = \frac{i}{\omega\epsilon_0}\nabla \times \mathbf{M}^{NL} + \mathbf{P}^{NL} - \nabla \cdot \mathbf{Q}^{NL}. \tag{2.12}$$

The above expression is the conventional multipolar expansion used in nonlinear optics[47–49].

In this work we consider second-order nonlinear interactions between the applied EM field and a given material. More specifically, we only consider second-harmonic generation (SHG). In this case, the applied EM field $\mathbf{E}(\omega)$ interacts with itself inside the nonlinear medium, producing a nonlinear (NL) polarization which oscillates at the doubled frequency 2ω. The polarization to first order in the magnetic-dipole and electric-quadrupole interactions is expressed with[48–50]:

$$\begin{aligned}\mathbf{P}(2\omega) = &\chi^{eee}(2\omega;\omega,\omega) : \mathbf{E}(\omega)\mathbf{E}(\omega) \\ &+ \chi^{eem}(2\omega;\omega,\omega) : \mathbf{E}(\omega)\mathbf{B}(\omega) \\ &+ \chi^{eeQ}(2\omega;\omega,\omega) : \mathbf{E}(\omega)\nabla\mathbf{E}(\omega),\end{aligned} \tag{2.13}$$

where the superscripts e, m, and Q denotes whether the nature of the interaction is electric dipolar, magnetic dipolar, or electric quadrupolar, respectively. $\mathbf{E}(\omega)$ and $\mathbf{B}(\omega)$ represent the electric and magnetic fields at the fundamental frequency. The NL polarization acts as a source term for the SHG field according to Eq. (2.11). The inddividual vectorial

components of the nonlinear polarization given by Eq. (2.13) can be written as:

$$\begin{aligned} P_i(2\omega) = &\chi_{ijk}^{eee}(2\omega;\omega,\omega)E_j(\omega)E_k(\omega) \\ &+ \chi_{ijk}^{eem}(2\omega;\omega,\omega)E_j(\omega)B_k(\omega) \\ &+ \chi_{ijkl}^{eeQ}(2\omega;\omega,\omega)E_j(\omega)\nabla_k E_l(\omega). \end{aligned} \tag{2.14}$$

Similarly, the contributions from the nonlinear magnetization and nonlinear quadrupolarization can be included as:

$$\mathbf{M}(2\omega;\omega,\omega) = \chi^{mee} : \mathbf{E}(\omega)\mathbf{E}(\omega), \tag{2.15a}$$

$$\mathbf{Q}(2\omega;\omega,\omega) = \chi^{Qee} : \mathbf{E}(\omega)\mathbf{E}(\omega). \tag{2.15b}$$

With the definitions introduced in this chapter, we next consider the symmetry rules governing SHG generation in nonlinear media.

2.2 Role of Symmetry in Second-Order Nonlinear Phenomena

Symmetry plays a major role in second-order nonlinear processes[45,47]. We first consider the electric dipole contribution to SHG radiation. In general, the nonlinear tensor describing the second order interactions between the vector field and matter is a third rank tensor with $(3 \times 3 \times 3 = 27)$ elements. However, due to symmetry properties, the number of non-vanishing, independent elements of the tensor can be significantly reduced.

Permutation Symmetry

Let us first consider the electric dipole tensor in the case of sum frequency generation, where two photons with the frequencies ω_n and ω_m are annihilated and one photon with sum frequency $\omega_n+\omega_m$ is created. We can write the following sum describing the nonlinear electric dipole polarization for each vectorial component:

$$P_i^{(2)}(\omega_m + \omega_n) = \epsilon_0 \sum_{j,k} \sum_{m,n} \chi_{ijk}^{eee}(\omega_m + \omega_n;\omega_m,\omega_n)E_j(\omega_m)E_k(\omega_n), \tag{2.16}$$

where i, j, and k correspond to the Cartesian coordinates x, y, and z, respectively. We notice that the order of the fields in Eq. 2.16 is arbitrary, and as long as the Cartesian and frequency components are permuted simultaneously, we can reduce the number of the independent components by the relation:

$$\chi_{ijk}^{eee}(\omega_m + \omega_n; \omega_m, \omega_n) = \chi_{ikj}^{eee}(\omega_n + \omega_m; \omega_n, \omega_m). \tag{2.17}$$

This symmetry is known as *intrinsic permutation symmetry*. Moreover, for the case of lossless material we can apply more symmetry rules. The absence of losses implies real components for the nonlinear tensor, which is expressed by:

$$\chi_{ijk}^{eee}(\omega_m + \omega_n; \omega_m, \omega_n) = \chi_{ijk}^{eee*}(\omega_m + \omega_n; \omega_m, \omega_n). \tag{2.18}$$

In such case, *full permutation symmetry* applies to the material, which means that all the frequency components in $\chi_{ijk}^{eee}(\omega_m + \omega_n; \omega_m, \omega_n)$ may be permuted freely, provided that the Cartesian coordinates are permuted simultaneously:

$$\chi_{ijk}^{eee}(\omega_m + \omega_n; \omega_m, \omega_n) = \chi_{kij}^{eee}(\omega_m; \omega_m + \omega_n, -\omega_n). \tag{2.19}$$

Finally, assuming that the dispersion of the tensor χ^{eee} is negligible in the material, we get the *Kleinman symmetry*, which allows us to permute the Cartesian coordinates without permuting the frequency components. In such a case, we get the result:

$$\chi_{ijk}^{eee} = \chi_{kij}^{eee} = \chi_{jki}^{eee} = \chi_{jik}^{eee} = \chi_{kji}^{eee} = \chi_{ikj}^{eee}. \tag{2.20}$$

However, the Kleinman symmetry has very limited validity in practical nonlinear optical materials[51].

Centrosymmetric Medium

We next consider a centrosymmetric medium and its second order response. Owing to the center of symmetry, such a medium is invariant under inversion with respect to a geometrical point. More specifically, for every point $(\mathbf{r})$ we find an indistinguishable point $(-\mathbf{r})$, where $\mathbf{r}$ is a vector originating from the point of symmetry. Let us take into consideration the second-order electric-dipole susceptibility tensor $\chi^{eee}(2\omega, \omega, \omega)$ for SHG.

The nonlinear electric-dipole polarization is then:

$$\mathbf{P}^{(2)}(2\omega) = \epsilon_0 \chi^{eee} \mathbf{E}^2(\omega) \tag{2.21}$$

For the case of an excitation field with opposite sign $-\mathbf{E}(\omega)$, we have:

$$-\mathbf{P}^{(2)}(2\omega) = \epsilon_0 \chi^{eee} \left(-\mathbf{E}(\omega)\right)^2 = \epsilon_0 \chi^{eee} \mathbf{E}^2(\omega) \tag{2.22}$$

where the sign of the electric dipole polarization also changes due to inversion of the field. The right sides of Eqs. 2.21 and 2.22 are equal, which can only hold if all the elements of the electric dipole susceptibility tensor χ^{eee} vanish, implying that electric-dipole SHG in centrosymmetric media is forbidden.

Transformation Properties of Multipoles

The multipolar contributions expressed by Eqs. (2.12-2.15b) are represented by different types of tensors, that can allow for the generation of SH radiation, even inside centrosymmetric media, where the NL electric-dipole tensor χ^{eee} vanishes. The reason of such behavior is that e.g. χ^{mee} and χ^{eem} are associated with two polar vectors (electric quantities) and an axial vector (magnetic quantity), whereas the electric dipole tensor χ^{eee} connects three polar vectors. These tensors transform differently under improper rotation operations (the combination of a rotation about an axis and a reflection in a plane)[52].

In principle, the multipolar orders in SH radiation can be accounted for by their distinctive radiation patterns in three-dimensional space. However, since we are describing SHG radiation, which is a coherent process and produces strongly directional, laser-like emission, we can distinguish only some of these differences in the radiation obtained in transmitted and reflected directions.

Let us now consider two geometries of the generated SHG signals. We can define the vector of EM field $\mathbf{E}$ observed in transmitted direction at a certain point $\mathbf{r}_t$ in a given instant of time. The SHG field generated in the reflected direction $\mathbf{r}_r = -\mathbf{r}_t$ from the sample, will possess different signs related to the nature of the source. For the electric field produced by electric- $\mathbf{E}_p$, magnetic-dipole $\mathbf{E}_m$, and electric quadrupole $\mathbf{E}_Q$ sources

detected at the same instant of time, we get the relations:

$$\mathbf{E}_p(\mathbf{r}_r) = \mathbf{E}_p(\mathbf{r}_t), \tag{2.23a}$$

$$\mathbf{E}_m(\mathbf{r}_r) = -\mathbf{E}_m(\mathbf{r}_t), \tag{2.23b}$$

$$\mathbf{E}_Q(\mathbf{r}_r) = -\mathbf{E}_Q(\mathbf{r}_t). \tag{2.23c}$$

In other words, the subtle changes in the radiation of the SHG source in the transmitted and reflected directions allows us to separate the contributions to the total SHG signal from the electric dipolar and higher multipolar nonlinear tensors[32]. However, magnetic dipoles and electric quadrupoles cannot be distinguished from each other this way.

2.3 Surface Second Harmonic Generation

In the previous section, we showed that SHG is prohibited in centrosymmetric media. However, inversion symmetry is inherently broken at surfaces, which gives rise to an electric dipole allowed second-order response. In that sense, SHG is sensitive probe for the properties and structure of surfaces and thin molecular films[53,53–56]. The nonlinear electric-dipole polarization of a surface can be expressed by the effective surface polarization, similar to Eq. (2.12) with no higher order effects included:

$$\mathbf{P}^{sf}(2\omega) = \chi^{sf} : \mathbf{e}(\omega)\mathbf{e}(\omega), \tag{2.24}$$

where χ^{sf} is the electric dipole-allowed surface nonlinear susceptibility tensor, and $\mathbf{e}(\omega)$ is the electric field at the fundamental frequency ω. The schematic representation of the surface SHG is presented in Fig. 2.1. The fundamental beam is propagating at angle θ with respect to the film normal. The refractive indices at the fundamental and second-harmonic wavelength are n_i and N_i, respectively, where i represents the number of the region (1, 2, or 3). The SHG field propagates at angle Θ and D is the thickness of the thin film. The theory of surface SHG from thin films is, in general, a complex problem, considering effects arising from chirality of the surface, and higher-order nonlinear effects such as nonlinear magnetization[56]. For simplicity, we only consider the special case of an isotropic, achiral surface. Such a surface is uniform in all directions along the surface, so that all the rotations with respect to the surface normal and all mirror operations in planes including the surface normal are symmetry operations. These kind of surfaces belong

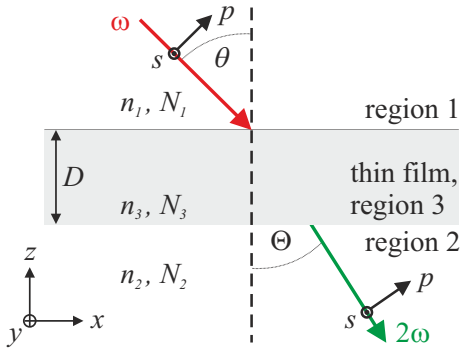

Figure 2.1 Surface second-harmonic generation. Region 3 is the thin film of material with the thickness D, placed between two different materials, marked as region 1 and region 3.

to the symmetry group $C_{\infty\nu}$. Within this symmetry group, and for the case of SHG, the electric-dipole surface tensor has only three non-vanishing, independent components, which are:

$$\begin{aligned} &\chi^{sf}_{zzz}, \\ &\chi^{sf}_{zxx} = \chi^{sf}_{zyy}, \\ \text{and } &\chi^{sf}_{xxz} = \chi^{sf}_{xzx} = \chi^{sf}_{yyz} = \chi^{sf}_{yzy}, \end{aligned} \tag{2.25}$$

where x, and y are the orthogonal in-plane vectors and z is the normal to the surface. Let us now consider SHG from a thin film between two materials(see Fig. 2.1 for illustration). The incoming field is a polarized laser beam at angle of incidence θ with respect to the surface normal. The p-polarized and s-polarized components of the generated SHG field can be expressed by[57]:

$$\begin{aligned} E_p &= \frac{i4\pi\tilde{\omega}}{N_3 \cos\Theta_3}(fe_p^2 + ge_s^2), \\ E_s &= \frac{i4\pi\tilde{\omega}}{N_3 \cos\Theta_3} he_p e_s, \end{aligned} \tag{2.26}$$

where e_p, and e_s refer to the p-, and s-polarized components of the fundamental beam, $\tilde{\omega} = \omega/c$ is the normalized angular frequency, and c is the speed of light in vacuum. In general, the expansion coefficients f, g, and h are complex quantities that depend linearly on the components of the surface susceptibility tensor χ^{sf}. Utilizing the simplified version of Green's function formalism[54,56] we can write the above expansion coefficients in terms of the three independent surface susceptibility components (Eq. 2.25). Neglecting the

absorption and multiple reflections between consecutive layers we have:

$$f = t_{p13}^2 T_{p32} T_{p21} [\chi_{xxz}^{sf} \cos\Theta_3 \sin 2\theta_3 + \chi_{zxx}^{sf} \cos^2\theta_3 \sin\Theta_3 + \chi_{zzz}^{sf} \sin^2\theta_3 \sin\Theta_3], \quad (2.27)$$

$$g = t_{s13}^2 T_{p32} T_{p21} \chi_{zxx}^{sf} \sin\Theta_3, \quad (2.28)$$

$$h = 2 t_{s13} t_{p13} T_{s32} T_{s21} \chi_{zxx}^{sf} \sin\theta_3, \quad (2.29)$$

where the subscripts 1, 2, and 3 refer to the regions as indicated in Fig. 2.1. For convenience, the quantities at the fundamental frequency are denoted by lower-case letters and the quantities at the SH frequency (2ω) are denoted with upper-case letters. With this notation, $n_i(N_i)$ is the refractive index of the i^{th} region and $\theta_i(\Theta_i)$ is the angle of the propagation in the i^{th} region at the fundamental (SHG) frequency. The Fresnel transmission coefficients $t_{sij}(T_{sij})$ and $t_{pij}(T_{pij})$ at the ij interfaces are given by:

$$t_{sij} = \frac{2 n_i \cos\theta_i}{n_i \cos\theta_i + n_j \cos\theta_j}, \quad (2.30a)$$

$$t_{pij} = \frac{2 n_i \cos\theta_i}{n_i \cos\theta_j + n_j \cos\theta_i}. \quad (2.30b)$$

The above formulas describe the Fresnel transmission coefficients between region i and region j and apply both for the case of the fundamental and SHG fields, simply replacing lower-case by upper-case letters.

We now consider the p-polarized SHG field E_p, generated by the p-polarized component of the fundamental beam e_p. Taking into account the propagation effects in the region 3 and transmissions between the regions 1, 2 and 3, omitting absorption and multiple reflections between interfaces, we can derive an expression for the amplitude of the SHG field generated in the thin layer[56], marked as region 3 in Fig. 2.1:

$$E_p(2\omega) = \frac{i 4\pi\tilde{\omega}}{2 N_3 \cos\Theta_3} e_p(\omega) e_p(\omega) t_{p12}^2 T_{p32} \exp\left[i(2\tilde{\omega} N_3 \cos\Theta_3 D)\right] \times \left\{\chi_{xxz}^{sf} \sin 2\theta_3 \cos\Theta_3 + \sin\Theta_3 [\chi_{zxx}^{sf} (\cos\theta_3)^2 + \chi_{zzz}^{sf} (\sin\theta_3)^2]\right\}. \quad (2.31)$$

2.4 Nonlinear Response Tensor

The theory presented above allows to fully describe the interaction of the nonlinear medium with an EM field. We need to remember, however, that the susceptibility formalism presented here assumes that the nonlinear medium is homogeneous on a scale smaller than wavelength, i.e. the variations in the material properties as well as in the local EM field at the fundamental frequency, occur on scales much smaller than the wavelength of the incident light. In the case of metal nanostructures, this is not always true, as the particle sizes, electromagnetic field, and nonlinear sources can vary significantly over the scale of a wavelength[58,59]. Thus, the full description of the nonlinear polarization in metal nanostructures would require accounting for the variations in local fields, generated nonlinear sources, including higher multipoles, coupling of the incoming and outgoing fields to the local fields, etc. Direct integration of all these quantities to predict the nonlinear responses is computationally challenging even for structures with a high degree of symmetry, and nearly impossible for structures with more realistic features.

A scattering matrix-like formalism for the description of the second-order nonlinear responses was developed to perform analysis of the SHG measurements on a samples with complex geometries. The nonlinear response tensor (NRT) formalism operates on the level of input and output fields, treating the sample itself as a "black box"[60]. It allows to link a specific polarization component of the SH field polarization with components of the fundamental field by a simple algebraic relation:

$$E_i(2\omega) = \sum_{jk} A_{ijk} E_j(\omega) E_k(\omega), \tag{2.32}$$

where A_{ijk} is the ijk NRT component, $E_i(2\omega)$ is the i^{th} component of the outgoing SH field, and the j^{th} and k^{th} components of the incoming fundamental field are $E_j(\omega)$ and $E_k(\omega)$, respectively. Unlike in the susceptibility formalism, a measurable SH field appears instead of the nonlinear source on the left side of Eq. (2.32). Therefore, the NRT appeares as a macroscopic parameter that implicitly includes the contributions of all nonlinear sources. The main advantage of such formalism is its simplicity. However, the values of the NRT tensor elements are related more to experimental geometry than to the actual sample. Nevertheless it provides useful information about the macroscopic response of the sample, and by comparing the determined values of the NTR under different experimental conditions we can obtain more detailed information about the underlying

physical processes[32].

Chapter 3

Metal Nanostructures

In this chapter, we provide a theoretical description of the optical properties of metals. Introducing the Drude model of the relative permittivity of metals allows explaining the mechanism of plasmon resonances. The theory of the effective medium helps to derive the properties of compound materials, consisting of two-component mixtures of various types of materials, including metals. Finally, we will present a short review of current research into the field of nanoplasmonics.

3.1 Drude Model of Electric Permittivity

Dielectric materials are characterized by real-valued electric permittivities which do not vary much over a broad range of wavelengths. In metals, we need to account for the conduction electrons with elementary charge e which can move across the metal under the influence of an external EM field. The optical properties of metals arise from these movements and are well explained over a wide range of frequencies by the *plasma model* [21]. This model describes mathematically the movement of *free electron gas* on a fixed background of positive ion cores. However, this model does not account for the band structure and electron-electron interactions, which causes noticeable differences between the measurements and calculated values at short wavelengths (see Fig. 3.1). Certain aspects of the band-structure can be accounted for using the so-called adjusted *optical mass* of the

electrons m[21]. In metals, the imaginary part of the electric permittivity function $\mathrm{Im}(\epsilon)$ is considerably large. More importantly, its real part $\mathrm{Re}(\epsilon)$ is negative, and can also be very large. This negative value of the real part of the electric permittivity is essential to the presence of plasmonic resonances in metal nanostructures. The electrons oscillate in

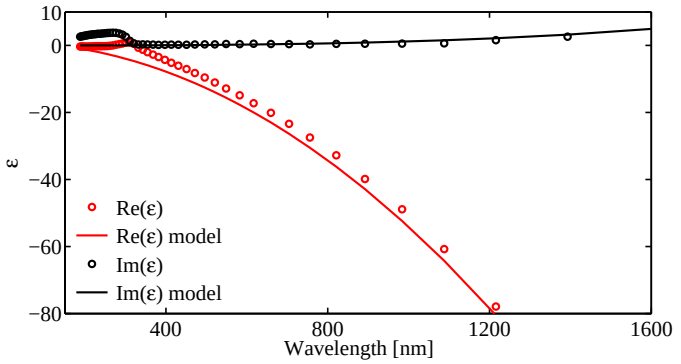

Figure 3.1 Measured permittivity function of silver (circles), taken from *Johnson and Christy*[61] and lines fitted with the Drude model (Equation (3.1)).

response to the external EM field. The movement of these electrons is governed by a simple equation of motion[21], from which we can derive the complex electric permittivity:

$$\epsilon(\omega) = 1 - \frac{\omega_p^2}{\omega^2 + i\gamma_D\omega}, \tag{3.1}$$

where ω is the angular frequency of the applied EM field, $\omega_p = \sqrt{ne^2/\epsilon_0 m}$ is the plasma frequency of the free electron gas and it depends on the density of electrons in metal n and the damping rate γ_D caused by the collisions of the free electrons with the lattice ions (relaxation time of the free electron gas which is typically on the order of 10^{-14} s at room temperature). Typical values of the plasma frequencies of different metals vary in the range of ultraviolet to visible parts of the EM spectrum. For the calculations for silver with Eq. (3.1) presented in Fig. 3.1 as lines, we use ω_p=1.4×10^{-16} s^{-1}, and the damping rate γ_D=4.1×10^{-13} s^{-1}.

Equation (3.1) can be presented in a different form by separating the real and the imaginary parts:

$$\epsilon(\omega) = 1 - \frac{\omega_p^2}{\omega^2 + \gamma_D^2} + i\frac{\omega_p^2\gamma_D}{\omega(\omega^2 + \gamma_D^2)}. \tag{3.2}$$

With this form, we see that at low frequencies, such that $\omega < \sqrt{\omega_p^2 - \gamma_D^2}$, the real part

of ϵ is negative, which explains high reflectivity in the visible and infrared. For very high frequencies on the other hand, the permittivity function approaches unity, which implies transparency for short wavelengths, like X-rays.

3.2 Plasmon Resonances

Plasmon resonances in metal nanostructures arise from the collective, resonant oscillations of the conduction electrons. These resonances play an essential role in the optical properties of systems of metal nanoparticles. Plasmon oscillations can be categorized into three different modes, depending on the applicable boundary conditions: volume, surface, and localized surface (or particle) plasmons, which are all schematically illustrated in Fig. 3.2. Volume plasmons (see Fig. 3.2(a)) are collective oscillations of the conduction electron

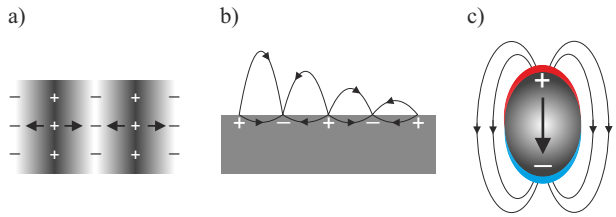

Figure 3.2 Different modes of plasmon resonances. a) Volume plasmon, b) surface plasmon, and c) localized surface plasmon (particle plasmon).

gas in a bulk metal. These resonances are not confined, and cannot be directly excited with an electromagnetic wave. The experimental studies of this type of resonances are usually performed by electron loss spectroscopy[21,62].

Surface plasmons (or surface plasmon polaritons) occur at dielectric-metal interfaces. In essence, these resonances correspond to the oscillations of the longitudinal charge density confined in one dimension. Considering the directional plasmon propagation along metal surfaces, the wave equation yields two possible propagation modes, transverse magnetic (TM), and transverse electric (TE). Due to the boundary conditions at the interface between metal and dielectric, only TM modes may excite surface plasmons. Moreover, the only allowed TM modes must fulfill the dispersion relation:

$$k_{SP}(\omega) = k_0(\omega)\sqrt{\frac{\epsilon_m(\omega)\epsilon_d}{\epsilon_m(\omega)+\epsilon_d}}, \tag{3.3}$$

where $k_{SP}(\omega)$ is the propagation constant of the surface plasmon, k_0 is the propagation constant of the applied fundamental field, $\epsilon_m(\omega)$ is the electric permittivity function of the metal, and ϵ_d is the dielectric constant of the surrounding dielectric material. The direct consequence of the dispersion relation 3.3 is that surface plasmons can only exist for opposite signs of the real parts of $\epsilon_m(\omega)$ and ϵ_d. For the case of a metal surrounded by dielectric material, this condition is always satisfied as the permittivity function of metals has negative real values in the visible and near-infrared spectral regions as shown in the previous section (see Fig. 3.1), and dielectrics, e.g., glass, always possess a positive dielectric constant. The above condition also implies that the electric waves decay exponentially perpendicular to the surface. Moreover, the dispersion relation also implies that the surface plasmon and the excitation field have different wavevectors. Therefore, surface plasmons cannot be excited by light propagating in free space, but special phase-matching techniques, e.g., using a prism (Kretschmann or Otto configuration), or diffraction grating, are needed to effectively couple light to surface plasmons[21].

Metal nanoparticles are three-dimensional structures, whose sizes are of the order of the wavelength of the excitation field or less. The oscillations of the conduction electrons inside such structures are confined in all three dimensions, and are referred to as localized surface plasmons (or particle plasmons). The interaction of the applied field with a collection of metal nanoparticles can be described by an electromagnetic scattering problem. However, existing analytical solutions are limited to spheres, spheroids, and ellipsoids[10,21,63]. The approximated optical response of the collection of particles much smaller than the wavelength of the incidence field can be obtained with the quasi-static approximation[21]. In such case, the sizes of individual particles and the distance between them is much smaller than the wavelength of the incoming light, which means that the EM field can be treated locally as a constant. Within this approximation, a spherical particle in a static EM field is characterized with a polarizability α[21]:

$$\alpha = 4\pi r^3 \frac{\epsilon_m(\omega) - \epsilon_d}{\epsilon_m(\omega) + 2\epsilon_d}, \tag{3.4}$$

where the particle radius is r, $\epsilon_m(\omega)$ is the electric permittivity of the metal (complex valued) and ϵ_d is the dielectric constant of the surrounding dielectric material (real valued). The permittivities have opposite signs such that when the real part of the metal particle permittivity fulfills the condition $\mathrm{Re}[\epsilon_m(\omega)] = -2\epsilon_d$, the polarizability is maximum. This is the so-called Fröhlich condition, which is associated with the small particle plasmon resonance. This approximation is valid only for particles with sizes smaller than approximately

100 nm. The polarizability resonance described by Eq. (3.4) also yields the enhancement in the local EM fields, which is limited by the imaginary part of the permittivity function of metal (denominator is never equal to 0). The resonance frequency can be estimated from the Drude model (Eq. 3.2), and it occurs at the frequency:

$$\omega_0 = \frac{\omega_p}{\sqrt{1 + 2\epsilon_d}}, \tag{3.5}$$

which implies that the resonance frequency depends on the dielectric medium surrounding the metal nanoparticle. The resonance frequency will red-shift with an increasing refractive index (increasing dielectric constant) of the surrounding medium.

Beyond the electrostatic approximation, for particle sizes larger than 100 nm, a more rigorous electrodynamic model is required. The first explanation of the scattering and absorption of EM fields on spherical metallic particles suspended in water, which sizes are not limited, was formulated by Gustav Mie in 1908[8]. The proposed model utilizes the solutions of the vector wave equations in a spherical coordinates, and whose describes the local scattered field as a sum of the contributions from electric and magnetic multipoles.

3.3 Maxwell Garnett Model of the Effective Medium

The theory of the *effective medium* describes the electric permittivity function for a mixture of two or more different constituents. One of the simplest effective medium theories was developed by Maxwell Garnett for the nano-spherical inclusions embedded in a host material[7]. The schematic illustration of such a composite medium is illustrated in Fig. 3.3. The spherical solid inclusions with sizes smaller than the wavelength of the incident

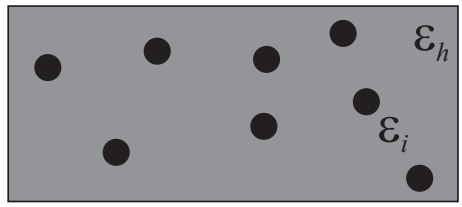

Figure 3.3 Schematic illustration of Maxwell Garnett effective medium, spherical inclusions with electrical permittivity ϵ_i inside a host medium with permittivity ϵ_h.

light can be dielectrics, semiconductors, or metals. The particles embedded inside the

host material are further assumed to have a random distribution. In the case where the linear refractive index of the nanospheres is lower than that of the nonlinear host material, enhancement of a nonlinear process is possible due to the local fields which can be extremely strong inside the spherical particles[9]. The Maxwell Garnett theory of the effective medium is the simplest one, but it is nevertheless the most successful in modelling of effective media, with many modifications accounting for different types of materials and nonlinear effects[9,10,29,64,65]. In this thesis, the inclusions embedded in the host material are nanoparticles made of metal, whose approximate electric permittivity function can be estimated with the Drude model (Eq. (3.1)), or measured experimentally[61]. With the assumption that the volume fraction, or fill factor, f_i is relatively small (i.e. $f_i \ll 1$), the linear effective dielectric function ϵ_{eff} fulfills the relation[7]:

$$\frac{\epsilon_{eff}(\omega) - \epsilon_h(\omega)}{\epsilon_{eff}(\omega) + 2\epsilon_h(\omega)} = f_i \frac{\epsilon_i(\omega) - \epsilon_h(\omega)}{\epsilon_i(\omega) + 2\epsilon_h(\omega)}, \tag{3.6}$$

where $\epsilon_i(\omega)$ stands for the permittivity function of the inclusions (nanoshperes) and $\epsilon_h(\omega)$ is the electric permittivity of the host material. Equation (3.6) can be rewritten in the more convenient form:

$$\epsilon_{eff}(\omega) = \epsilon_h(\omega) \frac{1 + 2\delta(\omega) f_i}{1 - \delta(\omega) f_i}, \tag{3.7}$$

where the factor $\delta(\omega)$ is given by:

$$\delta(\omega) = \frac{\epsilon_i(\omega) - \epsilon_h(\omega)}{\epsilon_i(\omega) + 2\epsilon_h(\omega)}. \tag{3.8}$$

The above relations can be used to estimate the complex dielectric function of the metal nanoparticles embedded in a dielectric host material. The effective permittivity function can take complex values due to introduction of the metal into the host dielectric material. However, Maxwell Garnett approximation does not account for the interactions between the nanoparticles or for the scattering of the incident light. Furthermore, the model assumes that the effective medium is highly homogeneous and that the random distribution of nanospheres does not create agglomerates. The model is also independent of the particles size and their spatial separation.

The Maxwell Garnet model has been extended to account for the nonlinear effects[9,29]. According to these extensions, which take into account the nonlinearities of both host and inclusion materials, the nonlinear properties of the composite material can differ significantly from those of its constituents, and moreover, under proper circumstances, they can

exceed those of its constituent materials.

3.4 Review into Nanoplasmonics

The interest in the optical properties of nanoscale particles and structures utilizing various materials is increasing every year. Research in the field of nanoplasmonics focuses on nanoscale structures made of metal. There are many challenges in this expanding field. As the size of the nanoparticles approaches the skin-depth of metals ($\sim$ 20-30 nm), the classical approach of scaling down the bulk material properties is insufficient to provide a complete description of the optical properties[66]. The optical responses (linear and nonlinear) of metal nanostructures are determined by their plasmon resonances, which are strongly dependent on particle sizes, dielectric environment, as well as their mutual orientation. With the recent fabrication techniques, the characteristics of the nanostructures can be controlled with high precision, and even though the analytical theories for the optical response of nanoparticle systems are limited to simple geometries, the experimental investigations of more complex structures give valuable insight into the underlying physical processes. In this section, we briefly discuss recent work in the field of nanoplasmonics.

Metamaterials

Meatameterials consist of artificial periodic structures at the nanoscale[67]. They are one of the most promising structures in optical engineering with a broad range of very interesting and exotic applications including lenses utilizing negative refraction, light confinement below the diffraction limit[25], optical cloaking devices manipulating the light in a way that allows to render objects invisible[68,69]. Recent advancements in the modeling of such structures allowed for a successful demonstration of a functional cloak in the micro-waves regime[70].

According to the above definition, all structures containing nanoscale elements are metamaterials, but some researchers use a stricter definition and relate metamaterials only to those exhibiting magnetic resonances and a negative refractive index. In this case the real parts of either the permittivity function ϵ or magnetic permeability μ or both must be negative. As already mentioned, most metals possess negative real part of the electric

permittivity function over a broad range of optical frequencies, and if the real part of the permeability μ is also negative, the index of refraction becomes negative. The optical characteristics of metamaterials can be tailored by changing the shape and size of individual particles, however it might be further modified by changes in the mutual arrangement of the particles in the structure[71].

Similarly to the case of negative electric permittivity described in the previous section, a negative real part of the magnetic permeability, leads to the presence of magnetic resonances. The excitation of those in the optical regime, however, still requires special techniques and design, i.e., coupling via electric component of the incident light to a split-ring resonator[72–74]. These types of resonances can affect the efficiency of SHG generation. For example it was reported that split-ring resonator structures can give rise to SHG enhancement via the excitation of magnetic resonances[33,75]. Also, the combination of magnetic and electric responses leads to nonlinear magnetization[48] and are useful in explaining the effect of optical activity of materials[76].

With a number of different designs for metamaterials, a very important part of research is only concerned with the optimization of such structures to obtain negative refractive indices for a broad spectrum of optical frequencies. In fact, different types of structures possessing negative refractive index have already been reported. Negative refraction at 15 GHz was reported in a structure consisting of simple pairs of conductive wires[77], as well as in the near infrared (2 μm) in structures with fishnet geometry[78], or at 1.5 μm in a structure consisting of nanorod pairs[72]. The optimization of the design of metamaterials and the recent progress in fabrication methods have allowed demonstrating materials with negative index of refraction close to visible wavelengths[79–82].

Surface-enhanced Effects

Inelastic Raman scattering in molecules, and a second-harmonic generation are typically relatively weak processes. However, the effective cross-section of Raman scattering for both absorption and emission is enhanced in the presence of strong local fields. Such strong local-field enhancement can be provided by the presence of metal nanoparticles on a surface, from which the signal can be anhanced up to several orders of magnitude. This surface geometry is called *surface-enhanced Raman scattering* (SERS). The first observation of the phenomenon was performed on roughened silver surfaces in 1974[83].

Apart from rough surfaces, the effect can be obtained by using metamaterials, which allow optimization of the resonance conditions. Some of these methods utilize for example: arrays of bridged nanocones[84], gold-silica nanoshells in a solution[13], silver particles in a solution[85], etc. The same applies for the case of second-harmonic generation, so that the strong local fields confined in the nanopartiles can lead, under proper conditions, to the enhancement of the nonlinear process[30,58].

Nanoapertures

Complementary to the studies of metal particles in nanoscale, the nanoscale apertures in a thin metal films have been also investigated. Elementary considerations might lead to the conclusion, that the field cannot pass through an aperture with dimensions smaller than the wavelength of the incidence field[86]. However, studies show that an arrays of sub-wavelength apertures in metal films can lead to enhanced transmission[86–88]. The peaks of the transmission in such an arrays occur at wavelengths much larger than the diameter of the apertures. Moreover, the transmission normalized to the area of the apertures can be larger than one. The original explanation to these results were the plasmon resonances induced by the coupling effects between the incoming field and the periodic structure[88]. Later, an alternative explanation was proposed according to which the enhanced transmission would result from a wavegiude-mode resonance diffraction[89].

Nanoapertures can provide the detection enhancement of single molecule fluorescence. The enhancement factors of the fluorescence count rate per molecule up to 120 fold were reported[90,91]. Moreover, the emission of the fluorescence was found to be directional into a narrow angular cone in the direction normal to the sample plane. Such results are highly relevant for the development of single molecule sensing, single-photon sources, and light emitting devices, and they form an original tool to characterize and optimize the plasmonic response of metal nanostructures.

We also find reports on the second-order nonlinear response of the nanoaperture arrays. Similar to the case of nanoparticles, the second-harmonic response of the nanoapertures has been found to depend on the symmetry and arrangement of the apertures[92]. It is most interesting that the SHG signal levels measured for the traditional and complementary split-ring resonators have been found to agree very well with each other[93].

Nanoantennas

The concept of nanoantennas is the equivalent of the radio-, or micro-wave antennas, capable of controlling coupling between the near- and far-fields[94]. They can also be interpreted as the equivalent of a nanolens that focuses the electromagnetic energy beyond the diffraction limit. The key mechanism utilized in such structures is the local-field enhancement. The most simplistic optical nanoantennas are dipolar nanorods[95]. Systems of nanodimers, which are essentially pairs of nanoparticles in close proximity, can change their resonance conditions due to interparticle coupling. These changes can be explained due to plasmon hybridization effects[96]. One of the examples of such structures are bow-tie nano-dimer antennas which focus light beyond the diffraction limit[97,98]. The same effect was predicted and experimentally demonstrated in self-similar chains of metal nanoparticles[99–101]. Nanoshells, which posses well-distinguished multipolar radiation patterns depending on the excitation wavelength, are also used as optical antennas[102]. Antennas with unidirectional emission patterns have been reported[103], as well as a row of nanorods, which act as an optical Yagi-Uda antenna[104,105]. Coupling can be also done by utilizing the lightning-rod effect, which relies on sharp features of nanostructures, like tips or nanogaps[106,107].

Plasmon Sensors

Plasmon resonances of metal nanostructures depend on their shape, size, mutual arrangement, and, of course, the surrounding medium. This particular property of plasmon resonances is used for sensing applications. The shift in the plasmon resonance frequency, which depends on the surrounding medium[23,24], provides information on the presence of different type of surrounding media, and the magnitude of the shift can deliver information on the change in the refractive index. Sensors based on surface plasmons can be realized by analyzing the angular dependence on the excitation by scanning the outgoing field[108]. Improvements in the sensitivity have been reported by using multi-wavelength excitation[109]. Also, similar as in nanoantennas, coupling effects in dimer systems or arrays of particles can lead to stronger confinement of the fields, which then increases significantly the sensitivity compared to the case of a single nanoparticle[110].

Nonlinear Optics

The most commonly used metals in nanoplasmonic research are silver and gold. These metals posses a face-centered cubic crystal symmetry, and therefore a center of symmetry. This implies that electric-dipolar SHG process is forbidden in the bulk of these metals. Since the existing fabrication methods, especially the lithographic ones, are not capable of forming bulk monocrystals, the resulting random collection of nanocrystals effectively increases symmetry even more. However, it is always broken at the interfaces between two different media, e.g., the metal-dielectric interface, allowing electric-dipolar second-harmonic generation from metal surfaces or two dimensional arrays of metal nanoparticles[45].

Nonlinear processes, which scale with a high power of the incidence field can be enhanced by the presence of strong local fields which arise from plasmon resonances. The original inspiration for SHG enhancement with strong local fields actually came from the discovery of surface-enhanced effects in Raman scattering. Enhancements of the order of four orders of magnitude were obtained on rough silver-air interfaces[30,111]. Such enhancements, similar to the SERS effect, can be further optimized by the use of metal nanostructures whose resonances can be tuned to the desired wavelength. SHG enhanement in systems of metal nanoparticles was also reported[58,59,112,113]. Moreover, SHG from metal nanoparticles with proper design can exceed up to several orders of magnitude the SHG from a thin metal surface[63,114]. Remarkably strong field confinement occurs also for sharp features of metal nanostructures (e.g., sharp tips or edges of metal structures), which also increases the efficiency of the SHG process. Studies of SHG generation on sharp metal tips have shown that the interactions between the tip and a surface in proximity significantly modify the enhancements of the SHG signals[115], such that e.g., the field near a sharp metal tip can be strongly enhanced if irradiated with an optical field polarized along the tip axis. This effect can be utilized to map the local field distributions at the surfaces[116].

We have emphasized the dependence of the plasmon resonances on the features of the metal nanostructures and the optimization of metal nanostructures for a specific application therefore depends on the dimension of a single particle and their mutual interactions. All these parameters determine the resonances and coupling effect of the effective medium. For SHG, it is essential to break the inversion symmetry, which forbids electric-dipole interactions, which are the dominating ones. That implies that both individual particles, as well as the effective structure, must not have a center of inversion. The simplest example of such structure is a regular array of L-shaped nanoparticles. In this thesis we address the

effects arise from imperfections that can be present in nanostructures and arising during fabrication. Such defects are found to significantly influence the nature of the generated SHG field, and we connect them with multipolar contributions to the SHG signal. Analysis performed by Stockman et al. on the basis of Green's function theory show that the effect of nano-scale roughness are localized SH fields (hot-spots) which are strongly incoherent [58]. These unintentional defects also act as symmetry-breaking agents, leading to the presence of symmetry forbidden signals in the generated radiation, which was presented in **Publication 1**. Experiments with such structures were performed in our lab in recent years, raising interesting points with regard to the quality of the structure. In Particular, high quality structures suppress the multipolar contributions to the SHG, which is one of the topics presented in this thesis in **Publication 2**. Similar structures were also investigated elsewhere, and it was demonstrated, that the decay time of plasma oscillations in silver nanoparticles is larger than expected from the bulk metal dielectric function [117]. Recently, a new concept for tailoring the second-order nonlinear response such arrays of L-shaped metal nanostructures was proposed, by simply controlling the mutual orientations between the particles [71]. It is also possible to modify the electromagnetic modes in such structures by introducing passive elements which act like fundamental field coupling antennas, therefore increasing the efficiency of the SHG process [118]. Symmetry breaking is also possible in multi-layer bulk-type materials, in which layers of centrosymmetric metal nanostructure are separated by layers of pure dielectric material. SHG experiments in such a medium are presented in this thesis, and were reported in **Publication 3** with the detailed analysis of the susceptibility tensor of the structures in **Publication 4**.

Another interesting structure is a metal nanoparticle with the shape of the letter T. The nanodimers, in which perpendicular bars are separated from each other by a gap with size of the order of tens of nanometers, cause asymmetrical field confinement for the excitation along the axis of symmetry of the T-shaped particle, which in effect increases SHG efficiency [119,120]. This field asymmetry was found to be of more importance for SHG generation than the strong local fields themselves.

The local field enhancement in metal nanostructures can also be beneficial to other nonlinear processes such as four-wave mixing in a system of coupled gold nanoparticles [121], where it was shown that the efficiency of the process was enhanced by up to four orders of magnitude. The effect was attributed to the shift of the localized plasmon resonance towards the infrared wavelengths for decreasing distance between the particles. The enhancement occurs up to the point of physical contact, when the resonance of particles changes due

to a contact, which creates effectively a single, larger particle. Surface plasmons can also be excited nonlinearly with use of the four-wave mixing process[122]. The report states that the surface third-order susceptibility dominated the process, rather than the bulk one. There are also reports of third-harmonic generation (THG) from the metal structures and gratings[75,123–125]. With the plasmon resonance excited in the structure, the THG signal was found to be enhanced by several orders of magnitude. Yet again, the enhancement of THG generation can be optimized by tailoring the driving resonances with the proper nanostructure design.

The effective medium theory for small metal nanoparticles embedded in a host material and which accounts for the third-order nonlinear effects was proposed by Boyd and Sipe[9]. In this theoretical model the concept of Maxwell Garnett effective theory is extended to account for the third-order nonlinear response. The nonlinear susceptibility of a composite optical material consisting of spherical inclusions embedded in a host material is determined, and both constituents are allowed to respond nonlinearly and to exhibit linear absorption. More to that, each constituent and the resulting composite is assumed to be isotropic. Proposed model has shown that the third-order nonlinear susceptibility may be altered significantly and in particular that the effective susceptibility of the composite medium can exceed the nonlinearity of its constituents.

One of the most promising concepts for nonlinear optics in nanostructured, engineered optical materials are optical zero-index materials where phase-matching is automatically fulfilled[126,127]. Phase mismatch between distributed, microscopic sources in a nonlinear material prevent them from combining constructively, which limits the growth of the nonlinear signal, and quasi phase-matching techniques are needed to compensate for this effect. Experimentally demonstrated phase mismatch-free material simply cancels out this problem, as the propagation in the optical zero-index material does not alternate the phase of the incidence field, allowing efficient nonlinear generation in both forward and backward directions[126].

The progress in understanding the physical mechanisms governing the optical properties of metal nanostructures together with the development of more sophisticated models allows to develop new and more accurate methods for the fabrication of metamaterials. With the possibility of manipulating single atoms, creating mono-layers of atomic materials, building up complex structures in nanoscale, the fascinating prospects to manipulate and control light on the nanoscale are becoming a reality. Combination of theoretical knowledge with engineering know-how, will open the possibility for the composition of engineered,

customized multi-component composite materials with remarkable, highly controlled properties.

Chapter 4

Samples and Experiments

In this chapter we describe the samples investigated in this thesis, explain their methods of fabrication and introduce the experimental setups used to characterize their linear and nonlinear optical properties. We also describe the theory and models used for the analysis of the measurement results.

4.1 Fabrication Methods

The samples investigated in this thesis were prepared with two different fabrication methods and of two different metals. The first set of samples (**Publications 1 & 2**) are L-shaped metal nanoparticles arranged in a planar, regular array. The L-shape shape is one of the simplest structures with no centrosymmetry in two dimensions. The L-shaped samples were made of gold because this metal is very well suited for the excitation of particle plasmons. Moreover, gold does not oxidize when subject to normal laboratory conditions. The first set of samples was prepared with electron-beam lithography (EBL) method. Although this fabrication process is very complex, it allows fabricating nanostructures with nm-scale precision.

The second set of samples was prepared by aerosol synthesis, a much simpler technique but which also allows to collect nanoparticles with custom sizes at the nm-scale. In aerosol

synthesis, spheroidal metallic particles are synthesized in a constant flow of nitrogen. The technique allows for controlling the size of the particles and by adjusting the deposition time one can also control concentration. More complex structures can be fabricated by introducing intermediate processes, e.g. separating the layers of metal particles with a layer of dielectric material.

Electron Beam Lithography

The L-shaped gold nanoparticle samples were fabricated at the University of Eastern Finland by our collaborators using electron-beam lithography (EBL) followed by lift-off process. The main advantages of this fabrication method are versatility and high precision. The possible shapes and arrangements of nanoparticles in planar arrays are limited only by achievable parameters and imagination. This method allows us to create patterns beyond the diffraction limit of the feature size imposed by conventional optical lithography tools used in the electronics industry. Achievable line widths with the EBL technique are of the order of tens of nanometers: there are reports of a fabrication of 10 nm lines[128], and recently of a lines as fine as 5 nm[129]. The main drawback of the EBL fabrication method is that the process is extremely slow; it can take even up to several hours to expose a single 1×1 mm area. Moreover, the equipment is highly sensitive to calibration, which may result in low repeatability of the fabrication process.

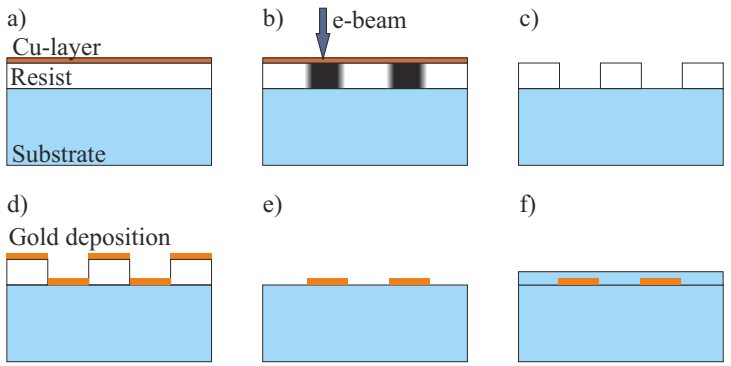

Figure 4.1 Sample fabrication with electron-beam lithography. a) Deposition of copper and resist layers, b) electron-beam writing, c) development of the structure, d) deposition of gold layer, e) lift-off process, and f) glass cover layer deposition.

The process itself consists of several steps, which are presented schematically in Fig 4.1.

First, a layer of the electron-beam sensitive resist is applied on top of the substrate, together with a thin (c.a. 20 nm) layer of copper, which prevents the sample from being electrically charged during the electron-beam writing process. The pattern of the nanoparticle array is recorded directly by e-beam. The irradiated parts of the resist layer together with the discharging layer of copper are removed in the next stage. The resulting structure is next covered with a thin adhesion layer of chromium and a 20 nm layer of gold. In the final stages of the fabrication, the rest of the resist layer is removed in a lift-off process, leaving only the gold nanoparticles patterns, which are finally covered with a 20 nm protective layer of glass.

Aerosol Synthesis

The samples made by the aerosol techniques were prepared in cooperation with the Aerosol Physics Laboratory of Tampere University of Technology. Aerosol techniques are much cheaper than EBL fabrication; also, the fabrication process is considerably faster. The main limitation of this method is the resulting shape of the created nanoparticles, which, due to surface tension of the floating aerosol particles, can only be sphere-like. The main advantage over similar fabrication methods such as ion implantation[130], sputtering[36], pulsed laser deposition[131], and wet chemical techniques[132], is that the achievable particles size covers practically the whole nanoscale from a few nanometers to over 100 nm[37], whereas with the aforementioned methods the size is limited to below $\sim$ 30 nm. The particles are generated by an evaporation-condensation technique followed by size selection and sintering. In the end of the process the synthesized particles are gathered on a glass substrate as shown schematically in Fig. 4.2. The process allows controlling the average

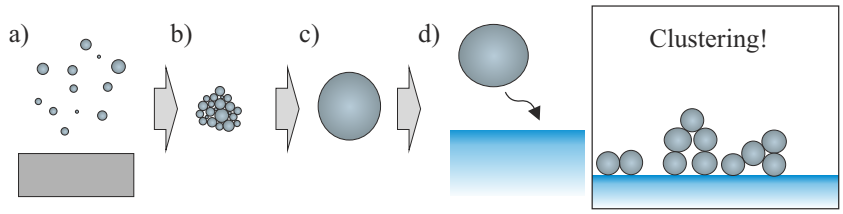

Figure 4.2 Aerosol synthesis of metal nanoparticles. a) Evaporation of bulk silver, b) condensation and size selection, c) sintering to form a particle, d) deposition on a glass substrate. Inset: clustering of the metal nanoparticles.

size of the deposited particles as well as the size dispersion. However, the resulting structure

can exhibit agglomerates of charged silver nanoparticles for large concentrations (see inset on Fig. 4.2). It was reported that such clustering is responsible for the inhomogeneous broadening of the plasmon resonance of the collection of particles, which is more apparent in samples with high concentration of metal nanoparticles[37]. To overcome this problem, the method was modified and it is this modified method that was used in the samples of this work (**Publications 3 & 4**). Here we use additional dielectric carrier particles consisting of silica glass with a size of the order of 50 nm. Nanodots made of silver are deposited on top of the carrier particles via evaporation and condensation. The resulting structure is then collected on top of a glass substrate with an electrostatic precipitator. The process is shown in Fig. 4.3. This modified method allows for the deposition of a virtually unlimited

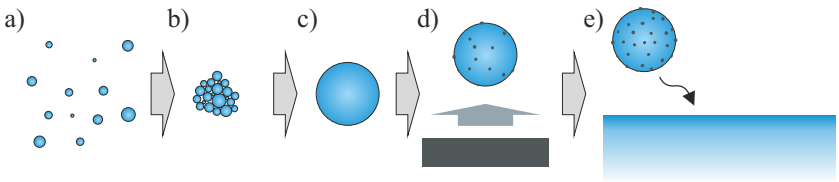

Figure 4.3 Aerosol synthesis of silica nanoparticles decorated with silver. a) Prefabricated silica particles in a constant flow of nitrogen, b) formation of silica clusters and size selection, c) sintering to form a silica particle, d) evaporation and condensation of silver "decoration," and e) deposition of the particles on top of a substrate.

amount of particles on a substrate while preventing clustering of the metal nanoparticles and therefore canceling out the effect of the inhomogeneous broadening of the plasmon resonance.

The metals used, gold and silver, have both good plasmonic properties. When considering the interband transitions, silver is even better than gold. The interband transitions for gold occur already in the visible region (620 nm), whereas for silver they occur below 330 nm. Another advantage of silver is its lower damping rate, which affects the plasmon resonance[133,134]. However, silver is chemically active under normal laboratory conditions and therefore oxidizes, which can alter the properties of a sample with time. Gold, on the other hand, is chemically stable, allowing for samples with stable optical properties.

4.2 Samples

Arrays of L-shaped Nanoparticles

The first sample investigated is presented in Fig. 4.4 and consists of a regular array of the L-shaped nanoparticles. The particles have one axis of symmetry along the x-direction. The lengths of both arms of a single L-particle is 200 nm, both arms are 100 nm wide, and the thickness of the particles is 20 nm. The particles are arranged in a regular array with a period of 400 nm and total area of 1×1 mm. The size of the particle was chosen to yield a plasmonic resonance at the 1060 nm wavelength of the laser used for the SHG experiments. It is clear from Fig. 4.4 that the sample quality is relatively low. As

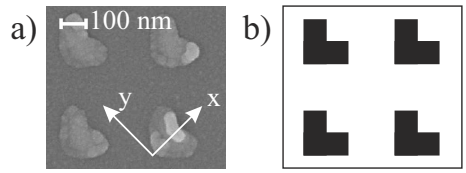

Figure 4.4 L-shaped nanoparticles with low quality. a) SEM image of the structure with the coordinate system, b) schematic image of the fabricated structure.

mentioned in Chapter 3, defects brings to the overall SH response contributions from the higher-order multipoles. The measurements that reveal the multipolar nature of the SHG generated from such low-quality samples are reported in **Publication 1**. This particular sample was fabricated several years ago, and there has been since significant improvement in the fabrication method. This improvement was obtained with a new EBL system, which possesses higher accuracy and stability. Improved line quality was achieved by a smaller step size for the e-beam, and due to an increase in the speed of writing the structures, this reduced step size did not increase the fabrication time of the structure. A similar sample but with higher quality is presented in Fig. 4.5. This sample has an almost identical

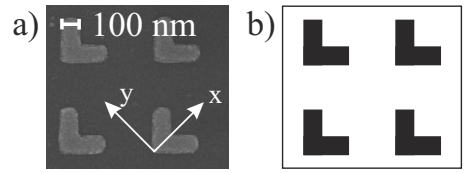

Figure 4.5 L-shaped nanoparticles with high quality. a) SEM image of the structure with the coordinate system, b) schematic image of the fabricated structure.

structure, but with slightly different dimensions. The width of the L-particle arm is 100 nm, the length is 250 nm, and the period of the regular array in the new sample is 500 nm. Comparison between the SHG signals from both low- and high-quality samples, is the topic of the **Publication 2**

Nanocomposites Fabricated with Aerosol Techniques

In the second part of this thesis, we characterize samples fabricated by aerosol techniques where we introduced a structure in the direction perpendicular to the substrate surface. The size of each silica carrier particle is controlled to be 50 nm. On top of the carrier particles, silver nanodots are deposited with sizes of up to 5 nm. The fabrication process of all the investigated samples is shown schematically in Fig. 4.6. The starting point is a clean, glass substrate, on top of which the nanoparticles are deposited (see Fig. 4.6(a)). The amount of the deposited particles is determined by the deposition time. The nanoparticle layers are covered with a layer of fused silica with the use of electron-beam dielectric coater (see Fig. 4.6(b)). During this process, the beam of electrons evaporates silica from the bulk, which is next deposited on top of the nanoparticles. The resulting structure is then the staring point for the deposition of the next layer of aerosol-synthesized particles and so forth. Samples with a desired number of deposited layers are created simply by repeating

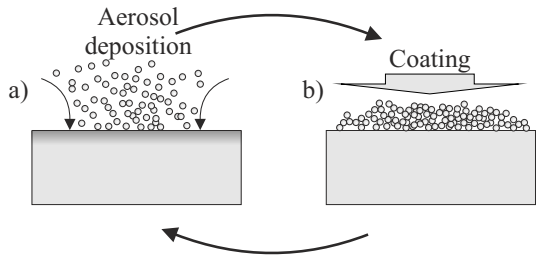

Figure 4.6 Aerosol sample fabrication method. a) Deposition of the silver decorated silica nanoparticles, b) deposition of the fused silica layer with the electron beam dielectric coater. In order to create multilayer structures, we repeat the procedure in cycles, as marked on a figure.

steps (a) and (b) shown in Fig. 4.6. For the purpose of the work presented in this thesis, we prepared samples which are characterized by different numbers of almost identical layers, as well as control samples which allow us to confirm the nonlinear effects observed in the multilayer structures. The investigated set of samples is presented in Fig. 4.7. A single layer of the nanocomposite deposited on top of a glass substrate is 800 nm thick and the

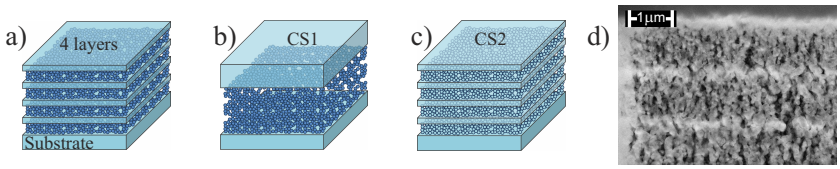

Figure 4.7 Multilayer samples prepared with aerosol techniques . a) Sample with deposited four layers (the number of layers in the experiments presented is from 1 to 4), b) control sample CS1 with the thickness equivalent to the sample with four layers deposited, c) control sample with four layers, but no silver decoration, d) transmission electron microscope image of the resulting structure.

subsequently deposited layer of glass is 200 nm, which gives a thickness of one full layer to be 1 μm. Transmission electron microscope image of the fabricated structure is shown in Fig. 4.7(d) where the different layers can be identified. Control samples CS1, which contains the silver inclusions, but only one thick layer, and CS2, which posses four layers of nanoparticles without the silver decoration, were prepared to validate the nature of the nonlinear responses measured for the multilayer structures (see Fig. 4.6 for illustration).

4.3 Characterization of Linear Optical Properties

The linear properties of the samples are important, as they directly influence the nonlinear response of the structures. The linear optical properties of the L-shaped nanoparticle arrays and nanocomposite samples are determined with measurements of the extinction spectra. The extinction spectra account for both absorption and scattering of the samples, as they cannot be separated from each other in the setups used for the measurements. The extinction measurements for the L-shaped nanoparticles were performed at normal

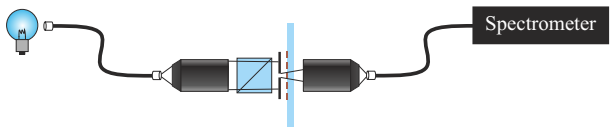

Figure 4.8 Setup for the measurement of the extinction spectra of L-shaped particles.

incidence with a broadband tungsten halogen light source as shown in Fig 4.8. The halogen lamp emits light in the spectral range from 350 nm to 1650 nm, and the spectrum was measured with Avantes AvaSpec-2048 spectrometer covering the spectral range from 400 to 1700 nm. The light from the source was guided in multimode fiber and was

collimated with a microscope objectives through a pinhole with 500 μm aperture. The pinhole allows illuminating only the sample area whose size is 1×1 mm. A polarizer was inserted before the pinhole to control the polarization state of the incident light. The measurement was performed in two stages. First the spectrum is measured for a clean substrate only (glass). In the second step, the extinction spectrum of a given sample with nanoparticles is measured from which that of the clean substrate is subtracted.

The linear properties of the samples fabricated with aerosol techniques were measured with a high-sensitivity, high-resolution, fully automated UV-Vis-IR Shimadzu UV-3600 spectrometer. Because the samples consists of a collection of spherical particles with random arrangement creating an isotropic surface, there was no need to perform measurements for different polarization states in this case.

4.4 Second Harmonic Generation Experiments

The characterization of the second-order nonlinear properties of the samples was performed by second-harmonic generation experiments. In the experiments with L-shaped nanoparticles, we used as the excitation source a femtosecond Nd:glass laser (200 fs pulse duration, 82 MHz repetition rate), operating at 1060 nm. The measurement setup used for the nonlinear experiments with the L-shaped nanoparticles is illustrated in Fig. 4.9. The average power of the fundamental beam before the sample was 80 mW. The beam

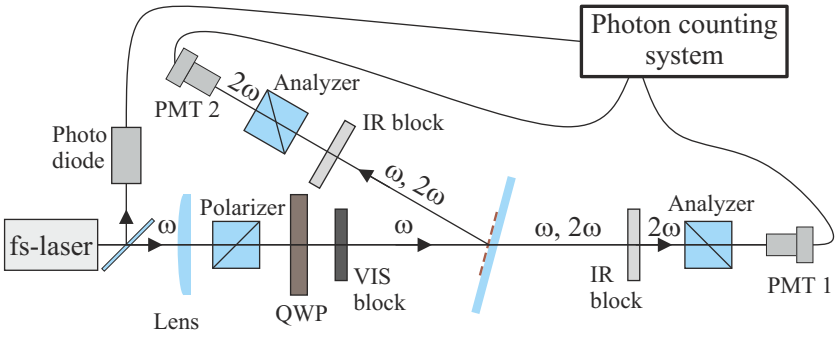

Figure 4.9 Experimental setup for the measurement of second-harmonic generation from L-shaped nanoparticles.

was weakly focused with a 300 mm focal length lens onto the sample, resulting in a spot size of about 300 μm. Any SHG radiation that could be generated by optical components

before the sample was removed by a filter (VIS-block) placed just before it. The state of polarization of the fundamental beam was controlled with a polarizer which is transmits the linear p-polarization (in the plane of incidence). During the measurements, the state of polarization was modulated continuously with a quarter-wave plate (QWP) mounted on a computer-controlled motorized rotation stage. In order to simultaneously measure the transmitted and reflected SHG signals, the sample was slightly tilted off normal with respect to the fundamental beam (around 1°). Several tests were performed to verify that such a small angle does not cause coupling of the fields with the sample normal direction (z)[32,42]. In the measurements for the L-shaped nanoparticles, we can thus relate the s- and p-polarization components with the x- and y-polarizations, respectively. The fundamental fields in the transmitted and reflected directions from the sample are cut out by the infrared blocks (IR-block). The generated SHG light passes through an analyzer that only transmits s-polarized light (normal to the plane of incidence). The s-polarized SH signal is thus detected as a function of the fundamental beam polarization state controlled with the QWP rotation angle. The SHG signal is detected with a sensitive photomultiplier tube connected to a photon counting system, which is synchronized to the repetition rate of the laser. In addition, a bandpass filter with a center wavelength at the second-harmonic wavelength was used at the aperture of the photon multiplier detector to ensure no stray light from the background. The setup described above is used for the measurements reported in **Publication 1** and **Publication 2**.

The measurement setup used for the characterization of the second-order nonlinear properties of the aerosol-synthesized samples is very similar to the one used for the L-shaped particles except for the fundamental beam which was derived from a Nd:YAG laser producing 70 ps pulses at a 1 kHz repetition rate and with 1064 nm wavelength. The experimental setup is presented in Fig. 4.10. The polarization state for the fundamental beam was con-

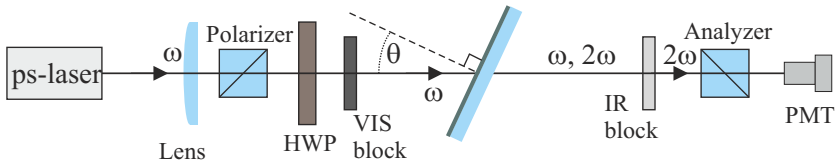

Figure 4.10 Experimental setup for the measurement of second-harmonic generation and Maker-fringes from multilayer samples fabricated with aerosol techniques.

trolled by calcite Glan polarizer and the half-wave plate (HWP) placed right after the polarizer. The fundamental beam was weakly focused on the sample under test with a 25 cm focal-length lens, resulting in a spot size of around 20 μm at the sample plane. The

average power of the beam just before the sample was 34 mW for all the measurements. As for the L-shaped nanoparticles setup, the generated SHG light passes through an s-directed analyzer, such that the s-polarized or p-polarized SH signals are detected as a function of the fundamental beam polarization direction controlled with the HWP rotation angle. The sample was mounted on a high-precision rotation stage to detect the p-polarized SHG as a function of the angle of incidence, therefore recording the Maker-fringe pattern. The SHG signal was found to be a highly directional beam for the aerosol samples, thus verifying the coherent character of the process. SHG radiation was detected with a photomultiplier, with an additional narrow-band interference filter (central wavelength 532 nm, bandwidth 4 nm) placed in front. The experimental setup presented in Fig. 4.10 was used for the experiments presented in **Publication 3**, and **Publication 4**.

4.5 Tensor Analysis of the SHG Signals

In order to analyze the results of the SHG experiments of the L-shaped nanoparticles, we use the nonlinear response tensor formalism described in Chapter 2. Local fields and material properties such as susceptibilities, exhibit strong spatial variations in the scale of a wavelength or less for metal nanostructures and the traditional model of nonlinear response based on the electric-dipole approximation and nonlinear susceptibility is not well suited to describe the responses of such structures. In an earlier implementation of the NRT approach[42], the second-order NRT structure was determined by electric-dipole-type symmetry rules for a given experimental geometry such that the NRT could be considered equivalent to the nonlinear susceptibility tensor in the effective medium limit of the sample. Here, we extended the NRT approach to account for dipole and higher-multipole interactions. Up to lowest-order magnetic-dipole and electric-quadrupole effects, the effective SH source polarization, magnetization, and quadrupolarization are expressed with equations similar to Eqs. (2.13,2.15a,2.15b) in Chapter 2:

$$P_i 2\omega = A^{eee}_{ijk}(2\omega,\omega,\omega)E_j(\omega)E_k(\omega) + A^{eem}_{ijk}E_j(\omega)B_k(\omega) + A^{eeQ}_{ijkl}E_j(\omega)\nabla_k E_l(\omega), \quad (4.1a)$$

$$M_i(\omega) = A^{mee}_{ijk}(2\omega,\omega,\omega)E_j(\omega)E_k(\omega), \quad (4.1b)$$

$$Q_{ij}(2\omega) = A^{Qee}_{ijkl}(2\omega,\omega,\omega)E_k(\omega)E_l(\omega), \quad (4.1c)$$

where indices i, j, and k refer to the Cartesian field components. The effective NRT has now components connected only to electric dipole A^{eee}_{ijk}, magnetic dipole A^{eem}_{ijk}, electric

quadrupole A^{eeQ}_{ijkl}, nonlinear magnetization A^{mee}_{ijk}, and nonlinear quadrupolization A^{Qee}_{ijkl}. In addition, emission from the quadrupolarization involves a gradient of the source with respect to the direction of emission $\nabla_i Q_{ij}$ [47]. From the measurements of the coherent signals, we are unable to separate magnetic-dipole and electric-quadrupole signals [50]. Given the limitation to the spatial symmetry operations, we propose a model in which the electric quadrupole effects are implicitly included in the magnetic tensors $\mathbf{A}^{eem}$ and $\mathbf{A}^{mee}$. With this in mind, we now take $\mathbf{A}^{eeQ} = \mathbf{A}^{Qee} = 0$ in Eqs. (4.1). With the effective medium approximation made, the field components refer to the incident plane waves and not the strongly varying local fields in the nanostructure. The array of nanoparticles in nearly at normal incidence, which limits the fields components to x- and y-directions, and thereby the i, j, and k indices in Eq. (4.1).

Based on the above assumptions, we construct a model for the case of a fundamental plane wave, where the generated SHG field is expressed as:

$$E_x(2\omega) = fE_x^2(\omega) + gE_y^2(\omega) + hE_x(\omega)E_y(\omega), \tag{4.2}$$

where $E_x(2\omega)$ is the x-polarized signal generated from the sample, and $E_x(\omega)$ and $E_y(\omega)$ are the components of the fundamental field polarized along the x- and y-directions, respectively. The expansion coefficients f, g, and h have generally complex values, and they are defined by the formulas:

$$f = A^{eee}_{xxx} \pm A^{eem}_{xxy} \pm A^{mee}_{yxx}, \tag{4.3a}$$

$$g = A^{eee}_{xyy} \mp A^{eem}_{xyx} \pm A^{mee}_{yyy}, \tag{4.3b}$$

$$h = A^{eee}_{xxy} \pm (A^{eem}_{xyy} - A^{eem}_{xxx}) \pm A^{mee}_{yxy}, \tag{4.3c}$$

where the proper signs for each detected configurations (metal side incidence, transmission direction (M-T); metal side, reflection direction (M-R); substrate side, transmission direction (S-T); and substrate side, reflection direction (S-R)) are indicated in Table 4.1.

The measurements were performed for two geometries as shown in Fig. 4.11. The subtle differences in the measured SHG fields for the different experimental geometries, which are caused by the interference between the electric-dipole and higher-order multipolar contributions, give us the information about the magnitude of the higher-order contributions to the total SHG signal. This model is used for the data analysis in **Publication 1** and **Publication 2**.

Table 4.1. NRT element signs with respect to measurement geometry (M-T, metal side, transmission; M-R, metal side, reflection; S-T, substrate side, transmission; S-R, substrate side, reflection). $A_{xyy}^{eem'} = (A_{xyy}^{eem} - A_{xxx}^{eem})$.

Geometry	A_{xxx}^{eee}	A_{xxy}^{eem}	A_{yxx}^{mee}	A_{xyy}^{eee}	A_{xyx}^{eem}	A_{yyy}^{mee}	A_{xxy}^{eee}	$A_{xyy}^{eem'}$	A_{yxy}^{mee}
M-T	+	-	-	+	+	-	-	+	+
M-R	+	-	+	+	+	+	-	+	-
S-T	+	+	+	+	-	+	+	+	+
S-R	+	+	-	+	-	-	+	+	-

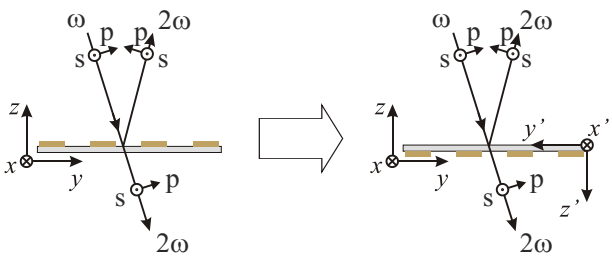

Figure 4.11 The geometry of the conducted measurements: the fundamental beam is first incident on the metal side of the sample, and after flipping over the sample, on the substrate side. The angle of incidence is kept relatively small, which allows us to identify s- and p-polarizations with x- and y-polarizations, respectively. After flipping the sample, the coordinate system connected with the sample is transformed with respect to the laboratory coordinate system according to relations: $x = x'$; $y = -y'$; $z = z'$.

4.6 Tensor Analysis of the Nanocomposites

To analyze the results of the measurements made for the nanocomposite samples, we have developed a theoretical model based on surface SHG as described in Chapter 2, accounting for the propagation effects in the deposited layers (see Fig. 4.12) and transmission of the multiple interfaces. The f, g, and h parameters defined by Eqs.(2.27-2.29) take the form:

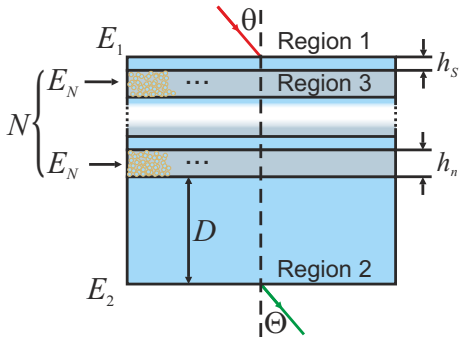

Figure 4.12 Schematic illustration of the nanocomposite samples. D is the thickness of the glass substrate, N is the number of layers, and h_n and h_S represent the thickness of silver-decorated nanoparticles and pure silica, respectively. The SHG sources with effective contribution from a single layer E_k^{al} are indicated.

$$f = t_{p12}^2 T_{p21} \Delta_k^{(p)} \times [\chi_{xxz}^{\text{Ag/glass}} \sin 2\theta_3 \cos\Theta_3 + \chi_{zxx}^{\text{Ag/glass}} \cos^2\theta_3 \sin\Theta_3 + \chi_{zzz}^{\text{Ag/glass}} \sin^2\theta_3 \sin\Theta_3], \quad (4.4)$$

$$g = t_{s12}^2 T_{p21} \Delta_k^{(s)} \chi_{zxx}^{\text{Ag/glass}} \sin\Theta_3, \quad (4.5)$$

$$h = t_{s12} t_{p12} T_{s21} \Delta_k^{(ps)} \chi_{zxx}^{\text{Ag/glass}} \sin\theta_3, \quad (4.6)$$

where $\Delta_k^{(p)}$, $\Delta_k^{(s)}$ and $\Delta_k^{(ps)}$ are the phase factors arising from the propagation of the fundamental, and second-harmonic fields inside the composite structure with a total number of layers N, and are expressed with the sums:

$$\Delta_k^{(p)} = \sum_{k=1}^{N} t_{p23}^{2k} T_{p23}^{(N-k)} T_{p32}^{(N-k+1)} \exp[2i(w_2 k h_S + w_3(k-1)h_n)] \times \exp[i(W_2(D + h_S(N-k)) + W_3(N-k+1)h_n]. \quad (4.7a)$$

$$\Delta_k^{(s)} = \sum_{k=1}^{N} t_{s23}^{2k} T_{p23}^{(N-k)} T_{p32}^{(N-k+1)} \exp\left[2i(w_2 k h_S + w_3(k-1)h_n)\right] \times \exp\left[i(W_2(D + h_S(N-k)) + W_3(N-k+1)h_n\right]. \quad (4.7b)$$

$$\Delta_k^{(ps)} = \sum_{k=1}^{N} t_{s23}^{k} t_{p23}^{k} T_{p23}^{(N-k)} T_{p32}^{(N-k+1)} \exp\left[2i(w_2 k h_S + w_3(k-1)h_n)\right] \times \exp\left[i(W_2(D + h_S(N-k)) + W_3(N-k+1)h_n\right]. \quad (4.7c)$$

The subscripts 1, 2, and 3 refer to air, silica, and nanocomposite layers respectively (see marked areas on the schematic image in Fig. 4.12), $\tilde{\omega} = \omega/c$ is the the reduced frequency, h_S denotes the thickness of the silica layer, h_n is the thickness of the nanocomposite active layers. For convenience, we use the notation defined in previous section, in which the quantities written with lower-case letters will be connected with the fundamental field, and the upper-case letters with the SHG field. Within this notation n_i (N_i) is the refractive index of the i^{th} region at the fundamental (SH) frequency, and θ_i (Θ_i) is the angle of propagation of the fundamental (SH) radiation with respect to the structure normal inside the i^{th} region, with the phase factors defined as: $w_i = \tilde{\omega} n_i \cos\theta_i$ ($W_i = 2\tilde{\omega} N_i \cos\Theta_i$). The Fresnel transmission coefficients t_{pij} and t_{sij} (T_{pij} and T_{sij}) are defined with Eqs. 2.30. We also introduce a model for the amplitude of the p-polarized SHG from aerosol sample, which was measured as a function of the angle of incidence with the fundamental laser beam. Because the different layers of the samples were prepared under identical conditions, the equations are derived with the assumption that each interface is an identical source of nonlinear radiation. The SH intensity generated from the multilayer structure is then given by

$$I_{SHG} = |E_1 + E_2 + E_3|^2 \quad (4.8)$$

The SH fields E_1 and E_2 represent the contributions from the air-silica interface in region 1 and silica-air interface in region 2, respectively, and they are given by

$$E_1 = \frac{J}{W_2} t_{p12}^2 (T_{p23} T_{p32})^N T_{p21} \exp\left[i\left(W_2(D + N h_S) + W_3 N h_n\right)\right] \times \left\{\chi_{xxz}^{\text{glass}} \sin 2\theta_2 \cos\Theta_2 + \sin\Theta_2 [\chi_{zxx}^{\text{glass}} (\cos\theta_2)^2 + \chi_{zzz}^{\text{glass}} (\sin\theta_2)^2]\right\}, \quad (4.9)$$

and

$$E_2 = -\frac{J}{W_2} t_{p12}^2 (t_{p23} t_{p32})^{2N} t_{p21}^2 \exp\left[i2\left(w_2(D + Nh_S) + w_3 N h_n\right)\right] \times \left\{\chi_{xxz}^{\text{glass}} \sin 2\theta_2 \cos\Theta_2 + \sin\Theta_2 [\chi_{zxx}^{\text{glass}} (\cos\theta_2)^2 + \chi_{zzz}^{\text{glass}} (\sin\theta_2)^2]\right\}, \quad (4.10)$$

The total contribution E_3 of the nanocomposite multi-layers (region 3 in Fig. 4.12) to the SH field consists of multiple silica-nanoparticles interfaces which depends on the number of deposited layers N as:

$$E_3 = \sum_{k=1}^{N} E_k^{al}, \quad (4.11)$$

where the contribution E_k^{al} of the k^{th} layer to the total SHG signal is:

$$E_k^{al} = \frac{J}{W_3} t_{p12}^2 t_{p23}^{2k} t_{p32}^{2(k-1)} T_{p23}^{(N-k)} T_{p32}^{(N-k+1)} T_{p21} \times \exp\{i2[w_2 k h_S + w_3 (k-1) h_n]\} \exp\{i[W_2(D + (N-k)h_S) + W_3(N-k+1)h_n]\} \times \left\{\chi_{xxz}^{\text{Ag/glass}} \sin 2\theta_3 \cos\Theta_3 + \sin\Theta_3 [\chi_{zxx}^{\text{Ag/glass}} (\cos\theta_3)^2 + \chi_{zzz}^{\text{Ag/glass}} (\sin\theta_3)^2]\right\}. \quad (4.12)$$

With the introduced model we are able to reproduce the measured data with excellent agreements. The analysis with the model presented here was used in **Publication 4**.

Chapter 5

Results and Discussion

In this chapter, we summarize the main results presented in the **Publications** that are a part of this Thesis. The results are presented in logical order, which is the same as the chronological order of the published material. The chapter also includes the measurements which are not included in publications, but are essential for a full understanding of the thesis.

5.1 Multipolar Analysis

Linear Characterization

The arrays of L-shaped nanoparticles are classified into two categories based on their quality. The high-quality sample (HQ) was prepared nearly eight years later than the low-quality (LQ) one, and improvements in the fabrication method clearly resulted in an overall increase of the sample quality. This difference is clearly visible in Figs. 4.4 and 4.5.

For all the experiments and analysis, the in-plane symmetry axis of the L shape is along the x-axis of the coordinate system, and y is the orthogonal in-plane direction. The extinction spectra of both samples, measured with the setup shown in Fig. 4.8, are compared in Fig. 5.1. The samples are strongly dichroic, with the main plasmon resonances at similar

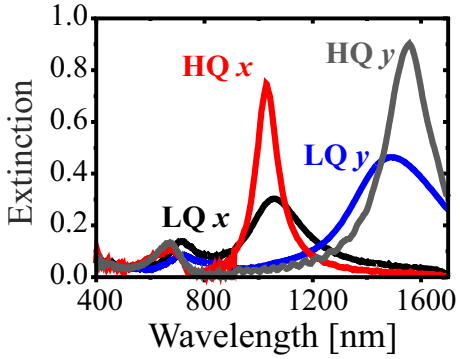

Figure 5.1 Comparison of the extinction spectra measured for low- and high-quality (LQ and HQ, respectively) samples with regular arrays of L-shaped nanoparticles.

wavelengths. The x-polarized resonances occur at 1033 nm $(HQ)_x$ and 1060 nm $(LQ)_x$ and the y-polarized resonances at 1554 nm $(HQ)_y$ and 1490 nm $(LQ)_y$. Additional resonances at 680 nm (HQ) and 710 nm (LQ) are related to the linewidth of the arms[22]. The similar spectral locations of the plasmon resonances in both structures are crucial for the comparison of their second-order nonlinear responses. The main difference between the measured spectra is that, in the low-quality sample, the resulting plasmon resonances are lower in magnitude and much broader. The effect can be easily explained by the inhomogeneous broadening of the plasmon resonance, due to the imperfections of the single particles. Indeed, although the amount of gold used for the fabrication of both samples is comparable, variations in the spatial dimensions of the particles in the low-quality sample induces shifts in the spectral locations of their plasmon resonances, effectively broadening the overall width of the resonances. In the high-quality sample, the effect of inhomogeneous broadening is much smaller, and therefore its resonances are stronger and narrower.

Multipolar analysis

Both samples posses a symmetry plane along the x-axis of the coordinate system, which means that the allowed NRT tensor components for both samples are governed by the same symmetry rules. The x-polarized plasmon resonance nearly matches the fundamental field from the laser used in the SHG experiments in both cases. This ensures that the SHG response is driven similarly by the local-field enhancement for both samples. The detailed NRT tensor element analysis was first performed for the low-quality sample as reported

in **Publication 1**. The results of the analysis were then used as a reference for the measurements conducted with the high-quality sample and the results are presented in **Publication 2**. Previous studies have shown that the samples with low quality can exhibit substantial contributions from the tensor components which are otherwise forbidden by the symmetry rules determined by the particle shape. These "forbidden" sources of SHG were even dominant in some low-quality samples[39–41]. It was postulated that contributions were associated with the imperfections of the nanoparticle samples which give rise to higher-order multipolar nonlinear effects. Using the NRT formalism discussed in chapter 4 that treats the array of particles as an effective medium with contributions from the magnetic dipole and electric quadrupole effects allowed us to verify this hypothesis by comparing the values of the tensor components determined for the low- and high-quality samples. The results of the SHG measurements analysis are summarized in Table 5.1. The quantitative

Table 5.1. NRT elements determined for the low-quality and high-quality samples with arrays of L-shaped nanoparticles. The table consolidates the results presented in **Publication 1** and **Publication 2**. $A_{xyy}^{eem'} = (A_{xyy}^{eem} - A_{xxx}^{eem})$.

Tensor		Low-quality		High-quality	
comp.	Allowed	Value	Magn.	Value	Magn.
A_{xxx}^{eee}	yes	1	1	1	1
A_{xxy}^{eem}	yes	$-0.239 + 0.408i$	0.473	-0.003	0.003
A_{yxx}^{mee}	yes	$0.034 + 0.041i$	0.054	-0.002	0.002
A_{xyy}^{eee}	yes	$0.794 + 0.063i$	0.797	$0.313 - 0.114i$	0.333
A_{xyx}^{eem}	yes	$0.233 - 0.315i$	0.392	$0.009 - 0.015i$	0.018
A_{yyy}^{mee}	yes	$0.012 - 0.033i$	0.035	$-0.007 + 0.013i$	0.015
A_{xxy}^{eee}	no	$0.199 - 0.086i$	0.217	$0.008 - 0.002i$	0.009
$A_{xyy}^{eem'}$	no	$0.438 + 0.137i$	0.459	$-0.035 + 0.003i$	0.035
A_{yxy}^{mee}	no	$0.003 + 0.007i$	0.007	$-0.001 + 0.004i$	0.004

information about the various multipole effects is obtained by fitting the SHG measured as a function of the QWP rotation angle with the model presented in chapter 4, by setting the values of the coefficients f, g, and h of Eqs. (4.2-4.3) to be a free running, complex parameters. The f, g, h parameters obtained for different experimental geometries are next used to determine the components of the NRT by constructing a group of linear equations, whose solution yields the relative complex values of the NRT components connected with electric-dipole or higher-multipolar interactions (see Table 5.1). The values are normalized to the electric-dipole component A_{xxx}^{eee}, which is dominant in both cases. This element is allowed for the ideal structure and is resonant at the fundamental wavelength for both samples. The signature of the interference of higher-multipolar contributions is observed in the radiation patterns for the modulated polarization state of the fundamental field, which

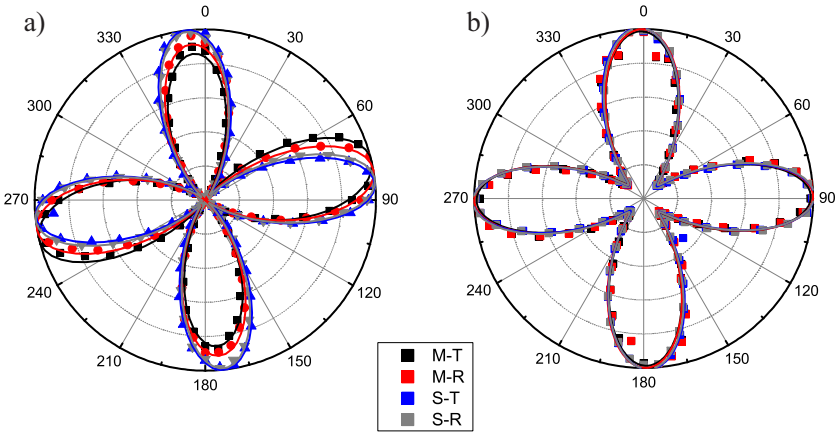

Figure 5.2 SHG measured for different geometries of the experiment reveal the higher-multipolar contributions in the second-harmonic radiation from the L-shaped nanoparticle arrays. a) Low-quality sample with visible differences in SHG measured in different geometries, b) high-quality sample with almost identical line-shapes obtained for measurements in different experimental geometries.

is observed as the difference between the lineshapes measured in different experimental geometries. The results are presented in Fig. 5.2.

The developed multipolar NRT formalism allowed us to determine the contributions from the higher-multipolar effects. We also confirmed the origin of such effects in metal nanostructures. For the high-quality sample, we see that the symmetry rules for second-harmonic generation are well fulfilled and the higher-multipole effects are almost completely suppressed. Moreover, after accounting for the different particle densities of the two samples, the SHG response of the present sample was found to be higher by a factor of 10. This enhancement arises from the narrower resonance and better resonance enhancement at the fundamental wavelength.

For the case of low-quality sample, the higher-multipolar contributions lead to the symmetry-forbidden SHG, whereas in the case of high-quality sample the response is dominated by the symmetry-allowed electric-dipole tensor components. We have thus essentially reached the dipole limit in SHG, implying that the response is dominated by the overall features of the sample, not by random defects. This is a prerequisite for tailoring the nonlinear response in a controllable way by the structural features of the sample.

5.2 Induced Symmetry Breaking in Bulk-like Nanocomposite

Linear Characterization

The extinction spectra measurements for the multilayer silver-decorated nanoparticles-silica composites were performed with a high-sensitivity, high-resolution UV-Vis-NIR spectrophotometer (Shimadzu UV-3600). The results are illustrated in Fig. 5.3 where we can clearly identify the typical plasmon resonance of silver particles centered at around 370 nm. The fact that the resonance linewidth remains constant for a growing number of layers indicates the absence of silver clusters that would otherwise significantly broaden the resonance. We also observe that the magnitude of the extinction maximum grows linearly with the number of layers (see inset in Fig. 5.3) and how the spectral location and width of the plasmon resonance remain unchanged with the number of layers. That shows that the fabrication process is controlled, and allows for the fabrication of structures with high repeatability. The oscillations visible for wavelengths above 600 nm arise from weak Fabry-Perot effects within the active layers. The linear properties of such structures depend only on the over-

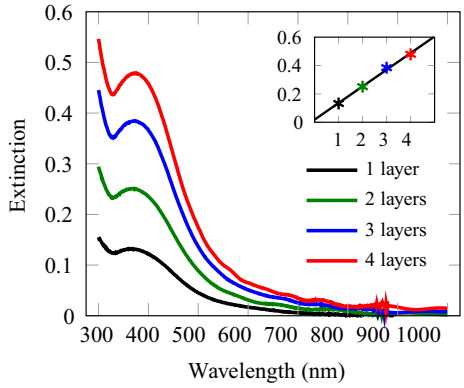

Figure 5.3 Measured extinction spectra for silver-glass nanocomposites samples with different number of layers.

all thickness the nanocomposite, which was verified by the measurements performed for two specially prepared control samples (see Fig. 4.7 (b) and (c)). The results of this measurements shows that the plasmon resonance peak arises from the metal inclusions, and that the layers structure of the sample does not influence its overall extinction (see

Fig. 5.4). Moreover, the extinction spectra are independent of the polarization of incident light, which is not surprizing as the fabricated samples are isotropic in the plane of the sample. The above measurements indicate, that the linear properties of the composites

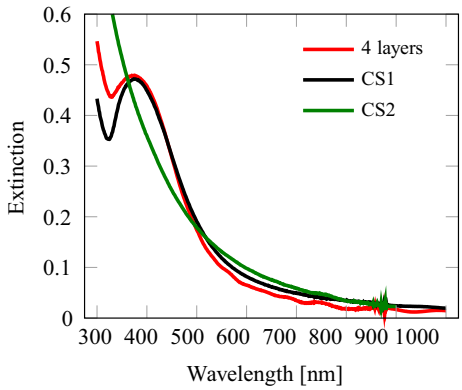

Figure 5.4 Comparison of the extinction spectra of the 4-layer structure with the control samples CS1 (one, thick layer with the thickness equivalent to the sample with four layers), and CS2 (four layer structure with no silver inclusions).

are fully determined by the fabrication conditions that sets the particle size, resulting in highly repeatable structures with almost identical linear properties. With the selected fabrication conditions the only free parameter is the thicknesses of the consecutive layers, which in both cases (nanoparticle deposition, and dielectric coater) are determined by the deposition time.

SHG Experiments

In the case of randomly distributed nanoparticles with a size close to a few nanometers, the second-order nonlinear response can be very well described with an electric dipole type of interaction. The sample isotropy in the plane of incidence is confirmed by the SHG measurements with the HWP rotating the linear input polarization. The result of the measurement, presented in Fig. 5.5, shows that the SHG signal for the p-s and s-s input-output polarization combinations is equal to zero, which implies an isotropic surface-type sample. Characterization of the SHG signal from the control samples CS1 and CS2 allows to identify the source of the nonlinear response. Specifically, the SHG results shown in Fig. 5.6 for these samples show that both metal inclusions and a layered structure are crucial to observe SHG. Indeed, the control sample CS1 that contains a single layer of

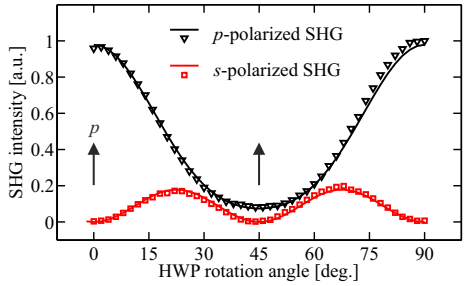

Figure 5.5 Experimentally measured intensity at 532 nm for p- (black dots) and s-polarized (red dots) SHG as a function of the HWP rotation angle modulating the polarization of the incident beam at 1064 nm. The angle of incidence was fixed to 62°. The results are normalized with respect to the p-polarized SHG intensity. Solid lines show the theoretical fit from Eqs. 4.4-4.7.

silver-silica nano-composite with total thickness and linear properties identical compared to the four-layer sample produces a SH signal three-times larger than that from the clean substrate, yet significantly less than measured from the composite with four active layers. This shows that a multilayer arrangement increases the amplitude of the SH response as compared to a single layer of equivalent thickness. On the other hand, sample CS2 which is identical with respect to the four-layer structure (four-layers of nanoparticles separated with silica glass) but does not contain the metal inclusions (and therefore does not exhibit any plasmon resonance) gives a SH signal which is lower that the signal measured from clean substrate. This result illustrates the importance of metal inclusion in observing SHG in the nano-composites.

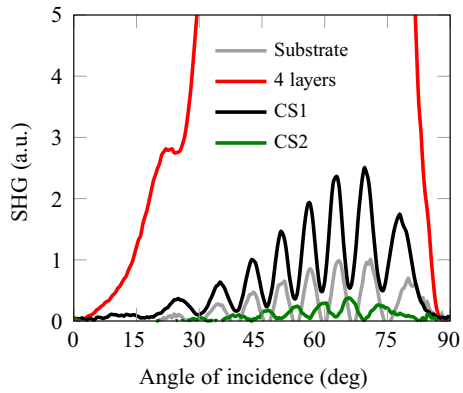

Figure 5.6 Maker-fringes measured for the control samples CS1 and CS2.

With the model described by Eqs. (4.8-4.12) in Chapter 4, we can calculate the absolute

values of the nonlinear surface tensor components in two steps. First, we estimate the thicknesses of the samples from the measured Maker-fringes. Next, we use a least-square algorithm to fit the Maker-fringes with the model. The fitting algorithm uses four free-running parameters: the three independent tensor components, and one scaling factor that accounts for the overall magnitude of the SHG intensity per single active layer. The measurements are normalized with respect to the SHG response of a clean glass plate used as a substrate for all the samples. With the known surface parameters of glass[135], we are able to determine the absolute values of the surface tensor components of the composite material. The resulting fits for the multilayer structures are presented in Fig. 5.7. The extracted tensor values are shown in Table 5.2. We further verified our results by evaluating the f, g, and h values for the four-layer structure from the model presented in Chapter 4, and superimposed the results to the experimental polarization SHG measurements. The solid lines in Fig. 5.5 are the results of calculation with the model, and are in excellent agreement with the data points.

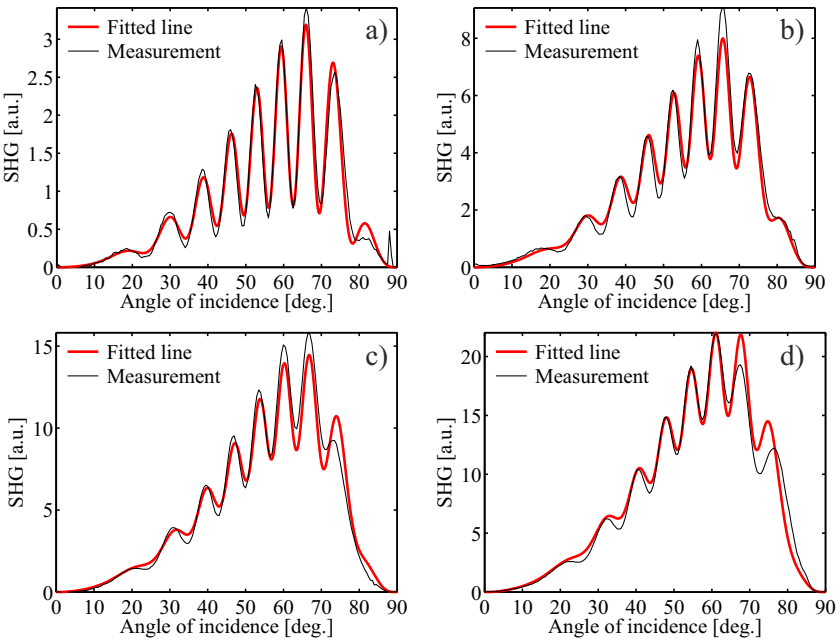

Figure 5.7 Maker-fringe measurements (black solid line) with fitted model (red solid line). The results are normalized with respect to the p-polarized SHG intensity from the clean glass substrate.

The measurement results presented here for all the aerosol samples are the result of averaging of several measurements performed at different spatial locations on the sample. The

Table 5.2. Calculated absolute values for the surface tensor components of a single nanocomposite layer.

Surface tensor components	Absolute Ag/glass composite (10^{-22}m^2/V)	Ag/glass normalized magnitude
χ_{xxz}	23.48	1
χ_{zxx}	15.28	0.65
χ_{zzz}	40.86	1.74

drawback of the aerosol fabrication method is a high porosity and roughness of the sample. The same effect is most likely responsible for the mechanism of the symmetry-breaking; when the number of rough layers increases, the differences between SHG signals measured in different spatial locations can be significant as shown in Fig. 5.8. The differences be-

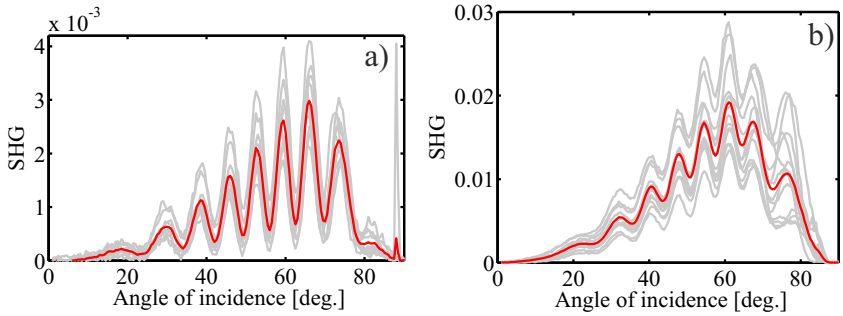

Figure 5.8 Maker-fringe measurements made for different spatial location of incidence beam. a) The average (red line) and SHG measurements (gray lines) for 1-layer sample, b) the average (red line) and SHG measurements for 4-layer sample.

tween measured SHG signals from 4-layer samples are of the order of 80% of the average over all the measurements, which indicates that SHG is strongly dependent on the point of incidence. For a one-layer sample, this effect is not visible, as the porosity of the structure grows with the number of layers. The linear and nonlinear optical properties of samples are reported in **Publication 3**. The results of the detailed tensor analysis are presented in **Publication 4**.

Nevertheless, the aerosol method is still much cheaper and time efficient than the EBL methods. In addition, the fabrication process has not been optimized yet at all. The limitation on structure topology might be overcome by the use of prefabricated substrates with an already imprinted structure, e.g., a diffraction grating. This kind of method would allow for the fabrication of three-dimensional nanostructures resembling plasmonic

photonic crystals, by stacking multiple layers on top of each other. The porosity of the samples might be decreased by using a piezoelectric element which would vibrate the substrate such that the electrostatically attracted particles would be packed tighter. These concepts, however, have yet to be verified in practice.

Chapter 6

Concluding Remarks

The results presented in this thesis show that optical second-harmonic generation is a very useful tool in determining the properties of metal nanostructures. With the help of fairly simple measurement techniques combined with theoretical knowledge, we can obtain information about the origin of the nonlinear response and its character. By applying simple rules, determined by measurement results and consequent analysis, we can extrapolate and fabricate structures with fine-tuned properties which are most suitable for specific applications.

We did verify in this work, that indeed, the imperfections of the structures lead to the presence of higher-multipolar effects in SHG radiation. This brings the conclusion that careful design and optimization of the structure can lead to materials with the desired properties, as long as the fabrication method is precise enough. In other words, it has to be repeatable and very accurate, in order to avoid the effects arising from defects. In the case of regular arrays of planar nanostructures, it would be most interesting to investigate the responses of such structures in and out of plasmon resonance regime, in order to determine the role of the multipole effects under resonant and non-resonant excitation.

The aerosol fabrication techniques helped us to develop interesting structure, which can be further optimized for the nonlinear optics applications. Presented multi-layer nanocomposite is a result of a simple and cheap fabrication technique, and the studies with SHG revealed that the material is interesting as the second-order nonlinear material. Keeping

that in mind, we can now fabricate effectively thick, bulk-like multilayer structure, which would have good second-order nonlinear properties. Since the strong local-field confinement present in plasmonic structures also drives the third-order nonlinearity, it would be most interesting to fabricate structures optimized for both second- and third-order nonlinearity. This, however is a distant goal for now. At the closest range, it is possible to verify the thickness effect of the active nanoparticle layer, which according to preliminary calculations, should benefit the SHG response.

We were trying to achieve significant enhancement in third-order nonlinear response, by introducing the metal inclusions into the dielectric media. Following the effective media theories for the third-order nonlinear refractive index, we were expecting, that for proper concentration of the metal inclusions, the interplay between the absorption and plasmon resonance enhanced third-order effects we could achieve the broadening of the spectrum of a short pulse, and later, after optimization of the structure, even the generation of a supercontinuum. The closest we got were the nanoparticles synthesized with aerosol techniques. However, since the first samples were fabricated as a collection of silver nanoparticles with high concentrations on a glass substrate, as a free-standing structure (not embedded in glass), the nonlinear properties and the durability of the structures were not satisfactory.

To conclude, this is a great journey, in which many scientists all over the world are trying to achieve new kinds of structures with remarkable properties. The application possibilities in optics are virtually unlimited. Together with the developments in fabrication technology, and theoretical models explaining the phenomena, comes understanding and knowledge. With time, thanks to the experience, even more fascinating structures and functionalities will be discovered. Contemporary research in the field of nanoplasmonics is bringing the most exciting concepts to live. Some of these concepts are already becoming reality, nanoplasmonics allows now for the resolving optical microscopy beyond the diffraction limit, as well as manipulate light in truly remarkable ways.

References

[1] M. Zdanowicz, S. Kujala, H. Husu, and M. Kauranen, "Effective medium multipolar tensor analysis of second-harmonic generation from metal nanoparticles," New J. Phys. **13**, 023025 (2011).

[2] R. Czaplicki, M. Zdanowicz, K. Koskinen, J. Laukkanen, M. Kuittinen, and M. Kauranen, "Dipole limit in second-harmonic generation from arrays of gold nanoparticles," Opt. Express **19**, 26866–26871 (2011).

[3] M. Zdanowicz, J. Harra, J. M. Mäkelä, E. Heinonen, T. Ning, M. Kauranen, and G. Genty, "Ordered multilayer silica-metal nanocomposites for second-order nonlinear optics," Appl. Phys. Lett. **103**, 251907 (2013).

[4] M. Zdanowicz, J. Harra, J. M. Mäkelä, E. Heinonen, T. Ning, M. Kauranen, and G. Genty, "Second-harmonic response of multilayer nanocomposites of silver-decorated nanoparticles and silica," Sci. Reports **4**, 5745 (2014).

[5] P. A. Franken, A. E. Hill, C. W. Peters, and G. Weinreich, "Generation of optical harmonics," Phys. Rev. Lett. **7**, 118–119 (1961).

[6] A. L. Schawlow and C. H. Townes, "Infrared and optical masers," Phys. Rev. **112**, 1940–1949 (1958).

[7] J. C. M. Garnett, "Colours in metal glasses and in metallic films," Phil. Trans. R. Soc. Lond. A **203**, 385–420 (1904).

[8] G. Mie, "Beiträge zur optik trüber medien, speziell kolloidaler metallösungen," Ann. Phys. **330**, 377–445 (1908).

[9] J. E. Sipe and R. W. Boyd, "Nonlinear susceptibility of composite optical materials in the maxwell garnett model," Phys. Rev. A **46**, 1614–1629 (1992).

[10] C. F. Bohren and D. R. Huffman, *Absorption and Scattering of Light by Small Particles*, Wiley Science Paperback Series (Wiley, New York, 1998).

[11] S. Link and M. A. El-Sayed, "Spectral properties and relaxation dynamics of surface plasmon electronic oscillations in gold and silver nanodots and nanorods," J. Phys. Chem. B **103**, 8410–8426 (1999).

[12] J. Aizpurua, P. Hanarp, D. S. Sutherland, M. Käll, G. W. Bryant, and F. J. García de Abajo, "Optical properties of gold nanorings," Phys. Rev. Lett. **90**, 057401 (2003).

[13] S. J. Oldenburg, S. L. Westcott, R. D. Averitt, and N. J. Halas, "Surface enhanced raman scattering in the near infrared using metal nanoshell substrates," J. Chem. Phys. **111**, 4729–4735 (1999).

[14] R. D. Averitt, S. L. Westcott, and N. J. Halas, "Linear optical properties of gold nanoshells," J. Opt. Soc. Am. B **16**, 1824–1832 (1999).

[15] C. Rockstuhl, F. Lederer, C. Etrich, T. Zentgraf, J. Kuhl, and H. Giessen, "On the reinterpretation of resonances in split-ring-resonators at normal incidence," Opt. Express **14**, 8827–8836 (2006).

[16] T. Tomioka, S. Kubo, M. Nakagawa, M. Hoga, and T. Tanaka, "Split-ring resonators interacting with a magnetic field at visible frequencies," Appl. Phys. Lett. **103**, 071104 (2013).

[17] J. J. Mock, S. J. Oldenburg, D. R. Smith, D. A. Schultz, and S. Schultz, "Composite plasmon resonant nanowires," Nano Lett. **2**, 465–469 (2002).

[18] J. R. Heath, "Size-dependent surface-plasmon resonances of bare silver particles," Phys. Rev. B **40**, 9982–9985 (1989).

[19] J. Krenn, G. Schider, W. Rechberger, B. Lamprecht, A. Leitner, F. Aussenegg, and J. Weeber, "Design of multipolar plasmon excitations in silver nanoparticles," Appl. Phys. Lett. **77**, 3379–3381 (2000).

[20] N. J. Halas, "Plasmonics: An emerging field fostered by nano letters," Nano Lett. **10**, 3816–3822 (2010).

[21] S. A. Maier, *Plasmonics: Fundamentals and Applications* (Springer, 2008).

[22] H. Husu, J. Mäkitalo, J. Laukkanen, M. Kuittinen, and M. Kauranen, "Particle plasmon resonances in l-shaped gold nanoparticles," Opt. Express **18**, 16601–16606 (2010).

[23] T. Okamoto, I. Yamaguchi, and T. Kobayashi, "Local plasmon sensor with gold colloid monolayers deposited upon glass substrates," Opt. Lett. **25**, 372–374 (2000).

[24] J. J. Mock, D. R. Smith, and S. Schultz, "Local refractive index dependence of plasmon resonance spectra from individual nanoparticles," Nano Lett. **3**, 485–491 (2003).

[25] J. B. Pendry, "Negative refraction makes a perfect lens," Phys. Rev. Lett. **85**, 3966 – 3969 (2000).

[26] A. Holden, "Towards some real applications for negative materials," Phot. Nano. Fund. Appl. **3**, 96–99 (2005).

[27] A. Pors, A. V. Uskov, M. Willatzen, and I. E. Protsenko, "Control of the input efficiency of photons into solar cells with plasmonic nanoparticles," Opt. Commun. **284**, 2226 – 2229 (2011).

[28] S. P. Martin A. Green, "Harnessing plasmonics for solar cells," Nature Phot. **6**, 130–132 (2012).

[29] R. W. Boyd and J. E. Sipe, "Nonlinear optical susceptibilities of layered composite materials," J. Opt. Soc. Am. B **11**, 297–303 (1994).

[30] C. K. Chen, A. R. B. de Castro, and Y. R. Shen, "Surface-enhanced second-harmonic generation," Phys. Rev. Lett. **46**, 145–148 (1981).

[31] H. Tuovinen, M. Kauranen, K. Jefimovs, P. Vahimaa, T. Vallius, J. Turunen, N.-V. Tkachenko, and H. Lemmetyinen, "Linear and second-order nonlinear optical properties of arrays of noncentrosymmetric gold nanoparticles," J. Nonlinear Opt. Phys. Mater. **11**, 421–432 (2002).

[32] S. Kujala, B. K. Canfield, M. Kauranen, Y. Svirko, and J. Turunen, "Multipole interference in the second-harmonic optical radiation from gold nanoparticles," Phys. Rev. Lett. **98**, 167403 (2007).

[33] M. W. Klein, C. Enkrich, M. Wegener, and S. Linden, "Second-harmonic generation from magnetic metamaterials," Science **313**, 502–504 (2006).

[34] F. Niesler, N. Feth, S. Linden, J. Niegemann, J. Gieseler, K. Busch, and M. Wegener, "Second-harmonic generation from split-ring resonators on a gaas substrate," Opt. Lett. **34**, 1997–1999 (2009).

[35] M. Hentschel, T. Utikal, H. Giessen, and M. Lippitz, "Quantitative modeling of the third harmonic emission spectrum of plasmonic nanoantennas," Nano Lett. **12**, 3778–3782 (2012).

[36] G. Xu, M. Tazawa, P. Jin, and S. Nakao, "Surface plasmon resonance of sputtered ag films: substrate and mass thickness dependence," Appl. Phys. A **80**, 1535–1540 (2005).

[37] J. Harra, J. Mkitalo, R. Siikanen, M. Virkki, G. Genty, T. Kobayashi, M. Kauranen, and J. M. Mkel, "Size-controlled aerosol synthesis of silver nanoparticles for plasmonic materials." J. Nanopart. Res. **14**, 870 (2012).

[38] S. Linden, F. B. P. Niesler, J. Förstner, Y. Grynko, T. Meier, and M. Wegener, "Collective effects in second-harmonic generation from split-ring-resonator arrays," Phys. Rev. Lett. **109**, 015502 (2012).

[39] B. Canfield, K. Kujala, K. Jefimovs, J. Turunen, and M. Kauranen, "Linear and nonlinear optical responses influenced by broken symmetry in an array of gold nanoparticles," Opt. Express **12**, 5418–5423 (2004).

[40] B. K. Canfield, S. Kujala, K. Laiho, K. Jefimovs, J. Turunen, and M. Kauranen, "Chirality arising from small defects in gold nanoparticle arrays," Opt. Express **14**, 950–955 (2006).

[41] B. K. Canfield, S. Kujala, K. Jefimovs, T. Vallius, J. Turunen, and M. Kauranen, "Polarization effects in the linear and nonlinear optical responses of gold nanoparticle arrays," J. Opt. A: Pure Appl. Opt. **7**, S110S117 (2005).

[42] S. Kujala, B. Canfield, M. Kauranen, Y. Svirko, and J. Turunen, "Multipolar analysis of second-harmonic radiation from gold nanoparticles," Opt. Express **16**, 17196–17208 (2008).

[43] J. Schwinger, ed., *Selected Papers on Quantum Electrodynamics* (Dover Publications, 1958).

[44] J. C. Maxwell, "A dynamical theory of the electromagnetic field," Phil. Trans. R. Soc. Lond. **155**, 459–512 (1865).

[45] R. Boyd, *Nonlinear Optics* (Academic Press, 2008), 3rd ed.

[46] L. Novotny and B. Hecht, *Principles of Nano-Optics* (Cambridge University Press, 2006).

[47] J. D. Jackson, *Classical Electrodynamics* (John Wiley & Sons, Inc., 1999), 3rd ed.

[48] P. S. Pershan, "Nonlinear optical properties of solids: Energy considerations," Phys. Rev. **130**, 919–929 (1963).

[49] E. Adler, "Nonlinear optical frequency polarization in a dielectric," Phys. Rev. **134**, A728–A733 (1964).

[50] M. Kauranen, T. Verbiest, and A. Persoons, "Second-order nonlinear optical signatures of surface chirality," J. Mod. Opt. **45**, 403–423 (1998).

[51] C. A. Dailey, B. J. Burke, and G. J. Simpson, "The general failure of kleinman symmetry in practical nonlinear optical applications," Chem. Phys. Lett. **390**, 8 – 13 (2004).

[52] G. B. Arfken and H. J. Weber, *Mathematical Methods for Physicists* (Academic Press, 2001), 5th ed.

[53] Y. R. Shen, "Surface properties probed by second-harmonic and sum-frequency generation," Nature **337**, 519–525 (1989).

[54] J. E. Sipe, "New green-function formalism for surface optics," J. Opt. Soc. Am. B **4**, 481–489 (1987).

[55] M. Kauranen and S. Cattaneo, "Chapter 2 polarization techniques for surface nonlinear optics," in "Progress in Optics 51," , vol. 51 of *Progress in Optics*, E. Wolf, ed. (Elsevier, 2008), chap. 2, pp. 69–120.

[56] J. J. Maki, M. Kauranen, and A. Persoons, "Surface second-harmonic generation from chiral materials," Phys. Rev. B **51**, 1425–1434 (1995).

[57] M. Kauranen, T. Verbiest, J. J. Maki, and A. Persoons, "Second-harmonic generation from chiral surfaces," J. Phys. Chem. **101**, 8193–8199 (1994).

[58] M. I. Stockman, D. J. Bergman, C. Anceau, S. Brasselet, and J. Zyss, "Enhanced second-harmonic generation by metal surfaces with nanoscale roughness: Nanoscale dephasing, depolarization, and correlations," Phys. Rev. Lett. **92**, 057402 (2004).

[59] K. Li, M. I. Stockman, and D. J. Bergman, "Enhanced second harmonic generation in a self-similar chain of metal nanospheres," Phys. Rev. B **72**, 153401 (2005).

[60] B. K. Canfield, S. Kujala, K. Jefimovs, Y. Svirko, J. Turunen, and M. Kauranen, "A macroscopic formalism to describe the second-order nonlinear optical response of nanostructures," J. Opt. A: Pure Appl. Opt. **8**, S278 (2006).

[61] P. B. Johnson and R. W. Christy, "Optical constants of the noble metals," Phys. Rev. B **6**, 4370–4379 (1972).

[62] H. Raether, *Surface Plasmons on Smooth and Rough Surfaces and on Gratings* (Springer, Berlin, 1988).

[63] U. Kreibig and M. Vollmer, *Optical Properties of Metal Clusters*, Springer Series in Materials

Science (Springer, Berlin, 1995).

[64] D. A. G. Bruggeman, "Berechnung verschiedener physikalischer konstanten von heterogenen substanzen. i. dielektrizitätskonstanten und leitfähigkeiten der mischkörper aus isotropen substanzen," Ann. Phys. **416**, 636–664 (1935).

[65] O. Levy and D. Stroud, "Maxwell garnett theory for mixtures of anisotropic inclusions: Application to conducting polymers," Phys. Rev. B **56**, 8035–8046 (1997).

[66] L. Novotny, "Effective wavelength scaling for optical antennas," Phys. Rev. Lett. **98**, 266802 (2007).

[67] V. M. Shalaev, "Optical negative-index metamaterials," Nature Phot. **1**, 41–48 (2007).

[68] U. Leonhardt, "Optical conformal mapping," Science **312**, 1777–1780 (2006).

[69] H. Gao, B. Zhang, and G. Barbastathis, "Photonic cloak made of subwavelength dielectric elliptical rod arrays," Opt. Commun. **284**, 4820 – 4823 (2011).

[70] D. Rainwater, A. Kerkhoff, K. Melin, J. C. Soric, G. Moreno, and A. Alú, "Experimental verification of three-dimensional plasmonic cloaking in free-space," New J. Phys. **14**, 013054 (2012).

[71] H. Husu, R. Siikanen, J. Mäkitalo, J. Lehtolahti, J. Laukkanen, M. Kuittinen, and M. Kauranen, "Metamaterials with tailored nonlinear optical response," Nano Lett. **12**, 673–677 (2012).

[72] V. M. Shalaev, W. Cai, U. K. Chettiar, H.-K. Yuan, A. K. Sarychev, V. P. Drachev, and A. V. Kildishev, "Negative index of refraction in optical metamaterials," Opt. Lett. **30**, 3356–3358 (2005).

[73] C. Enkrich, M. Wegener, S. Linden, S. Burger, L. Zschiedrich, F. Schmidt, J. F. Zhou, T. Koschny, and C. M. Soukoulis, "Magnetic metamaterials at telecommunication and visible frequencies," Phys. Rev. Lett. **95**, 203901 (2005).

[74] T. Pakizeh, M. S. Abrishamian, N. Granpayeh, A. Dmitriev, and M. Käll, "Magnetic-field enhancement in gold nanosandwiches," Opt. Express **14**, 8240–8246 (2006).

[75] M. W. Klein, M. Wegener, N. Feth, and S. Linden, "Experiments on second- and third-harmonic generation from magnetic metamaterials," Opt. Express **15**, 5238–5247 (2007).

[76] E. U. Condon, "Theories of optical rotatory power," Rev. Mod. Phys. **9**, 432–457 (1937).

[77] J. Zhou, L. Zhang, G. Tuttle, T. Koschny, and C. M. Soukoulis, "Negative index materials using simple short wire pairs," Phys. Rev. B **73**, 041101(R) (2006).

[78] S. Zhang, W. Fan, N. C. Panoiu, K. J. Malloy, R. M. Osgood, and S. R. J. Brueck, "Experimental demonstration of near-infrared negative-index metamaterials," Phys. Rev. Lett. **95**, 137404 (2005).

[79] H. Schweizer, L. Fu, H. Gräbeldinger, H. Guo, N. Liu, S. Kaiser, and H. Giessen, "Negative permeability around 630 nm in nanofabricated vertical meander metamaterials," Phys. Status Solidi A **204**, 3886–3900 (2007).

[80] G. Dolling, M. Wegener, C. M. Soukoulis, and S. Linden, "Negative-index metamaterial at

780 nm wavelength," Opt. Lett. **32**, 53–55 (2007).

[81] H. J. Lezec, J. A. Dionne, and H. A. Atwater, "Negative refraction at visible frequencies," Science **316**, 430 – 432 (2007).

[82] J. Valentine, S. Zhang, T. Zentgraf, E. Ulin-Avila, D. A. Genov, G. Bartal, and X. Zhang, "Three-dimensional optical metamaterial with a negative refractive index," Nature **455**, 376–379 (2008).

[83] M. Fleischmann, P. J. Hendra, and A. J. McQuillan, "Raman spectra of pyridine adsorbed at a silver electrode," Chem. Phys. Lett. **26**, 163 (1974).

[84] S. Rao, M. J. Huttunen, J. M. Kontio, J. Makitalo, M.-R. Viljanen, J. Simonen, M. Kauranen, and D. Petrov, "Tip-enhanced raman scattering from bridged nanocones," Opt. Express **18**, 23790–23795 (2010).

[85] K. Kneipp, Y. Wang, H. Kneipp, L. T. Perelman, I. Itzkan, R. R. Dasari, and M. S. Feld, "Single molecule detection using surface-enhanced raman scattering (sers)," Phys. Rev. Lett. **78**, 1667–1670 (1997).

[86] T. W. Ebbesen, H. J. Lezec, H. F. Ghaemi, T. Thio, and P. A. Wolff, "Extraordinary optical transmission through sub-wavelength hole arrays," Nature **391**, 667–669 (1998).

[87] H. F. Ghaemi, T. Thio, D. E. Grupp, T. W. Ebbesen, and H. J. Lezec, "Surface plasmons enhance optical transmission through subwavelength holes," Phys. Rev. B **58**, 6779–6782 (1998).

[88] D. E. Grupp, H. J. Lezec, T. W. Ebbesen, K. M. Pellerin, and T. Thio, "Crucial role of metal surface in enhanced transmission through subwavelength apertures," Appl. Phys. Lett. **77**, 1569–1571 (2000).

[89] Q. Cao and P. Lalanne, "Negative role of surface plasmons in the transmission of metallic gratings with very narrow slits," Phys. Rev. Lett. **88**, 057403 (2002).

[90] J. Wenger, D. Gérard, J. Dintinger, O. Mahboub, N. Bonod, E. Popov, T. W. Ebbesen, and H. Rigneault, "Emission and excitation contributions to enhanced single molecule fluorescence by gold nanometric apertures," Opt. Express **16**, 3008–3020 (2008).

[91] H. Aouani, O. Mahboub, N. Bonod, E. Devaux, E. Popov, H. Rigneault, T. W. Ebbesen, and J. Wenger, "Bright unidirectional fluorescence emission of molecules in a nanoaperture with plasmonic corrugations," Nano Lett. **11**, 637–644 (2011).

[92] T. Xu, X. Jiao, G.-P. Zhang, and S. Blair, "Second-harmonic emission from sub-wavelength apertures: Effects of aperture symmetry and lattice arrangement," Opt. Express **15**, 13894–13906 (2007).

[93] N. Feth, S. Linden, M. Klein, M. Decker, F. Niesler, Y. Zeng, W. Hoyer, J. Liu, S. Koch, J. Moloney, and M. Wegener, "Second-harmonic generation from complementary split-ring resonators," Opt. Lett. **33**, 1975–1977 (2008).

[94] P. Muhlschlegel, H.-J. Eisler, O. J. F. Martin, B. Hecht, and D. W. Pohl, "Resonant optical antennas," Science **308**, 1607–1609 (2005).

[95] H. Fischer and O. J. F. Martin, "Engineering the optical response of plasmonic nanoanten-

nas," Opt. Express **16**, 9144–9154 (2008).

[96] P. Nordlander, C. Oubre, E. Prodan, K. Li, and M. I. Stockman, "Plasmon hybridization in nanoparticle dimers," Nano Lett. **4**, 899–903 (2004).

[97] D. Fromm, A. Sundaramurthy, P. Schuck, G. Kino, and W. Moerner, "Gap-dependent optical coupling of single "bowtie" nanoantennas resonant in the visible," Nano Lett. **4**, 957–961 (2004).

[98] P. J. Schuck, D. P. Fromm, A. Sundaramurthy, G. S. Kino, and W. E. Moerner, "Improving the mismatch between light and nanoscale objects with gold bowtie nanoantennas," Phys. Rev. Lett. **94**, 017402 (2005).

[99] K. Li, M. I. Stockman, and D. J. Bergman, "Self-similar chain of metal nanospheres as an efficient nanolens," Phys. Rev. Lett. **91**, 227402 (2003).

[100] J. Dai, F. Cajko, I. Tsukerman, and M. I. Stockman, "Electrodynamic effects in plasmonic nanolenses," Phys. Rev. B **77**, 115419 (2008).

[101] J. Kneipp, X. Li, M. Sherwood, U. Panne, H. Kneipp, M. I. Stockman, and K. Kneipp, "Gold nanolenses generated by laser ablation-efficient enhancing structure for surface enhanced raman scattering analytics and sensing," Anal. Chem. **80**, 4247 (2008).

[102] S. J. Oldenburg, G. D. Hale, J. B. Jackson, and N. J. Halas, "Light scattering from dipole and quadrupole nanoshell antennas," Appl. Phys. Lett. **75**, 1063 (1999).

[103] T. Pakizeh and M. Käll, "Unidirectional ultracompact optical nanoantennas," Nano Lett. **9**, 2343–2349 (2009). PMID: 19422191.

[104] H. F. Hofmann, T. Kosako, and Y. Kadoya, "Design parameters for a nano-optical yagi-uda antenna," New J. Phys. **9**, 217 (2007).

[105] D. Dregely, J. Taubert, R. Dorfmüller, R. Vogelgesang, K. Kern, and H. Giessen, "3d optical yagi-uda nanoantenna array," Nature Comm. **2**, 267 (2011).

[106] A. Hartschuh, "Tip-enhanced near-field optical microscopy," Angew. Chem. Int. Ed. **47**, 8178 – 8191 (2008).

[107] J. M. Kontio, H. Husu, J. Simonen, M. J. Huttunen, J. Tommila, M. Pessa, and M. Kauranen, "Nanoimprint fabrication of gold nanocones with 10 nm tips for enhanced optical interactions," Opt. Lett. **34**, 1979–1981 (2009).

[108] J. Homola, S. S. Yeea, and G. Gauglitzb, "Surface plasmon resonance sensors: review," Sensor. Actuat. B-Chem. **54**, 3–15 (1999).

[109] K. Johansen, H. Arwin, I. Lundstrom, and B. Liedberg, "Imaging surface plasmon resonance sensor based on multiple wavelengths: Sensitivity considerations," Rev. Sci. Instrum. **71**, 3530–3538 (2000).

[110] S. Enoch, R. Quidant, and G. Badenes, "Optical sensing based on plasmon coupling in nanoparticle arrays," Opt. Express **12**, 3422–3427 (2004).

[111] G. T. Boyd, T. Rasing, J. R. R. Leite, and Y. R. Shen, "Local-field enhancement on rough surfaces of metals, semimetals, and semiconductors with the use of optical second-harmonic

generation," Phys. Rev. B **30**, 519–526 (1984).

[112] V. M. Shalaev and A. K. Sarychev, "Nonlinear optics of random metal-dielectric films," Phys. Rev. B **57**, 13265 (1998).

[113] M. I. Stockman, S. V. Faleev, and D. J. Bergman, "Coherent control of femtosecond energy localization in nanosystems," Phys. Rev. Lett. **88**, 067402 (2002).

[114] S. I. Bozhevolnyi, J. Beermann, and V. Coello, "Direct observation of localized second-harmonic enhancement in random metal nanostructures," Physical Review Letters **90**, 197403 (2003).

[115] S. Takahashi and A. V. Zayats, "Near-field second-harmonic generation at a metal tip apex," Appl. Phys. Lett. **80**, 3479 (2002).

[116] A. Bouhelier, M. Beversluis, A. Hartschuh, and L. Novotny, "Near-field second-harmonic generation induced by local field enhancement," Phys. Rev. Lett. **90**, 013903–013907 (2003).

[117] B. Lamprecht, A. Leitner, and F. Aussenegg, "Femtosecond decay-time measurement of electron-plasma oscillation in nanolithographically designed silver particles," Appl. Phys. B **64**, 269 (1997).

[118] R. Czaplicki, H. Husu, R. Siikanen, J. Mäkitalo, M. Kauranen, J. Laukkanen, J. Lehtolahti, and M. Kuittinen, "Enhancement of second-harmonic generation from metal nanoparticles by passive elements," Phys. Rev. Lett. **110**, 093902 (2013).

[119] B. Canfield, H. Husu, J. Laukkanen, B. Bai, M. Kuittinen, J. Turunen, and M. Kauranen, "Local field asymmetry drives second-harmonic generation in noncentrosymmetric nanodimers," Nano Lett. **7**, 1251–1255 (2007).

[120] H. Husu, B. Canfield, J. Laukkanen, B. Bai, M. Kuittinen, J. Turunen, and M. Kauranen, "Local-field effects in the nonlinear optical response of metamaterials," Metamaterials **2**, 155–168 (2008). Metamaterials'2007 Congress.

[121] M. Danckwerts and L. Novotny, "Optical frequency mixing at coupled gold nanoparticles," Phys. Rev. Lett. **98**, 026104 (2007).

[122] S. Palomba and L. Novotny, "Nonlinear excitation of surface plasmon polaritons by four-wave mixing," Phys. Rev. Lett. **101**, 056802 (2008).

[123] T. Tsang, "Surface-plasmon-enhanced third-harmonic generation in thin silver films," Opt. Lett. **21**, 245–247 (1996).

[124] A. V. Andreev, A. A. Korneev, L. S. Mukina, M. M. Nazarov, I. R. Prudnikov, and A. P. Shkurinov, "Simultaneous generation of second and third optical harmonics on a metal grating," Phys. Rev. B **74**, 235421 (2006).

[125] B. K. Canfield, H. Husu, J. Kontio, J. Viheril, T. Rytknen, T. Niemi, E. Chandler, A. Hrin, J. A. Squier, and M. Kauranen, "Inhomogeneities in the nonlinear tensorial responses of arrays of gold nanodots," New J. Phys. **10**, 013001 (2008).

[126] H. Suchowski, K. OBrien, Z. J. Wong, A. Salandrino, X. Yin, and X. Zhang, "Phase mismatchfree nonlinear propagation in optical zero-index materials," Science **342**, 1223–

1226 (2013).

[127] M. Kauranen, "Freeing nonlinear optics from phase matching," Science **342**, 1182–1183 (2013).

[128] A. Grigorescu, M. van der Krogt, C. Hagen, and P. Kruit, "10 nm lines and spaces written in hsq, using electron beam lithography," Microelectron. Eng. **84**, 822 – 824 (2007). Proceedings of the 32nd International Conference on Micro- and Nano-Engineering.

[129] V. R. Manfrinato, L. Zhang, D. Su, H. Duan, R. G. Hobbs, E. A. Stach, and K. K. Berggren, "Resolution limits of electron-beam lithography toward the atomic scale," Nano Lett. **13**, 1555–1558 (2013).

[130] A. L. Stepanov, "Nonlinear optical properties of implanted metal nanoparticles in various transparent matrixes: a review," Rev. Adv. Mater. Sci. **27**, 115–145 (2011).

[131] T. Donnelly, B. Doggett, and J. G. Lunney, "Pulsed laser deposition of nanostructured ag films," Appl. Surf. Sci. **252**, 4445 – 4448 (2006).

[132] L. M. Liz-Marzän, "Nanometals: Formation and color," Mater. Today **7**, 26 – 31 (2004).

[133] P. West, S. Ishii, G. Naik, N. Emani, V. Shalaev, and A. Boltasseva, "Searching for better plasmonic materials," Laser Photon. Rev. **4**, 795–808 (2010).

[134] A. Pinchuk, G. von Plessen, and U. Kreibig, "Influence of interband electronic transitions on the optical absorption in metallic nanoparticles," J. Phys. D: Appl. Phys. **37**, 3133 (2004).

[135] F. J. Rodriguez, F. X. Wang, and M. Kauranen, "Calibration of the second-order nonlinear optical susceptibility of surface and bulk of glass," Opt. Express **16**, 8704–8710 (2008).

Appendices

Paper 1

Mariusz Zdanowicz, Sami Kujala, Hannu Husu, and Martti Kauranen.

Effective medium multipolar tensor analysis of second-harmonic generation from metal nanoparticles.

New Journal of Physics **13**, 023025 (2011)

New Journal of Physics
The open-access journal for physics

Effective medium multipolar tensor analysis of second-harmonic generation from metal nanoparticles

Mariusz Zdanowicz[1,2,4], **Sami Kujala**[1,3], **Hannu Husu**[1] **and Martti Kauranen**[1]

[1] Department of Physics, Optics Laboratory, Tampere University of Technology, PO Box 692, FI-33101 Tampere, Finland
[2] Department of Transmission and Optical Technology, National Institute of Telecommunications, Szachowa Str. 1, 04-894 Warsaw, Poland
E-mail: mariusz.zdanowicz@tut.fi

New Journal of Physics **13** (2011) 023025 (12pp)
Received 6 September 2010
Published 10 February 2011
Online at http://www.njp.org/
doi:10.1088/1367-2630/13/2/023025

Abstract. We present a detailed multipolar tensor analysis of second-harmonic (SH) generation from arrays of L-shaped gold nanoparticles. We define three effective nonlinear tensors, which include electric dipoles only (A^{eee}) and lowest-order magnetic (and quadrupole) effects at the fundamental (A^{eem}) and the SH (A^{mee}) frequency. The components of the various tensors are distinguished through their different transformations as the experimental geometry is varied. The response is dominated by electric-dipole effects. However, the higher multipoles also play a significant role and are more important at the fundamental frequency than at the SH frequency. The results correlate well with the particles' plasmonic resonances and symmetry rules.

[3] Current address: Department of Micro and Nanosciences, Aalto University School of Science and Technology, PO Box 13500, FI-00076 Aalto, Finland
[4] Author to whom any correspondence should be addressed.

Contents

1. Introduction

The optical properties of metal nanostructures are dominated by the collective oscillations of conduction electrons, giving rise to plasmon resonances [1]. These resonances depend on the particle size and shape as well as their number and mutual ordering when they are organized in arrays. The resonances can lead to strong enhancement of the local electromagnetic fields within the structure [2]–[6]. Such strong local fields may enhance the optical responses of the structure, especially the nonlinear ones, which scale with the high power of the local field.

The local material properties and electromagnetic fields in nanostructures thus exhibit strong nanoscale variations. Such gradients may be favorable for higher-multipole interactions [7], thereby making magnetic dipoles, electric quadrupoles, etc important in the optical responses. The standard electric-dipole approximation may thus not be sufficient to describe the optical responses of nanostructures. In fact, two different types of multipoles should be taken into account [8]–[10]: those corresponding to microscopic multipole moments, arising from the atomic-scale light–matter interaction Hamiltonian [11], and those related to Mie scattering theory [1, 12], where the atomic-scale interaction may be of the electric-dipole origin, and the multipole effects arise from field retardation effects over the nanostructure. However, the radiation patterns of both types are similar in the far field. Moreover, there are particular challenges regarding the understanding of the role of different multipolar interactions in the nonlinear optical responses of various types of samples [13]–[16].

A number of works have addressed the role multipole effects in the optical responses of various kinds of nanoparticles [17]–[20]. Krenn *et al* [21] provided experimental evidence of multipolar plasmon resonances from elongated silver nanoparticles, where resonances depend on the nanoparticle length. The magnetic resonances are thought to play an important role in the properties of metamaterials [22]; however, the role of electric quadrupole effects has also recently been emphasized [23]. The nonlinear properties of nanoparticles as well as the multipolar contributions to the nonlinear properties are a subject of increasing interest [8]–[10], [24]–[27]. Second-harmonic generation (SHG) from arrays of split-ring resonators (SRRs) was studied by Klein *et al* [22]. They found that SHG was the most efficient when the magnetic resonance of the structure was excited. In addition, Petschulat *et al* [28] present a new analytical approach to the nonlinear properties of SRRs). They use a self-consistent model that describes the linear response of meta-atom geometries by their intrinsic plasmonic eigenmodes and includes multipolar effects. The simulated results were then used to estimate the nonlinear interactions that include the expected enhanced SH signal due to both electric and magnetic resonances. In addition, dipolar and quadrupolar effects have been shown

to play an important role in incoherent second-harmonic (SH) scattering from nanoparticles, both in ensemble [11, 27, 29] and single-particle measurements [8].

We have recently provided evidence of significant multipole interference in coherent SH emission from arrays of gold nanoparticles. Our approach [30, 31] was based on the differences between the fundamental radiative properties of electric dipoles as opposed to magnetic dipoles and electric quadrupoles [32]. The higher multipoles were estimated to contribute up to 20% of the total emitted SH field amplitude. Moreover, the tensor components forbidden for the ideal symmetry of the particles were found to play an important role in the SH response of the system [31]. This fact was explained by the chiral symmetry breaking of the particles, giving rise to the dipolar and effective quadrupolar sources that would be forbidden for the case of ideal particles. In this interpretation, the role of surface defects is particularly important, because they can act as local sources of SHG with retardation between the sources giving rise to effective quadrupoles. However, the measurement technique used is only able to provide evidence of higher-multipole interactions at the SH frequency.

In this paper, we extend our experimental approach further by defining effective nonlinear tensors for the nanostructure that include electric and magnetic effects at the fundamental and SH frequencies. Our magnetic tensors also account for the electric quadrupoles, because on the basis of present knowledge, the two types of effects cannot be separated from each other in the measured coherent SHG signals [33]. By relying on the different transformation properties of the nonlinear tensors as the experimental geometry is varied, we provide evidence of higher-multipole interactions at both the fundamental and the SH frequency. In particular, we find that for the structures investigated, the higher multipole effects are even stronger at the fundamental frequency than at the SH frequency.

2. Theoretical basis

The traditional model of the nonlinear response based on the electric-dipole approximation and the nonlinear susceptibility is not well suited to describing the nonlinear responses from metal nanostructures. This is because the local fields and material properties, such as the susceptibility, exhibit strong spatial variations in the scale of a wavelength or less. A full description of such effects is computationally extremely demanding and has been done only for some simple model cases [8, 9, 12, 34]. To avoid such nanoscale difficulties, we have introduced a macroscopic nonlinear response tensor (NRT) approach, in which the sample is treated as a 'black box', and the interesting quantities are the input and output radiation fields [35]. In our earlier implementation of this approach, the structure of the NRT was determined by electric-dipole-type symmetry rules for a given experimental situation at a time. With this limitation in mind, the NRT can also be considered as equivalent to the nonlinear susceptibility tensor in the effective medium limit of the sample.

In this paper, we extend the NRT approach to account for dipole and higher-multipole interactions. Up to lowest-order magnetic-dipole and electric-quadrupole effects, the effective SH source polarization, magnetization and quadrupolarization are [33, 36]

$$P_i(2\omega) = A^{eee}_{ijk}(2\omega, \omega, \omega)E_j(\omega)E_k(\omega) + A^{eem}_{ijk}E_j(\omega)B_k(\omega) + A^{eeQ}_{ijkl}E_j(\omega)\nabla_k E_l(\omega), \quad (1)$$

$$M_i(2\omega) = A^{mee}_{ijk}(2\omega, \omega, \omega)E_j(\omega)E_k(\omega), \quad (2)$$

$$Q_{ij}(2\omega) = A^{Qee}_{ijkl}(2\omega, \omega, \omega)E_k(\omega)E_l(\omega), \quad (3)$$

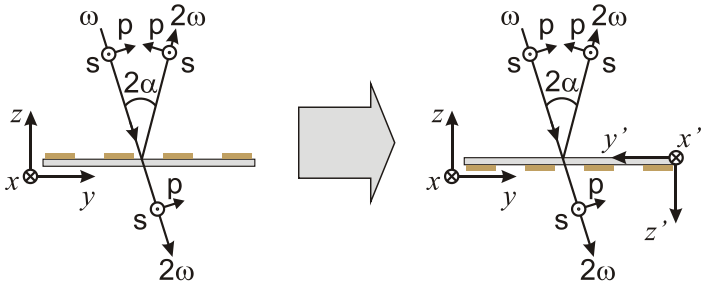

Figure 1. The geometry of the measurements: the fundamental beam is first incident on the metal side of the sample and after flipping the sample over on the substrate side. The angle of incidence α is kept relatively small ($<1^\circ$), which allows us to identify s- and p-polarizations with x- and y-polarizations, respectively. After flipping the sample, the coordinate system connected with the sample is transformed with respect to the laboratory coordinate system with $x = x'$; $y = -y'$; $z = z'$.

respectively, and the indices i, j and k refer to Cartesian field components. In addition, emission from the quadrupolarization involves a gradient of the source with respect to the direction of emission $\nabla_i Q_{ij}$ [32].

The present understanding, however, is that magnetic-dipole and electric-quadrupole effects cannot be separated from each other when coherent and directional signals are detected [33]. At first sight, this may appear surprising, because electric and magnetic interactions differ from each other with regard to time-reversal symmetry [32]. However, it is an open question as to how time reversal should be applied to a nonlinear frequency conversion process. This could be approached by considering the reciprocity of the experiment. To do this, another experiment should be performed, where all frequency components, including the ones generated by the sample, are sent back to the sample in reversed order and with proper phase, amplitude and spatial mode, which is clearly beyond experimental capabilities. Just repeating the SHG experiment with front- and back-side incidence is thus not sufficient.

We are thus experimentally limited to spatial symmetry operations. In the effective medium limit, the gradients associated with the quadrupole tensors $\mathbf{A}^{eeQ}$ and $\mathbf{A}^{Qee}$ are related to field propagation, whereas the field components can only involve transverse components. By considering the available spatial symmetry operations, one finds that the quadrupole effects cannot be separated from magnetic effects, as explained in more detail in [33]. From now on, we thus take $\mathbf{A}^{eeQ} = 0$ and $\mathbf{A}^{Qee} = 0$ in equations (1)–(3), with the understanding that the quadrupole effects are implicitly included in the magnetic tensors $\mathbf{A}^{eem}$ and $\mathbf{A}^{mee}$.

We next apply this formalism to the simplest possible geometry, where the incident laser beam is a plane wave propagating along the positive z-direction and is applied at normal incidence on the sample (figure 1).

It is important to note that under the effective-medium assumption, the field components refer to the incident plane waves, not the strongly varying local fields in the nanostructure. The fields thus only have the x- and y-components, also limiting the indices i, j and k in equations (1) and (2) to these values.

The incident plane wave at the fundamental frequency is thus described by

$$\mathbf{E}(\omega) = [\hat{x}E_x(\omega) + \hat{y}E_y(\omega)]\exp[\mathrm{i}(\mathbf{k}_\omega \cdot \mathbf{r} - \omega t)], \tag{4}$$

where $E_x(\omega)$ and $E_y(\omega)$ are the two polarization components of the beam and the wave vector $\mathbf{k}_\omega = (\omega/c)\hat{\mathbf{z}}$. From Maxwell's equations, it follows that $\mathrm{i}\mathbf{k}_\omega \times \mathbf{E}(\omega) = \mathrm{i}\omega\mathbf{B}(\omega)$, so that the magnetic and electric field components are related by

$$\begin{pmatrix} B_x(\omega) \\ B_y(\omega) \end{pmatrix} \sim \frac{1}{c}\begin{pmatrix} -E_y(\omega) \\ E_x(\omega) \end{pmatrix}. \tag{5}$$

Once the nonlinear sources have been established, they radiate SHG light according to the emission rules of the electric and magnetic dipole sources [29, 30]. For coherent signals emitted along the sample normal to the reflected and transmitted directions, the SHG signals in the far field are proportional to

$$\mathbf{E}(2\omega) \sim \mathbf{P}(2\omega) + \mathbf{k}_{2\omega} \times \mathbf{M}(2\omega), \tag{6}$$

where $\mathbf{k}_{2\omega}$ is the direction of observation ($\mathbf{k}_{2\omega} = (2\omega/c)\hat{\mathbf{z}}$ for transmission or $\mathbf{k}_{2\omega} = -(2\omega/c)\hat{\mathbf{z}}$ for reflection).

To understand how the various tensors contribute to possible measured signals, we consider, as an example, the x-polarized SH signal arising from the x-polarized fundamental beam. Within the electric-dipole approximation, the interaction is thus described by the tensor component A^{eee}_{xxx}. We also take the basic geometry to have the fundamental beam incident on the metal side of the sample, which is described by

$$E_x(2\omega) \sim A^{eee}_{xxx} E_x^2(\omega). \tag{7}$$

In the presence of magnetic contributions at the fundamental and SH frequencies, however, this signal is modified by the tensor components A^{eem}_{xxy} and A^{mee}_{yxx}, respectively. By taking these interactions into account and using equations (5) and (6), we find that the transmitted and reflected SH signals, respectively, are of the form

$$E_x(2\omega) \sim \left(A^{eee}_{xxx} + A^{eem}_{xxy} + A^{mee}_{yxx}\right) E_x^2(\omega), \tag{8}$$

$$E_x(2\omega) \sim \left(A^{eee}_{xxx} + A^{eem}_{xxy} - A^{mee}_{yxx}\right) E_x^2(\omega). \tag{9}$$

Note that compared to the basic definitions of equations (1) and (2), all tensors have now been renormalized in a way that all contributions refer to the electric fields at the fundamental and SH frequencies.

The expressions given by equations (8) and (9), however, do not contain sufficient information to determine all the components of the three tensors. Additional information can be obtained by flipping the sample over from metal-side incidence of the fundamental beam to substrate-side incidence. By rotating the sample by 180° about the x-axis (figure 1), and by recalling that under rotations electric and magnetic quantities transform in the same way, any tensor component with odd number of y indices changes sign. For the new geometry, the transmitted and reflected SH signals are thus

$$E_x(2\omega) \sim \left(A^{eee}_{xxx} - A^{eem}_{xxy} - A^{mee}_{yxx}\right) E_x^2(\omega), \tag{10}$$

$$E_x(2\omega) \sim \left(A^{eee}_{xxx} - A^{eem}_{xxy} + A^{mee}_{yxx}\right) E_x^2(\omega). \tag{11}$$

In our experiments, we modulate the polarization of the fundamental beam. We hence have to consider in the same way the electric-dipole tensor components A^{eee}_{xyy} and $A^{eee}_{xxy} = A^{eee}_{xyx}$,

Table 1. NRT element signs with respect to measurement geometry (M-T, metal side, transmission; M-R, metal side, reflection; S-T, substrate side, transmission; S-R, substrate side, reflection).

Geometry	A^{eee}_{xxx}	A^{eem}_{xxy}	A^{mee}_{yxx}	A^{eee}_{xyy}	A^{eem}_{xyx}	A^{mee}_{yyy}	A^{eee}_{xxy}	$(A^{eem}_{xyy} - A^{eem}_{xxx})$	A^{mee}_{yxy}
M-T	+	−	−	+	+	−	−	+	+
M-R	+	−	+	+	+	+	−	+	−
S-T	+	+	+	+	−	+	+	+	+
S-R	+	+	−	+	−	−	+	+	−

and the associated components of the magnetic tensors. The x-polarized signal for metal side incidence and transmitted direction is then found to be

$$E_x(2\omega) = \left(A^{eee}_{xxx} + A^{eem}_{xxy} + A^{mee}_{yxx}\right) E^2_x(\omega) + \left(A^{eee}_{xyy} - A^{eem}_{xyx} + A^{mee}_{yyy}\right) E^2_y(\omega) + \left[A^{eee}_{xxy} + \left(A^{eem}_{xyy} - A^{eem}_{xxx}\right) + A^{mee}_{yxy}\right] E_x(\omega) E_y(\omega). \tag{12}$$

In addition, the signs of the various components for the various measured signals are given in table 1. Note that table 1 shows that the tensor components A^{eem}_{xyy} and A^{eem}_{xxx} cannot be separated from each other but can only be measured as the combination $A^{eem}_{xyy} - A^{eem}_{xxx}$.

It is also important to note that absolute signal levels are extremely difficult to calibrate during the measurements. We will therefore take advantage of the fact that the strengths of the various interactions are likely to depend on the state of polarization of the fundamental beam. Our technique is therefore based on manipulating the polarization of the fundamental field continuously while the SH signals are recorded, which leads to varying interference between the different tensor components. Furthermore, the experimentally measured quantities are the irradiances of the SH field. Each measured signal can therefore be fitted to the functional form

$$I_{2\omega} = \left| f E^2_x(\omega) + g E^2_y(\omega) + h E_x(\omega) E_y(\omega) \right|^2, \tag{13}$$

where f, g and h are the fitting parameters expressing the contributions from different quadratic combinations of the polarization components of the fundamental field. It is evident that, except for trivial scaling constants, the parameters are of the form

$$\begin{aligned} f &= A^{eee}_{xxx} \pm A^{eem}_{xxy} \pm A^{mee}_{yxx}, \\ g &= A^{eee}_{xyy} \mp A^{eem}_{xyx} \pm A^{mee}_{yyy}, \\ h &= A^{eee}_{xxy} \pm \left(A^{eem}_{xyy} - A^{eem}_{xxx}\right) \pm A^{mee}_{yxy}, \end{aligned} \tag{14}$$

where the proper signs for each signal are given in table 1.

By measuring and analyzing all the four signals, we therefore obtain various combinations of the tensor components. The results can thus be used to construct a group of linear equations, where the unknowns are the tensor components and arbitrary scaling constants between the four signals. In the present case, the measured results provide a sufficient number of independent parameters that allow all of the unknowns to be uniquely determined.

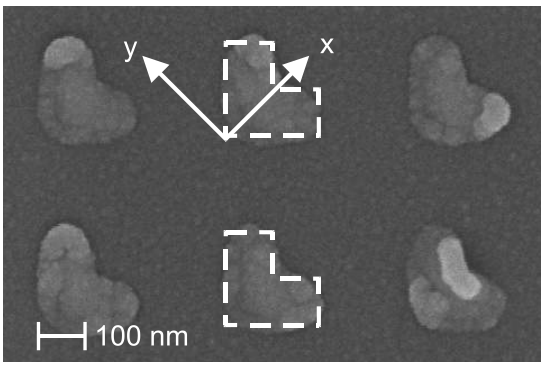

Figure 2. Scanning electron micrograph of the sample with the principal axes marked.

3. Experimental methods

Our sample consisted of an array of L-shaped gold nanoparticles. The linewidth of the particle arms is about 100 nm, the arm length is about 200 nm and the thickness of the metal layer is about 20 nm. The particles are ordered in a square lattice with a 400 nm period. The sample is covered with a 20 nm thick protective layer of silica. The active area of the sample is 1 mm × 1 mm. A scanning electron micrograph of the sample is shown in figure 2. The nanoparticles were deposited on a silica glass substrate using standard electron-beam lithography and the lift-off process [37].

The symmetry of an ideal L-shaped particle with equal arm lengths dictates a natural coordinate system for the sample. The principal axes denoted as x and y are rotated by 45° relative to the electron-beam lithography writing system. For the case of ideal, symmetric particles, the x-axis is a mirror symmetry axis. Reflection with respect to this axis is the only symmetry operation for the sample. However, in the case of a real structure, the symmetry is broken due to shape distortions from the ideal and by the surface defects. The ideal geometrical L outline in figure 2 emphasizes the deviation of the real sample from the ideal. The sample exhibits strong dichroism [38], with x- and y-polarizations having well-defined plasmonic resonances at the wavelengths of about 1050 and 1500 nm, respectively.

The experiments were performed using a femtosecond Nd:glass laser (200 fs pulse length, 82 MHz repetition rate and 320 mW average power) as the source of fundamental light (figure 3). The x-polarization plasmonic resonance is thus close to the laser wavelength of 1060 nm. In addition, for the x-polarized fundamental beam, the x-polarized SH signal, described by the tensor component A^{eee}_{xxx}, is electric-dipole-allowed by the ideal structural symmetry of the sample. Focusing the present study on the x-polarized SH signals is therefore particularly relevant for demonstrating the capabilities of our new measurement technique in addressing the interplay of plasmon resonances and various multipole effects in the nonlinear response of the sample.

The laser light is weakly focused on the sample (spot size about 200 μm). The state of polarization of the fundamental beam is controlled with a polarizer P1 (cf figure 3), passing the linear p-polarization (in the plane of incidence). During the measurements, the

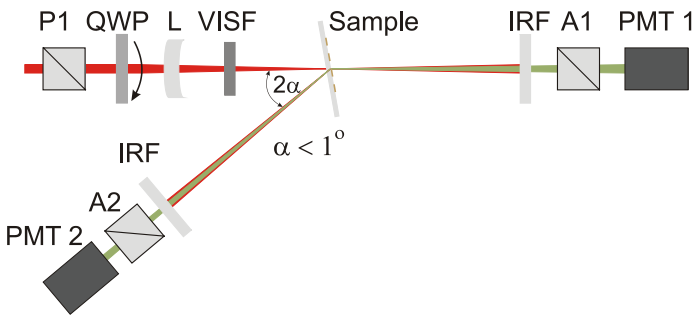

Figure 3. Experimental setup (VISF, visible blocking filter; IRF, infrared blocking filters; PMT 1, 2, photomultiplier tubes; P1, polarizer; A1, A2, analyzers).

state of polarization is modulated continuously with a quarter-wave plate (QWP), mounted in a computer-controlled, motorized rotation stage. Due to simultaneous measurements of the transmitted and reflected SHG signals, the sample is slightly (around 1°) tilted off normal with respect to the fundamental beam. We have performed several tests to verify that this angle is sufficiently small to make the coupling of the fields with the sample normal direction (z) insignificant [30, 31]. The s- and p-polarization components can thus be equated with the x- and y-polarizations, respectively.

The generated SHG light passes through an s-directed (normal to the plane of incidence) analyzer. The s-polarized SH signal is thus detected as a function of the fundamental beam polarization state controlled with the QWP rotation angle. The SHG signal is detected with a sensitive photomultiplier tube connected to a photon counting system. To make sure that the measured signal is SHG light and that it originates from the sample itself, visible and infrared blocking filters were used before and after the sample, respectively. The measurements were repeated for both orientations (metal and substrate side incidence) of the sample in the setup.

4. Results and discussion

The four measured signals as functions of the rotation angle of the QWP and their fits to equation (13) are shown in figure 4. In order to address whether an electric-dipole-only model could explain the data, the polarization lineshapes for the substrate-side incidence data have been reflected with respect to zero angle of the wave plate. This is because the change in the orientation of the sample reverses the sign of the y-coordinate of the sample, and hence this must be taken into account in describing how the wave plate modulates the state of polarization in the sample frame of reference (see also table 1). After this detail has been taken into account, all measured lineshapes would have to be identical if only electric dipoles were present.

The results of figure 4 have several interesting features. First, the overall features of all four lineshapes are very similar to each other, which would suggest that electric-dipole effects dominate the response. However, the lineshapes do have significant differences with regard to their details, both between the reflected and transmitted SHG signals and between the SHG signals for the metal and substrate side incidence of the fundamental beam. These

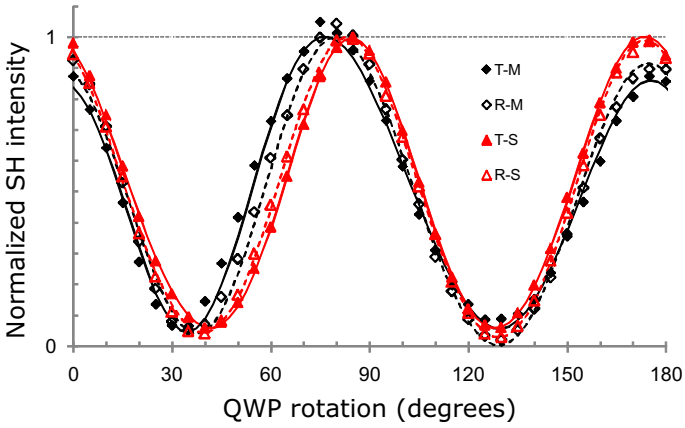

Figure 4. Comparison of data sets for different geometries of the measurement and their fits to the model of equation (13). The labels refer to transmission (T), reflection (R), metal incidence (M) and substrate incidence (S). Note that the results for the metal incidence are plotted from 0° to −180°, instead of 0° to 180°, to account for the change in sign of the y-coordinate between the two geometries.

Table 2. Results for the fits to equation (14). The error for all obtained values was estimated to be smaller than 0.03 units for both the real and imaginary parts.

NRT element	Value	Magnitude
A^{eee}_{xxx}	1	1
A^{eem}_{xxy}	$-0.239+0.408$i	0.473
A^{mee}_{yxx}	$0.034+0.041$i	0.054
A^{eee}_{xyy}	$0.794+0.063$i	0.797
A^{eem}_{xyx}	$0.233-0.315$i	0.392
A^{mee}_{yyy}	$0.012-0.033$i	0.035
A^{eee}_{xxy}	$0.199-0.086$i	0.217
$(A^{eem}_{xyy}-A^{eem}_{xxx})$	$0.438+0.137$i	0.459
A^{mee}_{yxy}	$0.003+0.007$i	0.007

differences already provide qualitative evidence of the importance of higher multipole effects at the fundamental and SH frequencies.

In order to obtain more quantitative information about the importance of the higher multipole effects, the fit parameters f, g and h for each measured signal were expressed in terms of the components of the tensors to set up a group of linear equations with the tensor components and scaling constants of the signals as unknowns. The solution is shown in table 2, where the values have been normalized to the electric-dipole-allowed component A^{eee}_{xxx}. The error for all obtained values was estimated to be smaller than 0.03 unit for both the real and the imaginary parts. Note that this component is electric-dipole-allowed for the ideal structure and

corresponds to the case where the fundamental wavelength is close to the plasmon resonance of this polarization. This component is indeed found to dominate the response. However, the other electric-dipole-allowed component A^{eee}_{xyy} is almost as large in magnitude, whereas the ideally forbidden component A^{eee}_{xxy} is significantly smaller.

The results also show that the higher multipole effects are much stronger in tensor A^{eem}_{ijk} than in tensor A^{mee}_{ijk}. The higher multipole effects are thus significantly more important at the fundamental frequency than at the SH frequency. This result is an important difference compared to our earlier results [30, 31], where the multipole effects were explained in terms of different radiative properties of the various multipoles, i.e. assuming that all multipole effects occur at the SH frequency. This new result could only be obtained by our new technique, where the sample is characterized in two different orientations (metal and substrate side incidence). The importance of higher multipole effects at the fundamental frequency is likely related to the fact that the particles support plasmonic resonances and thus strong local fields only at the fundamental frequency but not at the SH frequency. The field gradients favorable for the multipole effects are therefore stronger at the fundamental frequency.

It is also interesting to compare the relative importance of the higher multipole effects to the various measured signals. The electric-dipole-allowed resonant signal, which arises from the tensor components A^{eee}_{xxx}, A^{eem}_{xxy} and A^{mee}_{yxx}, is clearly dominated by electric-dipole effects, although higher multipoles also make a significant contribution. The same applies to the allowed signal due to A^{eee}_{xyy}, A^{eem}_{xyx} and A^{mee}_{yyy}. However, the forbidden signal, due to the components A^{eee}_{xxy}, $A^{eem}_{xyy} - A^{eem}_{xxx}$ and A^{mee}_{yxy}, which can only arise from sample imperfections (such as shape deviations from ideal and nanoscale defects), is dominated by the higher multipole components. This is in agreement with the earlier interpretation that higher multipole effects are associated with symmetry-breaking surface defects and field retardation [30, 31]. On the other hand, the role of higher multipole effects in the allowed signals suggests that not all surface defects need to break the symmetry and thus only contribute to retarded wavelets.

5. Conclusions

In conclusion, we have presented a new measurement technique that allows the role of the electric-dipole and higher-multipole contributions to the SH response of metal nanostructures to be addressed in detail. The technique is based on the effective medium approach where a total of three effective nonlinear response tensors are introduced to account for the electric-dipole interactions and the magnetic-dipole interactions to lowest-order at the fundamental and SH frequencies. The technique is based on the different transformation properties of the three tensors as the experimental geometry is manipulated. In particular, comparison of the SH signals emitted in the reflected and transmitted directions provides evidence of higher-multipole effects at the SH frequency [30, 31], whereas comparison of the signals for the fundamental beam incident on the metal and substrate sides provides complementary information that can be correlated with the presence of higher multiple effects at the fundamental frequency.

The present results show that the four measured signals have important differences in their details. The results for the sample investigated suggest that the dipolar response dominates; however, significant effects beyond electric dipoles are also present. Furthermore, the higher multipole effects are significantly more important at the fundamental frequency than at the SH frequency. In addition, the signal that is electric-dipole-forbidden for the ideal structure

is dominated by the higher multipole effects. This provides further support to the interpretation that the higher multipole effects are closely related to the surface defects of the sample. In the future, it will be interesting to investigate the role of the multipole effects under resonant and non-resonant excitation and for samples with varying surface quality.

Acknowledgments

We acknowledge the Academy of Finland (grant numbers 114913 and 132438) and the Nanophotonics Research and Development Program of the Ministry of Education of Finland for support of this work. MZ acknowledges the Wihuri Foundation for financial support. HH acknowledges support from the Graduate School of Tampere University of Technology and the Finnish Foundation for Technology Promotion.

References

[1] Kreibig U and Vollmer M 1995 *Optical Properties of Metal Clusters* (*Springer Series in Material Science*) (Berlin: Springer)
[2] Tsang T Y F 1996 Surface-plasmon-enchanced third-harmonic generation in thin silver films *Opt. Lett.* **21** 245
[3] Félidj N, Aubard J, Lévi G, Krenn J R, Salerno M, Schider G, Lamprecht B, Leitner A and Aussenegg F R 2002 Controlling the optical response of regular arrays of gold particles for surface-enhanced Raman scattering *Phys. Rev.* B **65** 075419
[4] Bouhelier A, Beversluis M, Hartschuh A and Novotny L 2003 Near-field second-harmonic generation induced by local field enhancement *Phys. Rev. Lett.* **90** 013903
[5] Stockman M I, Bergman D J and Kobayashi T 2004 Coherent control of nanoscale localization of ultrafast optical excitation in nanosystems *Phys. Rev.* B **69** 054202
[6] Shalaev V M, Poliakov E Y and Markel V A 1996 Small-particle composites. II. Nonlinear optical properties *Phys. Rev.* B **53** 2437–449
[7] Guyot-Sionnest P, Chen W and Shen Y 1986 General considerations on optical second-harmonic generation from surfaces and interfaces *Phys. Rev.* B **33** 8254
[8] Dadap J I, Shan J, Eisenthal K B and Heinz T F 1999 Second-harmonic Rayleigh scattering from a sphere of centrosymmetric material *Phys. Rev. Lett.* **83** 4045
[9] Dadap J I, Shan J and Heinz T F 2004 Theory of optical second-harmonic generation from a sphere of centrosymmetric material: small-particle limit *J. Opt. Soc. Am.* B **21** 1328–47
[10] Shan J, Dadap J I, Stiopkin I, Reider G A and Heinz T F 2006 Experimental study of optical second-harmonic scattering from spherical nanoparticles *Phys. Rev.* A **73** 023819
[11] Loudon R 1983 *The Quantum Theory of Light* 2nd edn (New York: Oxford University Press)
[12] Bachelier G, Russier-Antoine I, Benichou E, Jonin C and Brevet P-F 2008 Multipolar second-harmonic generation in noble metal nanoparticles *J. Opt. Soc. Am.* B **25** 955
[13] Kauranen M, Verbiest T, Maki J J and Persoons A 1994 Second-harmonic generation from chiral surfaces *J. Chem. Phys.* **101** 8193
[14] Kauranen M, Maki J J, Verbiest T, Elshocht S V and Persoons A 1997 Quantitive determination of electric and magnetic second-order susceptibility tensors of chiral surfaces *Phys. Rev.* B **55** R1985
[15] Elshocht S V, Verbiest T, Kauranen M, Persoons A, Langeveld-Voss B M W and Meijer E W 1997 Direct evidence of the failure of electric-dipole approximation in second-harmonic generation from a chiral polymer film *J. Chem. Phys.* **107** 8201
[16] Schanne-Klein M C, Hache F, Brotin T, Andraud C and Collet A 2001 Magnetic chiroptical effects in surface second-harmonic reflection *Chem. Phys. Lett.* **338** 159

[17] Oldenburg S J, Hale G D, Jackson J B and Halas N J 1999 Light scattering from dipole and quadrupole nanoshell antennas *Appl. Phys. Lett.* **75** 1063
[18] Kelly K L, Coronado E, Zhao L L and Schatz G C 2003 The optical properties of metal nanoparticles: the influence of size, shape, and dielectric environment *J. Phys. Chem.* B **107** 668
[19] Petschulat J, Menzel C, Chipouline A, Rockstuhl C, Tünnermann A, Lederer F and Pertsch T 2008 Multipole approach to metamaterials *Phys. Rev.* A **78** 043811
[20] Belardini A, Larciprete M C, Centini M, Fazio E, Sibilia C, Bertolotti M, Toma A, Chiappe D and Buatier de Mongeot F 2009 Tailored second harmonic generation from self-organized metal nano-wires arrays *Opt. Express* **17** 3603
[21] Krenn J, Schider G, Rechberger W, Lamprecht B, Leitner F, Aussenegg A and Weeber J 2000 Design of multipolar plasmon excitations in silver nanoparticles *Appl. Phys. Lett.* **77** 3379–81
[22] Klein M W, Enkrich C, Wegener M and Linden S 2006 Second-harmonic generation from magnetic metamaterials *Science* **313** 502–4
[23] Cho D J, Wang F, Zhang X and Shen Y R 2008 Contribution of the electric quadrupole resonance in optical metamaterials *Phys. Rev.* B **78** 121101
[24] Brudny V L, Mochán W L, Maytorena J A and Mendoza B S 2003 Second harmonic generation from a collection of nanoparticles *Phys. Status Solidi* b **240** 518–28
[25] Valencia C I, Méndez E R and Mendoza B S 2003 Second-harmonic generation in the scattering of light by two-dimensional particles *J. Opt. Soc. Am.* B **20** 2150–61
[26] Nappa J, Revillod G, Russier-Antoine I, Benichou E, Jonin C and Brevet P F 2005 Electric dipole origin of the second harmonic generation of small metallic particles *Phys. Rev.* B **71** 165407
[27] Nappa J, Russier-Antoine I, Benichou E, Jonin C and Brevet P F 2006 Second harmonic generation from small gold particles: from the dipolar to the quadrupolar response *J. Chem. Phys.* **125** 184712
[28] Petschulat J, Chipouline A, Tünnermann A, Pertsch T, Menzel C, Rockstuhl C and Lederer F 2009 Multipole nonlinearity of metamaterials *Phys. Rev.* A **80** 063828
[29] Butet J, Duboisset J, Bachelier G, Russier-Antoine I, Benichou E, Jonin C and Brevet P-F 2010 Second harmonic generation of single metallic nanoparticles embedded in a homogeneous medium *Nano Lett.* **10** 1717
[30] Kujala S, Canfield B K, Kauranen M, Svirko Y and Turunen J 2007 Multipole interference in the second-harmonic optical radiation from gold nanoparticles *Phys. Rev. Lett.* **98** 167403
[31] Kujala S, Canfield B K, Kauranen M, Svirko Y and Turunen J 2008 Multipolar analysis of second-harmonic radiation from gold nanoparticles *Opt. Express* **16** 17196
[32] Jackson J 1975 *Classical Electrodynamics* 2nd edn (New York: Wiley)
[33] Kauranen M, Verbiest T and Persoons A 1998 Second-order nonlinear optical signatures of surface chirality *J. Mod. Opt.* **45** 403
[34] Bai B and Turunen J 2007 Fourier modal method for the analysis of second-harmonic generation in two-dimensionally periodic structures containing anisotropic materials *J. Opt. Soc. Am.* B **24** 1105
[35] Canfield B K, Kujala S, Jefimovs K, Svirko Y, Turunen J and Kauranen M 2006 A macroscopic formalism to describe the second-order nonlinear optical response of nanostructures *J. Opt. A* **8** 278–84
[36] Pershan P 1963 Nonlinear optical properties of solids: energy considerations *Phys. Rev.* **130** 919
[37] Tuovinen H, Kauranen M, Jefimovs K, Vahimaa P, Vallius T, Turunen J, Tkachenko N V and Lemmetyinen H 2002 Linear and second-order nonlinear optical properties of arrays of noncentrosymmetric gold nanoparticles *J. Nonlinear Opt. Phys. Mater.* **11** 421
[38] Canfield B K, Kujala S, Laiho K, Jefimovs K, Turunen J and Kauranen M 2006 Chirality arising from small defects in gold nanoparticle arrays *Opt. Express* **14** 950–5

Paper 2

Robert Czaplicki, Mariusz Zdanowicz, Kalle Koskinen, Janne Laukkanen, Markku Kuittinen, and Martti Kauranen.

Dipole limit in second-harmonic generation from arrays of gold nanoparticles.

Optics Express **19**, 26866–26871 (2011)

Dipole limit in second-harmonic generation from arrays of gold nanoparticles

Robert Czaplicki,[1,*] Mariusz Zdanowicz,[1,2] Kalle Koskinen,[1] Janne Laukkanen,[3] Markku Kuittinen,[3] and Martti Kauranen[1]

[1]*Department of Physics, Tampere University of Technology, P.O. Box 692, FI-33101 Tampere, Finland*
[2]*National Institute of Telecommunications, Szachowa 1, PL-04894 Warsaw, Poland*
[3]*Department of Physics and Mathematics, University of Eastern Finland, FI-80101 Joensuu, Finland*
[*]*robert.czaplicki@tut.fi*

Abstract: We present a multipolar tensor analysis of second-harmonic generation from arrays of noncentrosymmetric gold nanoparticles. In contrast to earlier results, where higher multipoles and symmetry-forbidden signals arising from sample defects play a significant role, the present results are completely dominated by symmetry-allowed electric-dipole tensor components. The result arises from significant improvement in sample quality, which suppresses the higher-multipole effects and enhances the overall response by an order of magnitude. The results are a prerequisite for metamaterials with controllable nonlinear properties.

OCIS codes: (190.0190) Nonlinear optics; (310.6628) Subwavelength structures, nanostructures; (160.4236) Nanomaterials; (160.3900) Metals.

References and links

1. V. M. Shalaev, "Optical negative-index metamaterials," Nat. Photonics **1**(1), 41–48 (2007).
2. U. Kreibig and M. Vollmer, *Optical Properties of Metal Clusters*, Springer Series in Materials Science (Springer, New York, 1995).
3. K. L. Kelly, E. Coronado, L. L. Zhao, and G. C. Schatz, "The optical properties of metal nanoparticles: The influence of size, shape, and dielectric environment," J. Phys. Chem. B **107**(3), 668–677 (2003).
4. W. Cai, U. K. Chettiar, A. V. Kildishev, and V. M. Shalaev, "Optical cloaking with metamaterials," Nat. Photonics **1**(4), 224–227 (2007).
5. T. Ergin, N. Stenger, P. Brenner, J. B. Pendry, and M. Wegener, "Three-dimensional invisibility cloak at optical wavelengths," Science **328**(5976), 337–339 (2010).
6. B. K. Canfield, H. Husu, J. Laukkanen, B. Bai, M. Kuittinen, J. Turunen, and M. Kauranen, "Local field asymmetry drives second-harmonic generation in non-centrosymmetric nanodimers," Nano Lett. **7**(5), 1251–1255 (2007).
7. M. W. Klein, M. Wegener, N. Feth, and S. Linden, "Experiments on second- and third-harmonic generation from magnetic metamaterials," Opt. Express **15**(8), 5238–5247 (2007).
8. F. B. P. Niesler, N. Feth, S. Linden, and M. Wegener, "Second-harmonic optical spectroscopy on split-ring-resonator arrays," Opt. Lett. **36**(9), 1533–1535 (2011).
9. B. K. Canfield, S. Kujala, K. Jefimovs, T. Vallius, J. Turunen, and M. Kauranen, "Polarization effects in the linear and nonlinear optical responses of gold nanoparticle arrays," J. Opt. A Pure Appl Opt. **7**(2), S110–S117 (2005).
10. B. K. Canfield, S. Kujala, K. Jefimovs, J. Turunen, and M. Kauranen, "Linear and nonlinear optical responses influenced by broken symmetry in an array of gold nanoparticles," Opt. Express **12**(22), 5418–5423 (2004).
11. J. A. H. van Nieuwstadt, M. Sandtke, R. H. Harmsen, F. B. Segerink, J. C. Prangsma, S. Enoch, and L. Kuipers, "Strong modification of the nonlinear optical response of metallic subwavelength hole arrays," Phys. Rev. Lett. **97**(14), 146102 (2006).
12. M. W. Klein, Ch. Enkrich, M. Wegener, and S. Linden, "Second-harmonic generation from magnetic metamaterials," Science **313**(5786), 502–504 (2006).
13. M. Gentile, M. Hentschel, R. Taubert, H. Guo, H. Giessen, and M. Fiebig, "Investigation of the nonlinear optical properties of metamaterials by second harmonic generation," Appl. Phys. B **105**(1), 149–162 (2011).
14. S. Kujala, B. K. Canfield, M. Kauranen, Y. Svirko, and J. Turunen, "Multipolar analysis of second-harmonic radiation from gold nanoparticles," Opt. Express **16**(22), 17196–17208 (2008).
15. M. I. Stockman, D. J. Bergman, C. Anceau, S. Brasselet, and J. Zyss, "Enhanced second-harmonic generation by metal surfaces with nanoscale roughness: nanoscale dephasing, depolarization, and correlations," Phys. Rev. Lett. **92**(5), 057402 (2004).
16. M. I. Stockman, "Nanoscience: Dark-hot resonances," Nature **467**(7315), 541–542 (2010).

#157528 - $15.00 USD Received 2 Nov 2011; revised 7 Dec 2011; accepted 7 Dec 2011; published 15 Dec 2011

17. M. Zdanowicz, S. Kujala, H. Husu, and M. Kauranen, "Effective medium multipolar tensor analysis of second harmonic generation from metal nanoparticles," New J. Phys. **13**(2), 023025 (2011).
18. J. Nappa, G. Revillod, I. Russier-Antoine, E. Benichou, C. Jonin, and P.-F. Brevet, "Electric dipole origin of the second harmonic generation of small metallic particles," Phys. Rev. B **71**(16), 165407 (2005).
19. J. Butet, G. Bachelier, I. Russier-Antoine, C. Jonin, E. Benichou, and P.-F. Brevet, "Interference between selected dipoles and octupoles in the optical second-harmonic generation from spherical gold nanoparticles," Phys. Rev. Lett. **105**(7), 077401 (2010).
20. J. I. Dadap, J. Shan, K. B. Eisenthal, and T. F. Heinz, "Second-harmonic rayleigh scattering from a sphere of centrosymmetric material," Phys. Rev. Lett. **83**(20), 4045–4048 (1999).
21. S. Roke, M. Bonn, and A. V. Petukhov, "Nonlinear optical scattering: The concept of effective susceptibility," Phys. Rev. B **70**(11), 115106 (2004).
22. A. G. F. de Beer, S. Roke, and J. I. Dadap, "Theory of optical second-harmonic and sum-frequency scattering from arbitrarily shaped particles," J. Opt. Soc. Am. B **28**(6), 1374–1384 (2011).
23. H. Husu, J. Mäkitalo, J. Laukkanen, M. Kuittinen, and M. Kauranen, "Particle plasmon resonances in L-shaped gold nanoparticles," Opt. Express **18**(16), 16601–16606 (2010).
24. B. K. Canfield, S. Kujala, K. Jefimovs, Y. Svirko, J. Turunen, and M. Kauranen, "A macroscopic formalism to describe the second-order nonlinear optical response of nanostructures," J. Opt. A Pure Appl. Opt. **8**(4), S278–S284 (2006).
25. M. Kauranen, T. Verbiest, and A. Persoons, "Second-order nonlinear optical signatures of surface chirality," J. Mod. Opt. **45**(2), 403–423 (1998).
26. S. Kujala, B. K. Canfield, M. Kauranen, Y. Svirko, and J. Turunen, "Multipole interference in the second-harmonic optical radiation from gold nanoparticles," Phys. Rev. Lett. **98**(16), 167403 (2007).

Metamaterials are artificial nanostructures whose optical properties arise from the geometry of their structural features [1]. Such materials often consist of arrays of metal nanoparticles whose optical properties are dominated by the collective oscillations of the conduction electrons in the particles. The oscillations give rise to plasmonic and magnetic resonances, which depend on the size, shape, dielectric environment, and mutual ordering of the particles [2,3]. The resonances can lead to strong electromagnetic fields near the particles and thus enhance optical interactions. The linear optical responses tailored in such ways are utilized, e.g., to achieve negative index of refraction [1] or cloaking [4,5].

The local-field enhancement is particularly important for nonlinear optical processes, which scale with a high power of the field. For second-order effects, noncentrosymmetric structures are needed, and the response is also otherwise very sensitive to symmetry. Such structures have been characterized by second-harmonic generation (SHG) in order to understand the role of the structural features [6,7] and resonance enhancement [8,9] in the efficiency of SHG.

An important problem in these efforts has been that the selection rules between the allowed and forbidden SHG signals, as derived from the ideal structural symmetry, have not been fulfilled [10–13]. In some cases, forbidden signals have even dominated the response [14]. This problem arises from symmetry-breaking nanoscale defects of the structures. The defects can act as attractors for particularly strong local fields [15,16] and thus play a disproportionate role in the second-order response. Even when the local response of the defects is dipolar, they give rise to characteristic higher-multipole (magnetic-dipole and electric-quadrupole) features in SHG when analyzed using effective-medium concepts appropriate for metamaterials [14]. In the most detailed analysis to date, the tensor components associated with higher-multipole effects were up to 50% in magnitude compared to the dominant electric-dipole component [17]. Furthermore, the symmetry-forbidden signals were dominated by higher-multipole effects, thus emphasizing their connection to defects. It is evident that it is not acceptable to have random defects significantly influence the nonlinear response if one aims to develop nonlinear metamaterials with the response tailored by the structural features of the sample. Beyond results regarding multipole effects in coherent SHG, their role has also been addressed in incoherent hyper-Rayleigh scattering [18,19], described with different levels of detail from first-principles approaches [20] to effective quantities [21,22].

In this study, we show that the dipole limit of SHG can be reached by using nanostructured samples with significantly improved quality. We prepare an array of noncentrosymmetric gold nanoparticles and analyze its response in terms of effective electric-dipole and higher-multipole tensors. We show that the response is dominated by the

#157528 - $15.00 USD Received 2 Nov 2011; revised 7 Dec 2011; accepted 7 Dec 2011; published 15 Dec 2011

symmetry-allowed electric-dipole tensor components. The higher-multipole tensor components are found to be at most a few percent of the dominant dipolar component and for most cases well below this. In addition, the nonlinear response is enhanced by a factor of 10 compared to samples of earlier generation with lower quality. We have thus essentially reached the dipole limit in SHG, implying that the response is dominated by the overall features of the sample, not by random defects. This is a prerequisite for tailoring the nonlinear response in a controllable way by the structural features of the sample.

Our sample consists of an array of L-shaped gold nanoparticles (Fig. 1(a)), prepared by electron-beam lithography and lift-off. The particle dimensions were chosen to yield a plasmonic resonance at the laser wavelength used for the SHG experiments (1060 nm). The nominal linewidth is 100 nm and both arms have the equal length of 250 nm. The thickness of the gold layer is 20 nm and there is a thin adhesion layer of chromium between the fused silica substrate and the gold. In addition, the sample was covered by a 20-nm thick protective layer of silica. The array period is 500 nm in both directions and the total sample area is 1 × 1 mm^2.

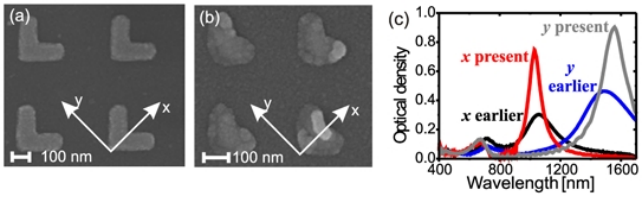

Fig. 1. SEM images and geometry of arrays of L-shaped nanoparticles for present, high-quality (a) and earlier, low-quality (b) samples. (c) *x*- and *y*-polarized extinction spectra of high- and low-quality samples.

For comparison, a sample from an earlier generation is also shown (Fig. 1(b)), where defects and higher multipole effects played a significant role in the SHG response [17]. The other main difference is that the array period of the old sample is 400 nm. It is evident from the SEM images of the quality of the present sample is significantly improved. The improvement is possible due to a new electron-beam lithography system, which has better accuracy and beam stability than the old system. The new system is also faster allowing smaller beam step size and thus improved line quality. Due to the high accelerating voltage (100 kV) of the new system, the forward scattering of electrons is smaller, which improves the shape control of the patterns further. Beyond the present sample, several others have been prepared with similar quality.

The samples are described using a coordinate system where *x* is the in-plane symmetry axis of the L shape and *y* is the orthogonal in-plane direction. The extinction spectra of the samples (Fig. 1(c)) were measured using fiber optic spectrometers at normal incidence. The samples are strongly dichroic with main resonances at similar wavelengths. The *x*-polarized resonances occur at 1033 nm (present sample) and 1060 nm (earlier sample) and the *y*-polarized resonances at 1554 nm (present) and 1490 nm (earlier). Additional resonances at 680 nm (present) and 710 nm (earlier) are related to the linewidth of the particles [23]. An important observation is that the extinction peak of the present sample is greatly enhanced and the linewidth narrowed. This is a direct consequence of the significantly improved sample quality with much less inhomogeneous broadening.

The nonlinear response is usually described by the nonlinear susceptibility tensor of the material. In nanostructures, however, the local fields and material properties exhibit nanoscale variations, which complicates such an approach. In order to avoid such nanoscale difficulties, we use the nonlinear response tensor (NRT) A_{ijk} [24], which operates on the level of input and output radiation fields

$$E_i(2\omega) = \sum_{jk} A_{ijk} E_j(\omega) E_k(\omega), \qquad (1)$$

#157528 - $15.00 USD Received 2 Nov 2011; revised 7 Dec 2011; accepted 7 Dec 2011; published 15 Dec 2011

where *ijk* refer to the polarization components of the respective fields. NRT is strictly specific to a given experiment rather than the sample itself. Its benefit is that it includes all multipole effects implicitly and it allows the signals to be analyzed using electric-dipole symmetry rules. Within the effective medium approach, NRT is proportional to the effective susceptibility of the nanostructure. Furthermore, the NRT approach can be extended to account for effective electric-dipole and higher-multipole effects. Due to difficulties in separating magnetic and quadrupole effects from each other in coherent signals [25], both are included in effective magnetic tensors. This results in three effective tensors, which describe electric-dipole interactions only $\left(A_{ijk}^{eee}\right)$, magnetic interactions at the fundamental frequency $\left(A_{ijk}^{eem}\right)$, and magnetic interactions at the second-harmonic frequency $\left(A_{ijk}^{mee}\right)$ [17].

The three tensors can be separated from each other by comparing SHG signals in the transmitted (T) and reflected (R) directions and for metal (M) and substrate (S) side incidence of the fundamental field [17]. When the fundamental beam is normally incident on the sample along *z* direction, any SHG signal can always be expressed in the general form

$$E_i(2\omega) = fE_x^2(\omega) + gE_y^2(\omega) + hE_x(\omega)E_y(\omega), \qquad (2)$$

where the expansion coefficients *f*, *g*, and *h* depend on the components of the three tensors and are different for the various experimental geometries. For our present sample, which exhibits a resonance for *x*-polarized fundamental field, the SHG signal is expected to be dominated by its *x*-polarized component. The expansion coefficients for *x*-polarized detection and the various experimental geometries are shown in Table 1. It is evident that if only symmetry-allowed (*f* and *g*) and dipolar effects play a role, all four signals should behave in the same way. On the other hand, symmetry-forbidden and higher-multipole effects contribute with varying signs to different signals, making possible the determination of all tensor components.

Table 1. The expansion coefficients expressed as function of NRT components for specific configurations. The signs depend on measurement geometry (M-: metal side incidence, S-: substrate side incidence, -T: transmission, -R: reflection). Note that *f* and *g* are allowed for the ideal symmetry of the L shape, whereas *h* is forbidden.

Geometry	*f*	*g*	*h*
M-T	$A_{xxx}^{eee} + A_{xxy}^{eem} + A_{yxx}^{mee}$	$A_{xyy}^{eee} - A_{yyx}^{eem} + A_{yyy}^{mee}$	$A_{xxy}^{eee} + (A_{xyy}^{eem} - A_{xxx}^{eem}) + A_{yxy}^{mee}$
M-R	$A_{xxx}^{eee} + A_{xxy}^{eem} - A_{yxx}^{mee}$	$A_{xyy}^{eee} - A_{yyx}^{eem} - A_{yyy}^{mee}$	$A_{xxy}^{eee} + (A_{xyy}^{eem} - A_{xxx}^{eem}) - A_{yxy}^{mee}$
S-T	$A_{xxx}^{eee} - A_{xxy}^{eem} - A_{yxx}^{mee}$	$A_{xyy}^{eee} + A_{yyx}^{eem} - A_{yyy}^{mee}$	$-A_{xxy}^{eee} + (A_{xyy}^{eem} - A_{xxx}^{eem}) + A_{yxy}^{mee}$
S-R	$A_{xxx}^{eee} - A_{xxy}^{eem} + A_{yxx}^{mee}$	$A_{xyy}^{eee} + A_{yyx}^{eem} + A_{yyy}^{mee}$	$-A_{xxy}^{eee} + (A_{xyy}^{eem} - A_{xxx}^{eem}) - A_{yxy}^{mee}$

Our experimental setup for SHG is shown in Fig. 2. A Nd:glass laser (200 fs pulse length, 82 MHz repetition rate) provided the fundamental beam at 1060 nm and its average power before the sample was 80 mW. The beam was weakly focused with 300 mm focal length lens on the sample, resulting in spot size of 300 μm. The polarization of the beam was set to *x* or y direction and then continuously modulated with a quarter-wave plate (QWP). Any possible

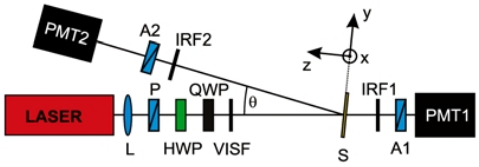

Fig. 2. Experimental setup. L – lens, P – polarizer, A1, A2 – analyzers, HWP – half-wave plate, QWP – quarter wave plate, VISF – visible blocking filter, IRF1, IRF2 – infrared blocking filters, PMT1, PMT2 – photomultiplier tubes.

#157528 - $15.00 USD Received 2 Nov 2011; revised 7 Dec 2011; accepted 7 Dec 2011; published 15 Dec 2011

SHG light from the optical components preceding the sample was filtered with a visible-blocking filter. The SHG signals were detected by photomultiplier tubes and photon counting by first filtering away the fundamental beam with infrared-blocking filters and using analyzers to pass only *x*-polarized SHG light.

The sample was slightly tilted off-normal with respect to fundamental beam (θ less than 2°) to allow detection of reflected SH radiation. The angle is sufficiently small that the fields do not couple significantly to the normal direction (*z*) of the sample [14,26].

The above measurements allow the relative complex values of the expansion coefficients to be determined for each signal separately. However, absolute calibration of the various signals is essentially impossible. The signals were thus separately normalized and their polarization lineshapes compared to obtain evidence of the presence or absence of higher multipole effects.

The measured signals (M-T, M-R, S-T and S-R) as functions of the rotation angle of the QWP and their fits to Eq. (2) are shown in Fig. 3. The lineshapes for S incidence have been reflected with respect to the zero angle of QWP to counter the sign change of the *y*-axis (*h* coefficient in Table 1) when the sample is flipped. All four signals should then show the same dependence on the polarization if only electric dipoles play role, whereas higher multipoles would lead to differences in the measured signals. All four measured lineshapes in Fig. 3 are seen to overlap almost perfectly. This result suggests that the SHG response of the present sample is strongly dominated by the electric-dipole interaction.

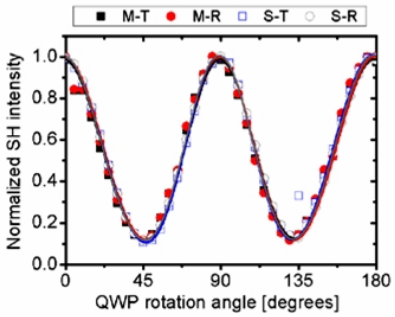

Fig. 3. Normalized transmitted (-T) and reflected (-R) SHG signals from an array of L-shaped gold nanoparticles for metal incidence (M-) and substrate incidence (S-), and from the present high-quality sample. Symbols represent the data from the measurements and solid lines are theoretical fits. The starting and detected linear polarization was *x*.

For more quantitative information about the various multipole effects, the fitted values of the coefficients *f*, *g* and *h* for the measured signals were compared to their expressions in terms of the components of the tensors (Table 1). This results in a group of linear equations, whose solution yields the relative complex values of the components (Table 2). The values are normalized to the dominant component A_{xxx}^{eee}, which has electric-dipole origin. A_{xxx}^{eee} is allowed for the ideal structure and has a plasmonic resonance at the fundamental wavelength.

The response is clearly dominated by the allowed electric-dipole components A_{xxx}^{eee} and A_{xyy}^{eee}, whereas the forbidden dipolar component A_{xxy}^{eee} is very weak. In addition, the magnitudes of the components of the two magnetic tensors remain below 2% of the dominant component with the exception of the combination $\left(A_{xyy}^{eem} - A_{xxx}^{eem}\right)$ which is 3.5%. Interestingly, this component is symmetry-forbidden, i.e., it arises from the residual imperfections of the sample. Nevertheless the results are a significant improvement compared to those for the low-quality particles shown in Fig. 1(b), where the higher multipolar components had magnitudes up to 50% of the dominant dipolar components [17].

#157528 - $15.00 USD Received 2 Nov 2011; revised 7 Dec 2011; accepted 7 Dec 2011; published 15 Dec 2011

In order to exclude any other possibilities for higher-multipole effects, we also measured the *y*-polarized SHG signals. They were always found to be weaker than the *x*-polarized signals by an order of magnitude and also dominated by electric-dipole effects. These results will thus not change the general conclusion presented above. Improvements in the sample quality have thus allowed us to reach essentially the dipole limit in the SHG response.

Table 2. Determined values of NRT components

Tensor component	Allowed	Value	Magnitude
A_{xxx}^{eee}	YES	1	1
A_{xxy}^{eem}	YES	–0.003	0.003
A_{yxx}^{mee}	YES	–0.0017	0.0017
A_{xyy}^{eee}	YES	0.3126-0.114i	0.3327
A_{xyx}^{eem}	YES	0.0094-0.0153i	0.018
A_{yyy}^{mee}	YES	–0.0074 + 0.0133i	0.0153
A_{xxy}^{eee}	NO	0.0084-0.002i	0.0086
$A_{xyy}^{eem} - A_{xxx}^{eem}$	NO	–0.0349 + 0.0033i	0.035
A_{yxy}^{mee}	NO	–0.0005 + 0.0038i	0.0039

We have also compared the maximum signal level from the present sample to that from the lower-quality sample. After accounting for the different particle densities of the two samples, the SHG response of the present sample was found to be a factor of 10 higher. This enhancement arises from the narrower resonance and better resonance enhancement at the fundamental wavelength.

In conclusion, we have shown that improvements in sample quality, obtained by state-of-the-art nanofabrication, lead to significant advances in their effective nonlinear optical properties. In particular, the symmetry rules for second-harmonic generation are well fulfilled and the higher-multipole effects, which have been associated with defects, are almost completely suppressed. Furthermore, the efficiency of second-harmonic radiation is enhanced by a factor of 10 compared to similar samples of earlier generation. We have thus reached, to a very good approximation, the desired dipole limit where the nonlinear response arises from the overall structural features of the sample and is not significantly influenced by random defects. This result is an essential prerequisite for designing nonlinear metamaterials with engineered properties.

Acknowledgments

This work was supported by the Academy of Finland (114913 and 132438). M. Z. acknowledges the Wihuri Foundation for financial support. The authors would like to thank Hannu Husu for fruitful discussions.

#157528 - $15.00 USD Received 2 Nov 2011; revised 7 Dec 2011; accepted 7 Dec 2011; published 15 Dec 2011

Paper 3

Mariusz Zdanowicz, Juha Harra, Jyrki Mäkelä, Esa Heinonen, Tingyin Ning, Martti Kauranen, and Goëry Genty.

Ordered multilayer silica-metal nanocomposites for second-order nonlinear optics.

Applied Physics Letters **103**, 251907 (2013)

Ordered multilayer silica-metal nanocomposites for second-order nonlinear optics

Mariusz Zdanowicz,[1,a)] Juha Harra,[1,b)] Jyrki M. Mäkelä,[1] Esa Heinonen,[2] Tingyin Ning,[1] Martti Kauranen,[1] and Goëry Genty[1]
[1]*Department of Physics, Tampere University of Technology, P.O. Box 692, FI-33101 Tampere, Finland*
[2]*Center of Microscopy and Nanotechnology, University of Oulu, P.O. Box 7150, FI-90014, Finland*

(Received 22 October 2013; accepted 6 December 2013; published online 18 December 2013)

We use aerosol synthesis to fabricate ordered metal-silica nanocomposites consisting of alternating layers of pure silica and silica nanoparticles decorated with silver nanodots. These multilayer structures preserve the narrow plasmon resonance of the nanodots even for high optical densities and allow second-harmonic generation due to spontaneous symmetry breaking arising from the interfaces between silica and nanoparticle layers. Our concept opens up perspectives for complex structures for advanced optical applications. © *2013 AIP Publishing LLC*. [http://dx.doi.org/10.1063/1.4852795]

P3

The optical responses of metal nanoparticles arise from the plasmonic oscillations of their conduction electrons. The resulting localized surface plasmon (LSP) resonances give rise to strong electromagnetic fields near the metal-dielectric interface. Such local-field enhancement has many attractive applications in biosensing,[1,2] imaging,[3,4] and solar cells.[5,6] In addition, the plasmon resonances depend sensitively on the particle size,[7,8] shape,[9–12] as well as their dielectric environment, allowing broad tailorability of the resonances for a given application.

The local-field enhancement is particularly important for nonlinear optical effects, which scale with a high power of the field. Indeed, enhancement of third-order effects, with no particular symmetry constraints, has been demonstrated in bulk-type metal-dielectric nanocomposites.[13,14] Second-order effects, such as second harmonic generation (SHG), on the other hand, require non-centrosymmetric samples, and their observation has so far been limited to surface geometries. Enhancement of SHG by rough metal surfaces was demonstrated early on in a traditional surface geometry where the incident beam is applied on the sample at oblique angle.[15] More recently, lithographic arrays of non-centrosymmetric particles have been introduced as second-order metamaterials whose response can be accessed at normal incidence,[16–19] but such samples are not easy to fabricate.

The nonlinear responses (both second and third-order) of a macroscopic sample can be enhanced by tuning the incident laser close to the plasmon resonance of the particles[20,21] or by increasing the density of the particles. Unfortunately, the latter approach spoils the quality (shape and linewidth) of the resonances either due to agglomeration of particles, which gives rise to inhomogeneous broadening,[22,23] or because of near field coupling.[24] An associated problem is the difficulty of fabricating bulk-type composite materials with the required non-centrosymmetry for second-order. For other types of materials, the organic ones in particular, the non-centrosymmetry can be induced afterwards by poling in an electric field[25] or by using self-assembly, which in some cases gives rise to a non-centrosymmetric structure.[26] With regard to metal nanostructures, the focus has been on the plasmonic enhancement of the nonlinearity,[27] but no methods have been demonstrated for fabricating thick non-centrosymmetric structures.

Nanoparticle synthesis by aerosol techniques is fairly inexpensive, simple, highly versatile, and also scalable.[28,29] Particles can be generated in a continuous process and deposited directly from the gas phase onto the desired substrate. Recently, aerosol techniques have been used to produce plasmonic metal nanoparticles from different materials and with various morphologies.[23,30,31] In addition, the synthesized nanoparticles have been incorporated into multilayer polymer films in order to achieve for example magnetic and plasmonic functionalities.[32] However, even though aerosol synthesized nanoparticles have been studied extensively using linear spectroscopy, their applicability in nonlinear optical materials remains to be explored.

In this Letter, we use aerosol techniques to fabricate ordered multilayer metal-silica nanocomposites with controllable linear and nonlinear optical responses. Our nanocomposites consist of alternating layers of silver-decorated silica particles and pure silica glass. The fabrication technique allows for precise control of the synthesis and deposition of the silver-decorated particles, thus preventing the formation of silver clusters and resulting in samples with reproducible optical properties. The shape of the plasmon resonance in the extinction spectrum of the ordered composites is perfectly maintained during the layer growth and its amplitude grows linearly as the number of layers increases. Significantly, we further show that symmetry is inherently broken due to interfaces between pure silica and a layer of decorated nanoparticles, resulting in spontaneous growth of a non-centrosymmetric structure and a SHG signal that increases with the number of layers. The SHG is dramatically larger than that observed from a single layer of decorated particles with equivalent thickness.

Silver-decorated silica nanoparticles (Fig. 1(a)) were synthesized in a continuous flow of nitrogen. The silica particles generated by chemical vapor synthesis from liquid tetraethyl orthosilicate (TEOS)[33] were subsequently sintered in

[a)]Also at Transmission and Optical Technologies Department, National Institute of Telecommunications, Szachowa Str. 1, 04-894 Warsaw, Poland.; Electronic mail: mariusz.zdanowicz@tut.fi.
[b)]M. Zdanowicz and J. Harra contributed equally to this work.

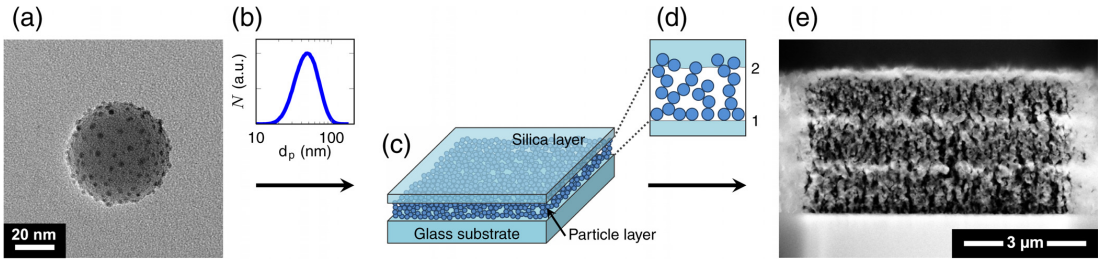

FIG. 1. (a) TEM image of a silver-decorated silica nanoparticle. (b) Size distribution of the silica particles (note the log scale in the horizontal axis). (c) Schematic image of one layer, which consist of a particle layer covered by a pure silica layer. (d) Schematic image of two neighboring interfaces explaining the symmetry breaking. (e) TEM image of the cross-section of a fabricated three-layer sample.

a tubular high-temperature furnace in order to obtain spherical carrier particles. Figure 1(b) shows the log-normal size distribution of the sintered silica particles, measured with a scanning mobility particle size (SMPS),[34] with a geometric mean diameter of 50 nm and a geometric standard deviation of 1.4. The silver decoration on the silica carrier particles was achieved by evaporation and subsequent condensation of silver from a small piece of bulk material.[31] This resulted in the formation of silver nanodots with diameters of 1–2 nm. The synthesized silver-decorated silica particles were then deposited from the gas phase onto glass substrates (1 mm thick microscope glass slides) by electrostatic collection.[35] The circular particle collection area on the substrate had a diameter of 2 cm.

The thickness of the particle layer on the substrate depends on collection time. Here, the collection time was set to 30 min, corresponding to particle layer thickness of approximately 1 μm with an estimated porosity of over 90%. This rough evaluation is based on the aerosol measurements (particle size and number concentration), particle collection parameters (gas flow rate, collection area and time) and realized layer thickness. Moreover, our estimation is consistent with previous reports of high porosity values for dry deposition of nanoparticles.[36] The layer of decorated nanoparticles was subsequently covered with a layer of pure silica using an electron-beam dielectric coater and with thickness, here approximately 200 nm, also determined by the deposition time (Fig. 1(c)). Repeating the particle deposition and coating processes multiple times and with identical deposition times allowed us to fabricate ordered multilayer nanocomposites whose linear and nonlinear optical properties can be controlled via the number of layers. Because the layer of silver-decorated particles is very porous, the silica coating penetrates it. However, the silica coating diffuses much less towards the bottom of the particle layer, and hence the overall symmetry of each layer is broken between the bottom and top interfaces (1 and 2, respectively, in Fig. 1(d)). Because each individual layer exhibits the same type of asymmetry the SHG response can grow significantly with the number of layers. In what follows, we use the term layer to refer to the combination of a single layer of decorated particles coated with a silica layer. Figure 1(e) shows a transmission electron microscope (TEM) image of the cross-section of a fabricated nanocomposite with three layers where the alternating layers of decorated nanoparticles and silica can be identified.

We first examined the linear optical properties of the fabricated samples. For this purpose, we measured their extinction spectra as a function of the number of layers with a high-sensitivity, high-resolution UV-Vis-NIR spectrophotometer (Shimadzu UV-3600). First, we clearly identify in each case the typical plasmon resonance of silver particles centered at around 370 nm (Fig. 2(a)) indicating the absence of silver clusters that would significantly broaden the resonance. Significantly, we also see how the magnitude of the extinction maximum grows linearly with the number of layers (see inset in Fig. 2(a)) and how the spectral location and width of the plasmon resonance remain unchanged with the number of layers. Oscillations visible for the wavelength

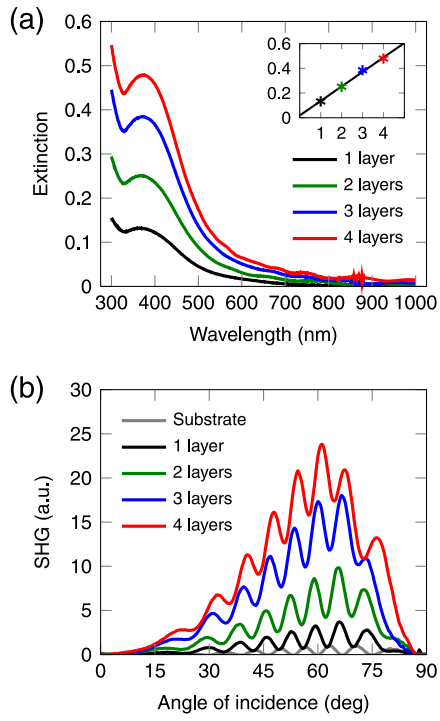

FIG. 2. (a) Extinction spectra of the multilayer nanocomposites. The inset shows the maximum extinction as a function of the number of layers. (b) Second-harmonic signal generated as a function of the angle of incidence.

TABLE I. Normalized SHG signals for different input-output polarization configurations.

p_{in}–p_{out}	s_{in}–p_{out}	p_{in}–s_{out}	s_{in}–s_{out}
1	8.9×10^{-2}	4.4×10^{-3}	0.7×10^{-3}

above 600 nm arise from weak Fabry-Perot effects within the active layers.

We then proceeded to investigate the second-order nonlinear response of the multilayer composites. The nonlinear response was characterized by measuring the SHG response as a function of the incidence angle in a Maker-fringe setup.[37,38] The fundamental beam was derived from a Nd:YAG laser producing 70 ps pulses at 1 kHz repetition rate and with 1064 nm wavelength. A 25 cm focal-length lens was used to weakly focus the beam into a spot size of around 20 μm at the sample plane, leading to the generation of SHG radiation at the 532 nm wavelength. Any potential SHG from the laser itself was removed with a long-pass IR filter inserted before the sample. The fundamental beam was blocked after the sample with a combination of a short-pass filter and an interference filter (central wavelength 532 nm, bandwidth 10 nm). The transmitted SHG signal was detected by a photomultiplier tube and the polarization states of the fundamental and SHG beams were controlled with calcite Glan polarizers. The sample was mounted on a high precision rotation stage to detect the SHG as a function of the angle of incidence. The SHG signal was found to be a highly directional beam, thus verifying the coherent character of the process.

The measurements were performed for samples consisting of 1 to 4 layers, for various polarization configurations and the maximum SHG was observed for the input and output polarizations parallel to the plane of incidence (p_{in}–p_{out} configuration, Table I). Very weak SHG signals for the p_{in}–s_{out} and s_{in}–s_{out} combinations suggest that the sample is isotropic in the plane of the sample as expected due to the fabrication process. In order to eliminate the possible influence of inhomogeneity in the sample plane, a series of measurements were conducted at ten different spatial locations on the samples. The SHG intensity was then averaged over all ten measurements. The results (Fig. 2(b)) show that the maximum of the SHG signal occurs for an incidence angle of approximately 60°. Most importantly, the strength of the SHG signal increases with the number of layers in the sample. The Maker-fringes are also clearly observed and result from interference between the SHG signals arising from the back side of the 1 mm thick glass substrate. The thickness of any composite itself is much smaller than that of the substrate and their effect on the Maker-fringes cannot be resolved. The shift of the SHG signal maximum originates from the fact that that the values of the susceptibility components for the active layers and the bottom surface of the substrate are different. As the active layer becomes thicker, its response becomes more important giving rise to changes in the fringe structure.

In order to evaluate the origin of the second-order response of the structures, we fabricated two additional control samples (see Fig. 3(a) for a schematic illustration). The first (CS1) consists of a single layer of silver-decorated particles coated with one layer of silica on top. Both layers were deposited so as to match the effective thicknesses of the respective layers in the four-layer sample. The other control sample (CS2), was prepared by depositing four layers of silica particles with no silver decoration. The collection time for the silica particles and the thickness of the deposited silica were identical to those of the four-layer sample with the silver decoration. The purpose of these two samples is two-fold: CS1 allows us to investigate the effect of structuring the samples into multiple layers whilst CS2 allows verifying the role of the silver particles in the nonlinear response.

We first compare in Fig. 3(b) the extinction spectra of the control samples and the four-layer sample. The linear response of the samples is seen to be essentially independent of the exact layer structure and only depends on the total silver and silica content. This can be understood from the fact that the only parameter that determines the overall extinction is the total amount of silver dots and silica and not the particular arrangement within the sample. This is an important result as it implies that any differences in the nonlinear response can be ascribed to the structuring of the samples into multiple layers. On the other hand, in the linear response of CS2 with no silver inclusions, we note, as expected, the absence of the plasmon resonance with an increase in the extinction for decreasing wavelengths consistent with typical silica absorption. These results clearly show that the extinction of the samples with silver-decorated particles is

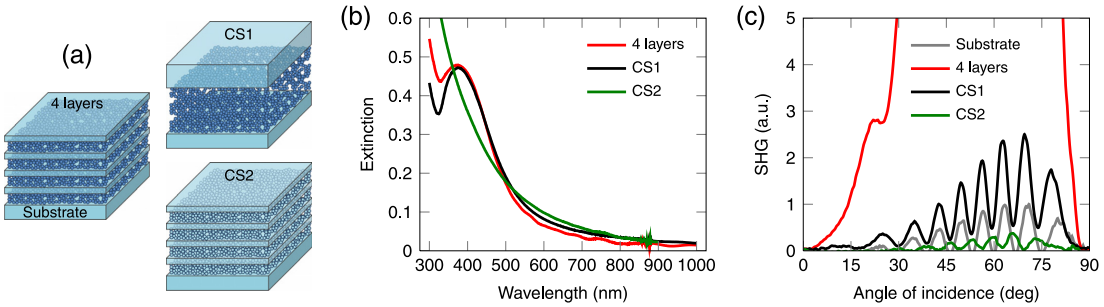

FIG. 3. (a) Schematic images of the multilayer nanocomposites and control samples. (b) Comparison of the extinction spectra between the four-layer sample and the control samples: CS1 with equivalent amount of metal and silica and CS2 with layers organized identically with four-layer structure, but without silver inclusions. (c) Comparison of the SH signal for the four-layer sample and the control samples CS1 and CS2.

dominated by the plasmon resonance as determined by the silver particle size and their total amount.

We subsequently performed the Maker-fringe experiments for the control samples under conditions identical to that of the multilayer composites. The results are presented in Fig. 3(c) along with the SHG intensity obtained from the four-layer structure and from the sole substrate. We first note that CS2 containing no decorated particles produces negligible SHG. In fact, the SHG signal from CS2 is even weaker than that from the substrate itself. On the other hand, CS1, which contains decorated particles, shows an increase in SHG compared to CS2 or the substrate, showing evidence of the importance of the silver nanoparticles in the SHG process. But most importantly, the SHG signal is more than order of magnitude weaker than that generated from the four-layer sample with the same quantity of silver. This is a truly remarkable result illustrating that (i) the multilayer structure plays a central role in enhancing SHG and (ii) SHG arises from the multiple coherent second-harmonic contributions induced by the symmetry-breaking arising from the differences between the top and bottom interfaces of each layer.

The SHG response from the multilayer samples can be modeled by assuming that each individual layer of silver-decorated nanoparticles covered with a silica layer is equivalent to a thin film source of SHG signal. Within this approximation and because the thickness of each layer is identical, the amplitude of the elementary SHG field generated from each layer is the same. With this model, we can express the total SHG field as $E_{SHG} = C(1 + Nb)$, where E_{SHG} represents the total SHG field generated within a nanocomposite with N active layers. Here, C is the normalization constant representing the SHG contribution from the back side of the substrate[39,40] and b is the contribution from one nanocomposite layer normalized to the response of the substrate. Note that to account for the possible phase differences in the elementary metal-dielectric sources, we allow b to be complex. The corresponding total intensity is given by $I_{SHG} = C^2|1 + Nb|^2$ and the measured SHG intensity averaged over all angles of incidence was fitted with this model as a function of the number of layers. The result (Fig. 4) shows excellent agreement with the experiment. The contribution from the thin film source manifested by parameter b exceeds that from the substrate which is normalized to 1, consistent with the observations of Fig. 3(c). Corresponding value of the conversion efficiency of the second-order process was estimated to be of the order of 10^{-12} for the 4-layer sample, based on the experimental data. We also remark that the imaginary part of b is extremely small (1.1×10^{-5}), which is consistent with the fact that the SHG wavelength of 532 nm is significantly detuned from the plasmon resonance (see Fig. 3(b)). In principle and according to our model, the strength of the SHG signal could be boosted even more by depositing more active layers in the structure. In fact, with our thickest four-layer sample, we already observe 43-fold stronger SHG signal than the one measured for the substrate (see Fig. 4). In addition, the structures prepared for the present experiments are non-optimized. Therefore we expect that further development and optimization process allows the second-order response to be increased even more.

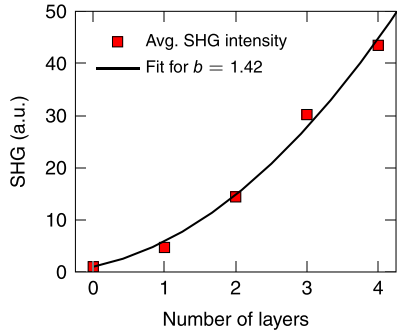

FIG. 4. Average SHG intensity as a function of the number of layers. Zero layers correspond to the substrate. The black line shows a fit with a model that separates contributions from the substrate and layers of the nanocomposite.

In conclusion, we have introduced a concept for the fabrication of silica-metal nanocomposites with controllable linear and nonlinear optical properties. Aerosol synthesis techniques were used to fabricate nanoparticle structures with enhanced nonlinear optical properties. The fabrication process allows creating ordered multilayer structures that preserve the shape of the plasmon resonance independently of the number of layers. We have further shown that separating multiple layers of decorated nanoparticles by silica results in an overall non-centrosymmetry that leads to second-harmonic generation that scales with the number of layers. Due to the flexibility of the used aerosol synthesis techniques, the material as well as the size of the carrier particles and the decorative nanodots can be varied to obtain nanocomposites with different optical responses (linear and nonlinear).

This work was supported by the Academy of Finland (136080 and 134980). M. Z. acknowledges the Wihuri Foundation for financial support. The authors thank Dr. Mari Honkanen (Department of Materials Science, Tampere University of Technology) for electron microscopy imaging, and Antti Rantamäki (Optoelectronics Research Centre, Tampere University of Technology) for preparing silica layers on the samples.

[1]T. Okamoto, I. Yamaguchi, and T. Kobayashi, Opt. Lett. **25**, 372 (2000).
[2]J. J. Mock, D. R. Smith, and S. Schultz, Nano Lett. **3**, 485 (2003).
[3]A. Holden, Photonics Nanostruct. Fundam. Appl. **3**, 96 (2005).
[4]J. B. Pendry, Phys. Rev. Lett. **85**, 3966 (2000).
[5]M. A. Green and S. Pillai, Nature Photonics **6**, 130 (2012).
[6]A. Pors, A. V. Uskov, M. Willatzen, and I. E. Protsenko, Opt. Commun. **284**, 2226 (2011).
[7]J. J. Mock, S. J. Oldenburg, D. R. Smith, D. A. Schultz, and S. Schultz, Nano Lett. **2**, 465 (2002).
[8]J. R. Heath, Phys. Rev. B **40**, 9982 (1989).
[9]J. Krenn, G. Schider, W. Rechberger, B. Lamprecht, A. Leitner, F. Aussenegg, and J. Weeber, Appl. Phys. Lett. **77**, 3379 (2000).
[10]N. J. Halas, Nano Lett. **10**, 3816 (2010).
[11]S. A. Maier, *Plasmonics: Fundamentals and Applications* (Springer, 2008).
[12]H. Husu, J. Mäkitalo, J. Laukkanen, M. Kuittinen, and M. Kauranen, Opt. Express **18**, 16601 (2010).
[13]J. E. Sipe and R. W. Boyd, Phys. Rev. A **46**, 1614 (1992).
[14]R. W. Boyd and J. E. Sipe, J. Opt. Soc. Am. B **11**, 297 (1994).
[15]C. K. Chen, A. R. B. de Castro, and Y. R. Shen, Phys. Rev. Lett. **46**, 145 (1981).

[16]H. Tuovinen, M. Kauranen, K. Jefimovs, P. Vahimaa, T. Vallius, J. Turunen, N.-V. Tkachenko, and H. Lemmetyinen, J. Nonlinear Opt. Phys. Mater. **11**, 421 (2002).
[17]S. Kujala, B. K. Canfield, M. Kauranen, Y. Svirko, and J. Turunen, Phys. Rev. Lett. **98**, 167403 (2007).
[18]R. Czaplicki, M. Zdanowicz, K. Koskinen, J. Laukkanen, M. Kuittinen, and M. Kauranen, Opt. Express **19**, 26866 (2011).
[19]M. W. Klein, C. Enkrich, M. Wegener, and S. Linden, Science **313**, 502 (2006).
[20]F. Niesler, N. Feth, S. Linden, J. Niegemann, J. Gieseler, K. Busch, and M. Wegener, Opt. Lett. **34**, 1997 (2009).
[21]M. Hentschel, T. Utikal, H. Giessen, and M. Lippitz, Nano Lett. **12**, 3778 (2012).
[22]G. Xu, M. Tazawa, P. Jin, and S. Nakao, Appl. Phys. A **80**, 1535 (2005).
[23]J. Harra, J. Mäkitalo, R. Siikanen, M. Virkki, G. Genty, T. Kobayashi, M. Kauranen, and J. M. Mäkelä, J. Nanopart. Res. **14**, 870 (2012).
[24]S. Linden, F. B. P. Niesler, J. Förstner, Y. Grynko, T. Meier, and M. Wegener, Phys. Rev. Lett. **109**, 015502 (2012).
[25]D. M. Burland, R. D. Miller, and C. A. Walsh, Chem. Rev. **94**, 31 (1994).
[26]S. I. Stupp, V. LeBonheur, K. Walker, L. S. Li, K. E. Huggins, M. Keser, and A. Amstutz, Science **276**, 384 (1997).
[27]K. Chen, C. Durak, J. R. Heflin, and H. D. Robinson, Nano Lett. **7**, 254 (2007).
[28]A. Gurav, T. Kodas, T. Pluym, and Y. Xiong, Aerosol Sci. Technol **19**, 411 (1993).
[29]F. Kruis, H. Fissan, and A. Peled, J. Aerosol Sci. **29**, 511 (1998).
[30]G. A. Sotiriou, T. Sannomiya, A. Teleki, F. Krumeich, J. Vörös, and S. E. Pratsinis, Adv. Funct. Mater. **20**, 4250 (2010).
[31]A. M. Boies, P. Lei, S. Calder, and S. L. Girshick, Nanotechnology **22**, 315603 (2011).
[32]G. A. Sotiriou, C. O. Blattmann, and S. E. Pratsinis, Adv. Funct. Mater. **23**, 34 (2013).
[33]A. Binder, A. Heel, and G. Kasper, Chem. Vap. Deposition **13**, 48 (2007).
[34]S. C. Wang and R. C. Flagan, Aerosol Sci. Technol. **13**, 230 (1990).
[35]T. J. Krinke, K. Deppert, M. H. Magnusson, F. Schmidt, and H. Fissan, J. Aerosol Sci. **33**, 1341 (2002).
[36]L. Mädler, A. Roessler, S. Pratsinis, T. Sahm, A. Gurlo, N. Barsan, and U. Weimar, Sens. Actuators B **114**, 283 (2006).
[37]P. D. Maker, R. W. Terhune, M. Nisenoff, and C. M. Savage, Phys. Rev. Lett. **8**, 21 (1962).
[38]J. Jerphagnon and S. K. Kurtz, J. Appl. Phys. **41**, 1667 (1970).
[39]The literature values for the surface susceptibility of glass vary but are on the order of 10^{-22} m^2/V, see Ref. 40.
[40]F. J. Rodriguez, F. X. Wang, and M. Kauranen, Opt. Express **16**, 8704 (2008).

P3

Paper 4

Mariusz Zdanowicz, Juha Harra, Jyrki Mäkelä, Esa Heinonen, Tingyin Ning, Martti Kauranen, and Goëry Genty.

Second-harmonic response of multilayer nanocomposites of silver-decorated nanoparticles and silica.

Scientific Reports **4**, 5745 (2014)

SCIENTIFIC REPORTS

OPEN

SUBJECT AREAS:
NANOPARTICLES
NONLINEAR OPTICS

Received
21 May 2014

Accepted
30 June 2014

Published
18 July 2014

Correspondence and requests for materials should be addressed to M.Z. (mariusz.zdanowicz@tut.fi.)

Second-harmonic response of multilayer nanocomposites of silver-decorated nanoparticles and silica

Mariusz Zdanowicz[1], Juha Harra[1], Jyrki M. Mäkelä[1], Esa Heinonen[2], Tingyin Ning[1], Martti Kauranen[1] & Goëry Genty[1]

[1]Department of Physics, Tampere University of Technology, P.O.Box 692, FI-33101 Tampere, Finland, [2]Center of Microscopy and Nanotechnology, P.O.Box 7150, FI-90014 University of Oulu, Finland.

We perform a detailed characterisation of the second-order nonlinear optical response of nanocomposites consisting of alternating layers of silver-decorated silica glass nanoparticles and pure silica glass. The samples are fabricated using aerosol techniques and electron-beam dielectric coating, resulting in a bulk-like material with symmetry-breaking induced by the porosity of the alternating layers. The second-order nonlinear response increases with the number of layers. Further, by determining the components of the second-order susceptibility tensor of the samples, we show that the structural properties of the samples are well maintained as the sample thickness is increased. Our results form an important baseline for any further optimization of these types of structures, which can be fabricated using very straightforward methods.

Metal nanostructures and composite nanomaterials play a significant role in linear and nonlinear optics. The optical responses of metal nanoparticles arise from the collective oscillations of their conduction electrons, and the characteristics of the resulting localized surface plasmon resonances strongly depend on several parameters, such as the nanoparticle shape[1–4], size[5–7], orientation and dielectric environment. In the past decade, significant progress in various fabrication techniques has allowed to explore a large variety of shapes and structures, as well as the effect of the mutual arrangement of the particles. This has led to remarkable improvements in controlling the optical properties of nanostructures, allowing their responses to be tailored for specific applications ranging from imaging[8,9] and biosensing[10,11] to solar cells[12,13].

The efforts on optical nanomaterials have followed two distinct lines. The first focuses on optimizing and understanding the enhanced optical responses of individual particles through particle shape (traditional spherical particles or ellipsoidal nanorice) or composition (solid vs. core-shell structures)[2]. The second line assembles collections of individual particles into nanocomposites with effective properties (metamaterials) enhanced compared to the constituent materials. The first effective-medium model for such composite materials was introduced more than a century ago by Maxwell-Garnett[14].

The effective medium approach is particularly important from the viewpoint of new types of nonlinear materials, where the macroscopic properties of the sample can play a crucial role in determining whether a significant response can be obtained or not. The model of Maxwell-Garnett has been extended to include nonlinear effects, and it has been shown that the third-order nonlinear susceptibility of a metal-dielectric bulk-type composite material can exceed that of either of its constituents and possess tensorial nonlinear properties very different from those of the host material[15–17].

The requirements for second-order materials are even more demanding, because second-order effects, such as second-harmonic generation, are only possible in noncentrosymmetric media. The observation of second-order effects in metals has thus been mainly limited to surface geometries where symmetry is broken at the metal-dielectric interfaces. For example, it is well-known that SHG can be enhanced by rough metal surfaces[18]. More recently, SHG has been demonstrated in lithographic arrays of non-centrosymmetric particles[19–22]. In our previous work, we have shown that bulk-type multilayer composites made of alternating layers of silver-decorated silica glass nanoparticles and fused silica intrinsically give rise to symmetry-breaking at each interface between the pure silica glass and layers of decorated particles, resulting in a spontaneous growth of an overall non-centrosymmetric structure[23]. However, these results based on a single SHG signal do not provide information on how well the order of the structure is maintained as its thickness is increased.

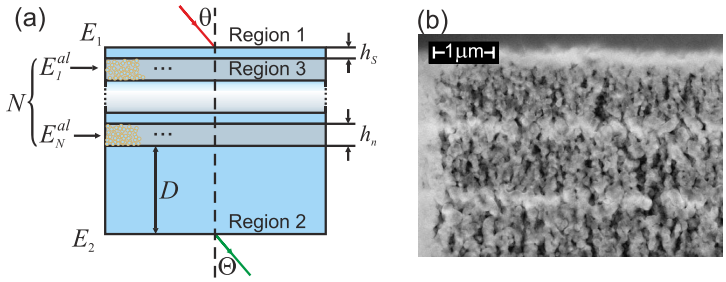

Figure 1 | (a) Schematic illustration of the nanocomposite samples. D is the thickness of the glass substrate, N is the number of layers, and h_n and h_S represent the thickness of silver-decorated nanoparticles and pure silica glass, respectively. The SHG sources with the effective contribution from a single layer E_k^{al} are indicated. (b) Transmission electron microscope image of the nanocomposite structure.

In this paper, we present a detailed experimental investigation of the second-order response for such a bulk-type second-order nanocomposite material. We determine the second-order susceptibility tensors of the samples of different thickness. By comparing the relative values of the various tensor components, we show that the structural properties of the samples are well maintained as the sample thickness is increased. The samples are shown to have the expected isotropy in the sample plane, and the independent components of the effective bulk susceptibility are found to be $\chi_{xxz}^{\mathrm{Ag/glass}} = 3.31$ fm/V, $\chi_{zxx}^{\mathrm{Ag/glass}} = 1.55$ fm/V, $\chi_{zzz}^{\mathrm{Ag/glass}} = 4.07$ fm/V (where z is the direction of the layer normal). Our results provide a convenient reference for further optimisation of these types of structures, which can be fabricated using very straightforward techniques.

Sample Fabrication and Measurements

The nanocomposite samples consist of alternating layers of silver-decorated silica glass nanoparticles and pure silica glass deposited on top of a 1 mm thick silica glass substrate (microscope glass slide). The layers are prepared using a combination of aerosol and dielectric coating techniques as described in detail in[23]. Samples with different numbers of layers were prepared with an effective area of about 3 cm^2. A schematic illustration of the nanocomposites together with an electron microscope image are shown in Fig. 1. The thickness of the layer consisting of metal nanoparticles is h_n=800 nm, and the deposited layer of silica glass has a thickness of h_S=200 nm.

Our previous results showed that the characteristics of the linear optical response of this type of nanocomposite are preserved during the multilayer growth and, in particular, the width and spectral position of the plasmon resonance remain independent of the amount of silver decorated particles and number of layers[23]. The measurement of the second-order nonlinear response further revealed that the intensity of the SHG signal grows with the number of layers with approximately the expected dependence[23].

To fully characterize the second-order nonlinear response of the composite samples, we perform SHG measurements using a neodymium YAG laser (1064 nm wavelength, 72 ps pulse length, 34 μJ pulse energy). Polarization dependent measurements allow us to verify the symmetry group of the samples. Subsequent Maker-fringe measurements allows us to verify, that the SHG signal grows with the sample thickness as expected. Finally, by comparing both sets of measurements, we verify that all results can be described by a unique set of tensor components.

First we make the measurements for different combinations of the fundamental and SHG polarizations. The polarization of the fundamental laser beam is modulated with a half-wave plate (HWP) and the intensities of the p- and s-polarized SHG signals are recorded as a function of the HWP rotation angle. The results show that the s-polarized SHG signal vanishes for both p- and s-polarized fundamental beams implying in full agreement with the expected in-plane isotropy ($C_{\infty v}$ symmetry group) of the sample and electric-dipole origin of the effective response. The non-vanishing second-order susceptibility tensor components are then limited to $\chi_{xxz} = \chi_{zxz} = \chi_{yyz} = \chi_{yzy}$, $\chi_{zxx} = \chi_{zyy}$ and χ_{zzz}, where z is the normal to the surface of the sample, and x and y represent orthogonal in-plane directions.

Next, we perform Maker-fringe charaterization[24,25] for four different samples with increasing number of nanoparticle-silica glass layers (1, 2, 3 and 4 layer samples) in the p_{in}-p_{out} polarization configuration. Measurements are also conducted for the glass substrate which is then used as the reference. A series of ten distinct measurements at different spatial positions on the sample surface is conducted to eliminate any effects from possible inhomogeneity, and the results are averaged over all ten measurements. The results for samples of different thickness are fitted to a unique set of tensor components and their compatibility with the polarization measurements is finally confirmed.

Modelling

In general, the p- and s-polarized SHG field components generated in an achiral thin film with in-plane isotropy can be expressed as $E_p = fe_p^2 + ge_s^2$, and $E_s = he_pe_s$,[26] where e_p and e_s represent the p- and s-polarized components of the fundamental beam, respectively, and f, g, and h are expansion coefficients that depend linearly on the susceptibility tensor components, angle of incidence, and linear optical properties of the material. Within the framework of a simplified Green's function formalism[27,28], where the multiple reflections within the thin nanocomposite layers and absorption are neglected, these expansion coefficients take the form

$$f = t_{p12}^2 T_{p21} \Delta_k^{(p)} [\chi_{xxz}^{\mathrm{Ag/glass}} \sin 2\theta_3 \cos\Theta_3 + \chi_{zxx}^{\mathrm{Ag/glass}} \cos^2\theta_3 \sin\Theta_3 + \chi_{zzz}^{\mathrm{Ag/glass}} \sin^2\theta_3 \sin\Theta_3], \quad (1)$$

$$g = t_{s12}^2 T_{p21} \Delta_k^{(s)} \chi_{zxx}^{\mathrm{Ag/glass}} \sin\Theta_3, \quad (2)$$

$$h = t_{s12} t_{p12} T_{s21} \Delta_k^{(ps)} \chi_{xxz}^{\mathrm{Ag/glass}} \sin\theta_3, \quad (3)$$

where $\Delta_k^{(p)}$, $\Delta_k^{(s)}$ and $\Delta_k^{(ps)}$ are the phase factors arising from the propagation of the fundamental, and second-harmonic fields inside of the structure with the total number of layers N, and are expressed with the sums:

$$\Delta_k^{(p)} = \sum_{k=1}^{N} t_{p23}^{2k} T_{p23}^{(N-k)} T_{p32}^{(N-k+1)} \exp[2i(w_2 k h_S + w_3(k-1)h_n)] \times \exp[i(W_2(D + h_S(N-k)) + W_3(N-k+1)h_n]. \quad (4)$$

$$\Delta_k^{(s)} = \sum_{k=1}^{N} t_{s23}^{2k} T_{p23}^{(N-k)} T_{p32}^{(N-k+1)} \exp[2i(w_2 k h_S + w_3(k-1)h_n)] \times \exp[i(W_2(D+h_S(N-k)) + W_3(N-k+1)h_n]. \quad (5)$$

$$\Delta_k^{(ps)} = \sum_{k=1}^{N} t_{s23}^{k} t_{p23}^{k} T_{p23}^{(N-k)} T_{p32}^{(N-k+1)} \exp[2i(w_2 k h_S + w_3(k-1)h_n)] \times \exp[i(W_2(D+h_S(N-k)) + W_3(N-k+1)h_n]. \quad (6)$$

The subscripts 1, 2 and 3 refer to air, silica glass, and nanocomposite layers, respectively (see marked areas on the schematic image in Fig. 1(a)), and $\tilde{w} = w/c$ is the reduced frequency (c is the speed of light in vacuum), h_S denotes the thickness of the silica layer and h_n the thickness of the nanocomposite active layers. In Eqs. 1–3, we have used lowercase and uppercase notation to define quantities at the fundamental and SHG frequencies, respectively. With this notation n_i (N_i) is the refractive index of the i^{th} region at the fundamental (SH) frequency, and θ_i (Θ_i) the angle of propagation of the fundamental (SH) radiation with respect to the structure normal inside the i^{th} region. Also: $w_i = \tilde{w} n_i \cos\theta_i$ ($W_i = 2\tilde{w} N_i \cos\Theta_i$). The coefficients t_{pij} and t_{sij} (T_{pij} and T_{sij}) account for the partial transmission of the s- and p- fundamental (SHG) field components at the interface between regions i and j, respectively, and they can be calculated from[28]

$$t_{sij} = \frac{2n_i \cos\theta_i}{n_i \cos\theta_i + n_j \cos\theta_j}, \quad (7)$$

$$t_{pij} = \frac{2n_i \cos\theta_i}{n_i \cos\theta_j + n_j \cos\theta_i}. \quad (8)$$

The refractive indices of the silver-decorated nanoparticle layers were calculated using an effective medium approach[16]. Taking into account the high porosity of the nanocomposite, we estimated $n_{Ag/glass}$ and $N_{Ag/glass}$ to be 1.102 and 1.122 at the fundamental and SH wavelengths, respectively[29]. Equations 1–8 can then be used to validate the results of the fitting of the three independent tensor components $\chi_{xxz}^{Ag/glass}$, $\chi_{zxx}^{Ag/glass}$ and $\chi_{zzz}^{Ag/glass}$ of a single active layer (decorated particles + silica glass) of the nanocomposite for the performed Maker-fringe fittings.

In order to evaluate the absolute values of the active layer tensor components and separate the contribution from the glass substrate, we calculate the SHG fields generated from each interface and the resulting total SHG amplitude. Because the different layers of the samples were prepared under identical conditions, we assume that each interface is an identical source of nonlinear radiation and contributes equally to the total SHG signal such that the total SHG amplitude simply corresponds to the sum of the interfering SHG fields generated at each interface. The SH intensity generated from the multilayer structure is then given by

$$I_{SHG} = |E_1 + E_2 + E_3|^2. \quad (9)$$

The SH fields E_1 and E_2 represent the contributions from the air-silica interface in region 1 and silica-air interface in region 2, respectively, and E_3 corresponds to the total contribution from the nanocomposite layers. For p-polarized fundamental and SHG light, as used in the Maker-fringe measurements, they can be expressed as[27,28]

$$E_1 = \frac{J}{W_2} t_{p12}^2 \left(T_{p23} T_{p32}\right)^N T_{p21} \exp[i\,(W_2(D+Nh_S) + W_3 N h_n)] \times \left\{\chi_{xxz}^{glass} \sin 2\theta_2 \cos\Theta_2 + \sin\Theta_2 \left[\chi_{zxx}^{glass} (\cos\theta_2)^2 + \chi_{zzz}^{glass} (\sin\theta_2)^2\right]\right\}, \quad (10)$$

and

$$E_2 = -\frac{J}{W_2} t_{p12}^2 \left(t_{p23} t_{p32}\right)^{2N} t_{p21}^2 \exp[i2(w_2(D+Nh_S) + w_3 N h_n)] \times \left\{\chi_{xxz}^{glass} \sin 2\theta_2 \cos\Theta_2 + \sin\Theta_2 \left[\chi_{zxx}^{glass} (\cos\theta_2)^2 + \chi_{zzz}^{glass} (\sin\theta_2)^2\right]\right\}. \quad (11)$$

Here, the constants $\chi_{xxz}^{glass} = 7.89 \times 10^{-22}$ m^2/V, $\chi_{zxx}^{glass} = 3.78 \times 10^{-22}$ m^2/V and $\chi_{zzz}^{glass} = 58.60 \times 10^{-22}$ m^2/V[30] represent the independent tensor components of the second-order surface response of the air-silica interface which are defined in terms of the fields inside the material. $J = i8\pi\tilde{\omega}^2 e_p^2$, on the other hand, is a constant, where e_p is the amplitude of the incident p-polarized beam and h_n, h_S and D denote the thickness of the silver-decorated nanoparticle layer, fused silica layer and glass substrate, respectively.

The total contribution E_3 of the nanocomposite multilayers (region 3 in Fig. 1) to the SH field consists of multiple silica-nanoparticles interfaces which depends on the number of deposited layers N as

$$E_3 = \sum_{k=1}^{N} E_k^{al}, \quad (12)$$

where the contribution E_k^{al} of the k^{th} layer to the total SHG signal is:

$$E_k^{al} = \frac{J}{W_3} t_{p12}^2 t_{p23}^{2k} t_{p32}^{2(k-1)} T_{p23}^{(N-k)} T_{p32}^{(N-k+1)} T_{p21} \times \exp\{i2[w_2 k h_S + w_3(k-1)h_n]\} \exp\{i[W_2(D+(N-k)h_S) + W_3(N-k+1)h_n]\} \times \left\{\chi_{xxz}^{Ag/glass} \sin 2\theta_3 \cos\Theta_3 + \sin\Theta_3 \left[\chi_{zxx}^{Ag/glass} (\cos\theta_3)^2 + \chi_{zzz}^{Ag/glass} (\sin\theta_3)^2\right]\right\}. \quad (13)$$

We are now in the position to determine the absolute values of the tensor components of a single active layer of the nanocomposite by fitting Eqs. 9–13 to the Maker-fringe patterns, and Eqs. 1–8 to the HWP polarization measurements.

Results

The results of the HWP measurements for different input/output polarization combinations at a 62° angle of incidence corresponding to maximum SHG signal are shown as squares and triangles in Fig. 2. They allow us to determine that the investigated samples posses in-plane isotropy, which limits the surface tensor components to the three independent elements as discussed above. The measurement for the 4-layer sample is presented in Fig. 2. The Maker-fringe measurement of a clean glass substrate alone (i.e. for the case of $N = 0$ in the model described with Eqs. 9–13) is illustrated in Fig. 3. The total

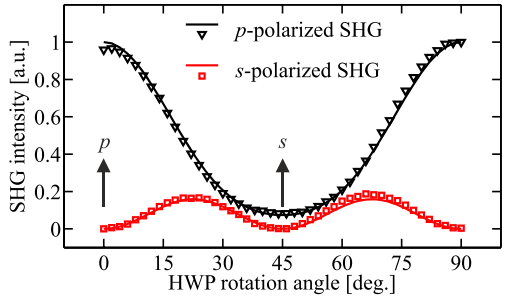

Figure 2 | Experimentally measured intensity at 532 nm for p- (black triangles) and s-polarized (red squares) SHG as a function of the HWP rotation angle modulating the polarization of the incident beam at 1064 nm. The angle of incidence was fixed to 62°. The results are normalized with respect to the p-polarized SHG intensity. Solid lines show the theoretical fits from Eqs. 1–8. The black arrows indicate the polarization of the incident fundamental field.

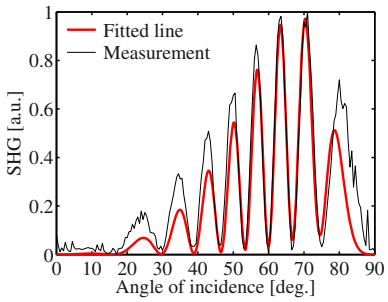

Figure 3 | Comparison between the theoretical model of Eqs. 9–11 (red solid line) and experimentally measured SHG intensity (black solid line) vs. angle of incidence for the glass substrate.

SH intensity reduces to contributions from the air-glass and glass-air interfaces only (see Eqs. 10 and 11) and we see very good agreement between the theoretical model and the experimentally measured data for refractive indices $n_{glass} = 1.45$ and $N_{glass} = 1.46$ at the fundamental and SHG wavelengths, respectively[29]. The thickness of the substrate was estimated to be $D = 1061.2$ μm in order to match the period of the Maker fringes between the theory and measurement. The Maker-fringe measurements for the nanocomposite are plotted in Fig. 4 as black solid lines and show a clear increase in the SH signal for a growing number of layers with a maximum signal at around 62° incidence. In order to fit these data with the model described by Eqs. 9–13, we first make coarse estimates of the thicknesses for all the samples, to match the fringe pattern with the experimental one. Next, we set the absolute values of the tensor components as free running parameters, and perform a robust fit using the least-square method. In the fitting procedure we account for all data points measured for all samples at the same time.

The results of the fits shown in Fig. 4 as red solid lines are in excellent agreement with the measured data for all the samples with different number of layers. In particular, the overall increase in the SH intensity as a function of the number of layers is correctly reproduced, as well as the modulation depth and period of the fringes. The corresponding absolute values of the nonlinear tensor components of the nanoparticle-silica interface obtained from the fit are summarized in Table I.

The values of the tensor components of the nanoparticle-silica interface $\chi_{xxz}^{Ag/glass}$, $\chi_{zxx}^{Ag/glass}$ and $\chi_{zzz}^{Ag/glass}$ are finally validated by the polarization measurements. Using Eqs. 1–3, we are now able to calculate the complex parameters *f*, *g*, and *h*. The calculated parameters are next used to draw the expected line shape for the HWP measurements. The fit is presented in Fig. 2 as solid lines. The results of the measurements are normalized with respect to the *p*-polarized data, as well as the calculated line shape. The measured data points and determined line are in excellent agreement, therefore validating the values of the tensor components.

Discussion

The dominant component of the nanocomposite layer interface is χ_{zzz}, however its value is lower than the same component of the glass surface. Note also, that the components χ_{zxx} and χ_{xxz} are also relatively large and unequal. These results allow us to make some conclusion about the character and possible origin of the nonlinear response of the nanocomposite. The components χ_{zxx} and χ_{xxz} must be equal when Kleinman symmetry is valid (i.e., far from any material resonances) or when the macroscopic nonlinearity arises from the orientational average of microscopic constituents whose nonlinearity is dominated by a single diagonal component of the hyperpolarizability tensor (which is the case for, e. g., rod-like push-pull molecules[31]). In the present case, our SHG wavelength is already at the wing of the plasmonic extinction band of the silver particles, whose presence is essential for the nonlinear response. The Kleinman symmetry is therefore not operative. In addition, if the silver nanoparticles are considered as the microscopic consitituents, their nonlinear response cannot be reduced to a single tensor component. Instead, more components need to be considered even on the

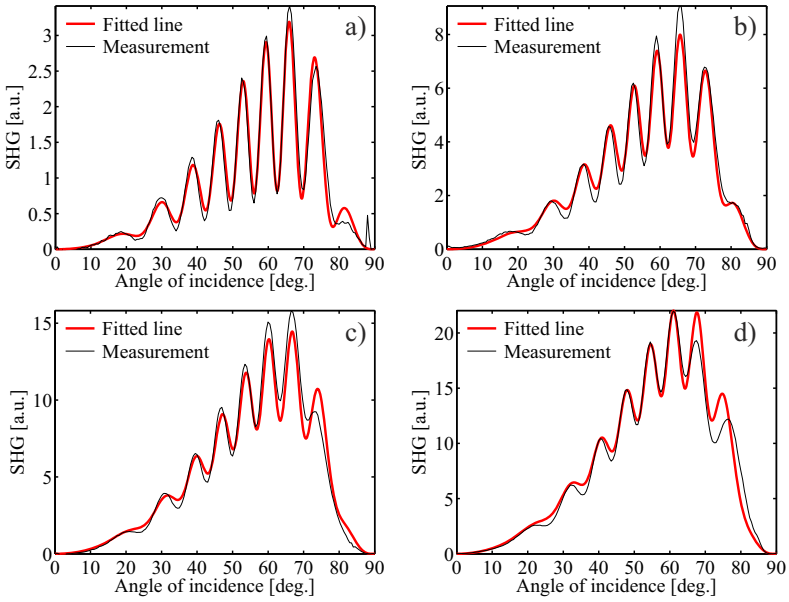

Figure 4 | Maker-fringe measurements (black solid line) with fitted model (red solid line). The averaged thicknesses of the silica glass and nanoparticles layers estimated from the microscope image (see Fig. 1(b)) are $h_S = 200$ nm and $h_n = 800$ nm, respectively. Number of layers: a) 1 layer sample, b) 2 layers sample, c) 3 layers sample, d) 4 layers sample.

Table I | Calculated absolute values for the surface tensor components of a single nanocomposite layer, as well as the effective bulk response obtained from these values

Surface tensor components	Absolute glass (10^{-22} m²/V)	Absolute Ag/glass composite (10^{-22} m²/V)	Ag/glass normalized magnitude	Effective bulk (fm/V)
χ_{xxz}	7.89	26.51	1	3.31
χ_{zxx}	3.78	12.37	0.47	1.55
χ_{zzz}	58.60	32.54	1.23	4.07

microscopic level, which will significantly complicate analyzing the connection between the microscopic and macroscopic responses. In addition, the fact that one of the off-diagonal components χ_{xxz} is almost as large as the diagonal component χ_{zzz} suggests that the orientational distribution of the microscopic constituents is relatively broad. This agrees well with the fact that the silver particles are randomly distributed on the surface of the silica particles. Hence, the properties of the silver particles are only modified by the porosity of the silica glass layer that leads to a varying dielectric environment around the silver particles at different vertical positions of a given silica particle. This suggests that the tensorial properties of the macroscopic nonlinearity could be tuned by controlling the porosity of the structure. Nevertheless, it is fair to say that it will be a significant challenge to build a detailed model that connects the microscopic origin of the nonlinearity to the macroscopic response.

We also note that the values of the bulk nonlinearity reported in Table I are relatively weak. This arises from the fact that the effective bulk response has been obtained by dividing the measured effective surface response by the layer thickness. For the present samples, the layer thickness is unnecessarily large and could easily be reduced by at least one order of magnitude, resulting in a more respectable bulk-type response. Further enhancement is expected from the optimization of the size and surface coverage of the silver decorated nanoparticles.

Conclusions

In conclusion, we have performed a detailed characterization of the second-order nonlinear response of multilayer silver nanoparticle-silica nanocomposites. Using a simplified Green's function formalism, which allows to describe mathematically the sources at the interfaces between the two materials, and fitting the Maker-fringe patterns of the multiple samples, we have determined all the independent tensor components of the nanocomposite samples. The fact that samples of different thickness can be described by a single set of nonlinear parameters shows that the level of ordering of the samples can be maintained for increasing sample thickness. The relative values of the tensor components allowed us to make some conclusions about the mechanism underlying the nonlinear response. The effective bulk nonlinearity of the investigated samples is relatively low but can likely be increased by reducing the sample thickness. It will also be interesting to investigate how much the nonlinear response can be boosted by increasing the amount of metal in the structure and by operating closer to the plasmon resonance. In any case, the present results provide a well-defined baseline for further optimization of these types of nanocomposite materials for second-order nonlinear effects.

1. Krenn, J. *et al.* Design of multipolar plasmon excitations in silver nanoparticles. *Appl. Phys. Lett.* **77**, 3379–3381; DOI:10.1063/1.1327615 (2000).
2. Maier, S. A. *Plasmonics: Fundamentals and Applications* (Springer, 2008).
3. Halas, N. J. Plasmonics: An emerging field fostered by nano letters. *Nano Lett.* **10**, 3816–3822; DOI: 10.1021/nl1032342 (2010).
4. Husu, H., Mäkitalo, J., Laukkanen, J., Kuittinen, M. & Kauranen, M. Particle plasmon resonances in l-shaped gold nanoparticles. *Opt. Express* **18**, 16601–16606; DOI:10.1364/OE.18.016601 (2010).
5. Heath, J. R. Size-dependent surface-plasmon resonances of bare silver particles. *Phys. Rev. B* **40**, 9982–9985; DOI:10.1103/PhysRevB.40.9982 (1989).
6. Mock, J. J., Oldenburg, S. J., Smith, D. R., Schultz, D. A. & Schultz, S. Composite plasmon resonant nanowires. *Nano Lett.* **2**, 465–469; DOI:10.1021/nl0255247 (2002).
7. Harra, J. *et al.* Size-controlled aerosol synthesis of silver nanoparticles for plasmonic materials. *J. Nanopart. Res.* **14**, 870; DOI:10.1007/s11051-012-0870-0 (2012).
8. Pendry, J. B. Negative refraction makes a perfect lens. *Phys. Rev. Lett.* **85**, 3966–3969; DOI:10.1103/PhysRevLett.85.3966 (2000).
9. Holden, A. Towards some real applications for negative materials. *Photonics Nanostruct.* **3**, 96–99; DOI:10.1016/j.photonics.2005.09.014 (2005).
10. Okamoto, T., Yamaguchi, I. & Kobayashi, T. Local plasmon sensor with gold colloid monolayers deposited upon glass substrates. *Opt. Lett.* **25**, 372–374; DOI:10.1364/OL.25.000372 (2000).
11. Mock, J. J., Smith, D. R. & Schultz, S. Local refractive index dependence of plasmon resonance spectra from individual nanoparticles. *Nano Lett.* **3**, 485–491; DOI:10.1021/nl0340475 (2003).
12. Pors, A., Uskov, A. V., Willatzen, M. & Protsenko, I. E. Control of the input efficiency of photons into solar cells with plasmonic nanoparticles. *Opt. Commun.* **284**, 2226–2229; DOI:10.1016/j.optcom.2010.12.067 (2011).
13. Green, M. A. & Pillai, S. Harnessing plasmonics for solar cells. *Nat. Photonics* **6**, 130–132; DOI:10.1038/nphoton.2012.30 (2012).
14. Garnett, J. C. M. Colours in metal glasses and in metallic films. *Philos. T. R. Soc. Lond.* **203**, 385–420; DOI:10.1098/rsta.1904.0024 (1904).
15. Ricard, D., Roussignol, P. & Flytzanis, C. Surface-mediated enhancement of optical phase conjugation in metal colloids. *Opt. Lett.* **10**, 511–513; DOI:10.1364/OL.10.000511 (1985).
16. Sipe, J. E. & Boyd, R. W. Nonlinear susceptibility of composite optical materials in the maxwell garnett model. *Phys. Rev. A* **46**, 1614–1629; DOI:10.1103/PhysRevA.46.1614 (1992).
17. Boyd, R. W. & Sipe, J. E. Nonlinear optical susceptibilities of layered composite materials. *J. Opt. Soc. Am. B* **11**, 297–303; DOI:10.1364/JOSAB.11.000297 (1994).
18. Chen, C. K., de Castro, A. R. B. & Shen, Y. R. Surface-enhanced second-harmonic generation. *Phys. Rev. Lett.* **46**, 145–148; DOI:10.1103/PhysRevLett.46.145 (1981).
19. Tuovinen, H. *et al.* Linear and second-order nonlinear optical properties of arrays of noncentrosymmetric gold nanoparticles. *J. Nonlinear Opt. Phys.* **11**, 421–432; DOI:10.1142/S0218863502001103 (2002).
20. Kujala, S., Canfield, B. K., Kauranen, M., Svirko, Y. & Turunen, J. Multipole interference in the second-harmonic optical radiation from gold nanoparticles. *Phys. Rev. Lett.* **98**, 167403; DOI:10.1103/PhysRevLett.98.167403 (2007).
21. Czaplicki, R. *et al.* Dipole limit in second-harmonic generation from arrays of gold nanoparticles. *Opt. Express* **19**, 26866–26871; DOI:10.1364/OE.19.026866 (2011).
22. Klein, M. W., Enkrich, C., Wegener, M. & Linden, S. Second-harmonic generation from magnetic metamaterials. *Science* **313**, 502–504; DOI:10.1126/science.1129198 (2006).
23. Zdanowicz, M. *et al.* Ordered multilayer silica-metal nanocomposites for second-order nonlinear optics. *Appl. Phys. Lett.* **103**, 251907; DOI:10.1063/1.4852795 (2013).
24. Maker, P. D., Terhune, R. W., Nisenoff, M. & Savage, C. M. Effects of dispersion and focusing on the production of optical harmonics. *Phys. Rev. Lett.* **8**, 21–22; DOI:10.1103/PhysRevLett.8.21 (1962).
25. Jerphagnon, J. & Kurtz, S. K. Maker fringes: A detailed comparison of theory and experiment for isotropic and uniaxial crystals. *J. Appl. Phys.* **41**, 1667–1681; DOI:10.1063/1.1659090 (1970).
26. Kauranen, M., Verbiest, T., Maki, J. J. & Persoons, A. Second-harmonic generation from chiral surfaces. *J. Chem. Phys.* **101**, 8193–8199; DOI:10.1063/1.468203 (1994).
27. Sipe, J. E. New green-function formalism for surface optics. *J. Opt. Soc. Am. B* **4**, 481–489; DOI:10.1364/JOSAB.4.000481 (1987).
28. Maki, J. J., Kauranen, M. & Persoons, A. Surface second-harmonic generation from chiral materials. *Phys. Rev. B* **51**, 1425–1434; DOI:10.1103/PhysRevB.51.1425 (1995).
29. Johnson, P. B. & Christy, R. W. Optical constants of the noble metals. *Phys. Rev. B* **6**, 4370–4379; DOI:10.1103/PhysRevB.6.4370 (1972).
30. Rodriguez, F. J., Wang, F. X. & Kauranen, M. Calibration of the second-order nonlinear optical susceptibility of surface and bulk of glass. *Opt. Express* **16**, 8704–8710; DOI:10.1364/OE.16.008704 (2008).
31. Prasad, P. N. & Williams, D. J., eds. *Introduction to Nonlinear Optical Effects in Molecules and Polymers* (John Wiley & Sons, Inc., 1991).

Acknowledgments

This work was supported by the Academy of Finland (136080 and 134980). M.Z. acknowledges the Wihuri Foundation and J. H. the Graduate School of Tampere University of Technology for financial support. The authors thank Antti Rantamäki (Optoelectronics Research Centre, Tampere University of Technology) for preparing silica layers on the samples.

Author contributions

M.Z. wrote the main manuscript text and carried out the calculations, J.H. prepared the aerosol samples, E.H. prepared Fig. 1(b). M.Z., J.H., J.M., E.H., T.N., M.K., G.G., all authors reviewed the manuscript.

Additional information

Competing financial interests: The authors declare no competing financial interests.

How to cite this article: Zdanowicz, M. *et al.* Second-harmonic response of multilayer nanocomposites of silver-decorated nanoparticles and silica. *Sci. Rep.* **4**, 5745; DOI:10.1038/srep05745 (2014).

Tampereen teknillinen yliopisto
PL 527
33101 Tampere

Tampere University of Technology
P.O.B. 527
FI-33101 Tampere, Finland

ISBN 978-952-15-3351-8
ISSN 1459-2045